

The Design of a Multi-Mission Relay Satellite

a project presented to
The Faculty of the Department of Aerospace Engineering
San Jose State University

in partial fulfillment of the requirements for the degree
Master of Science in Aerospace Engineering

by

Tyler A. B. Saunders

December 2022

approved by

Dr. Periklis Papadopoulos
Faculty Advisor



© 2022
Tyler A. B. Saunders
ALL RIGHTS RESERVED

ABSTRACT

The Design of a Multi-Mission Relay Satellite

Tyler A. B. Saunders

This project demonstrates the design of a multi-mission relay satellite (MMRS) to facilitate communication between spacecraft in the outer solar system and the Deep Space Network antennas on Earth. The design of five key subsystems, including communications, power, propulsion, structures, and thermal, from a systems engineering perspective is addressed. Finite element software was leveraged to verify the natural frequencies and mode shapes of an idealized MMRS spacecraft for the selected launch vehicle. Several mission profiles were additionally investigated to determine the appropriate orbital maneuver required to send the spacecraft on an interplanetary trajectory from Earth to the outer solar system.

ACKNOWLEDGEMENTS

I would like to thank Jordan Pollard, Michael Barrett, Andrew Strauss, and Dr. Periklis Papadopoulos for their help and support throughout this project.

Table of Contents

ABSTRACT	iii
ACKNOWLEDGEMENTS	iv
LIST OF TABLES	x
LIST OF FIGURES	xiii
NOMENCLATURE	xv
1.0 Introduction	1
1.1 Motivation.....	1
1.2 Literature Review.....	1
1.2.1 Outer Solar System Exploration	1
1.2.2 Application of Communication Relays.....	2
1.2.3 Deep Space Optical Communications.....	2
1.2.4 Spacecraft Power.....	3
1.2.5 Spacecraft Communications	5
1.2.6 Spacecraft Thermal Control	5
1.2.7 Spacecraft Propulsion	6
1.3 Project Proposal	6
1.4 Methodology	6
2.0 Communication Subsystem	7
2.1 Requirements	7
2.2 Data Link Design	7
2.3 High & Low Gain Antennas	10
2.3.1 High Gain Antenna	11
2.3.2 Low Gain Antennas	15
2.3.3 UHF.....	16
2.4 Transponders & Amplifiers	17
2.4.1 Transponders.....	17
2.4.2 RF Amplifiers	18
2.5 Communication Subsystem Sizing	18
2.6 Block Diagram.....	20
2.7 Design of Experiments.....	21
2.8 Verification & Validation	22
2.9 Test Plan.....	23

2.10 Risk Assessment	23
3.0 Power Subsystem	25
3.1 Requirements	25
3.2 Power Sources.....	26
3.2.1 Solar Arrays	26
3.2.2 Batteries	30
3.2.3 Radioisotope Thermoelectric Generators.....	31
3.2.5 Power Distribution, Regulation, & Control	34
3.3 Block Diagrams	34
3.4 Design of Experiments.....	35
3.5 Verification & Validation	37
3.6 Test Plan.....	38
3.7 Risk Assessment	38
4.0 Propulsion Subsystem.....	39
4.1 Requirements	39
4.2 Governing Equations	40
4.3 Thrusters	41
4.3.1 Orbital Insertion Thrusters	42
4.3.2 Trajectory Correction Thrusters.....	42
4.3.3 Attitude Control Thrusters	43
4.3.4 Commercial Off-The-Shelf Thrusters	44
4.4 Block Diagram.....	44
4.5 Design of Experiments.....	45
4.6 Verification & Validation	46
4.7 Test Plan.....	47
4.8 Risk Assessment	48
5.0 Thermal Subsystem	49
5.1 Subsystem Overview	49
5.1.1 Spacecraft Thermal Environment	50
5.2 Thermal Control Components.....	50
5.2.1 Surface Finishes	50
5.2.2 Insulation.....	51
5.2.3 Radiators	52

5.2.4 Heaters, Louvers, & Heat Pipes	52
5.3 Requirements	53
5.4 Governing Equations	55
5.5 Block Diagram	57
5.6 Design of Experiments.....	57
5.7 Verification & Validation	59
5.8 Test Plan.....	60
5.9 Risk Assessment	60
6.0 Structures and Mechanisms Subsystem.....	62
6.1 Subsystem Overview	62
6.1.1 General Structural Requirements	62
6.1.2 Design Options & Criteria	63
6.1.3 Sizing & Analysis of Structural Members	64
6.2 Requirements	64
6.3 Structural Design & Analysis	65
6.4 Governing Equations	68
6.5 Design of Experiments.....	70
6.6 Spacecraft Mass, Dimensions, & Packaging.....	72
6.6.1 Spacecraft Mass & Sizing	72
6.6.2 Approximate Spacecraft Dimensions.....	73
6.6.3 Mechanisms, Deployables, & Packaging.....	74
6.7 Structural Analysis.....	75
6.7.1 Geometry, Mesh Generation, Boundary Conditions, & Load Factors.....	75
6.7.2 Static Structural Analysis.....	76
6.7.3 Modal Analysis	78
6.8 Block Diagram.....	80
6.9 Verification & Validation	81
6.10 Test Plan.....	82
6.11 Risk Assessment	82
7.0 Orbital Mechanics and Mission Design	83
7.1 Hohmann Transfer	83
7.1.1 Constants & Assumptions.....	84
7.1.2 Delta-V Calculations.....	85

7.1.3 Wait Time	85
7.1.4 Equations of Motion.....	86
7.1.5 Orbit Simulation.....	87
7.2 Launch Vehicle	88
8.0 Overall System Diagrams & Specifications	89
8.1 System Diagrams	89
8.2 System Specifications	91
9.0 Path Forward	97
References.....	99
APPENDIX A – Calculations for Subsystem Sizing	106
A.1 – Communication Downlink Parameters (HGA, X-Band, Mars-Orbiting)	106
A.2 – Communication Uplink Parameters (HGA, X-Band, Mars-Orbiting)	107
A.3 – Communication Downlink Parameters (HGA, Ka-Band, Mars-Orbiting).....	108
A.4 – Solar Array Sizing (Mars).....	109
A.5 – Solar Array Sizing (Jupiter)	110
A.6 – Theoretical MMRS Battery Sizing.....	111
A.7 – Propulsion System Sizing	112
A.8 – Propulsion System Storage & Feed.....	113
A.9 – Thermal Control System Sizing	114
A.10 – Thermal Control: Solar Array Analysis	115
A.11 – Spacecraft Bus: Preliminary Sizing	116
A.12 – Structure & Mechanisms: Monocoque Structure	117
A.13 – Structure & Mechanisms: Semi-Monocoque Structure	118
A.14 – Launch Vehicle Information: Atlas V 400.....	119
APPENDIX B – Orbital Mechanics & Mission Design	120
B.1 – Derivation of Position & Velocity Vectors	120
B.2 – Code: Position & Velocity Vectors from Keplerian Elements (Mars About Sun).....	121
B.3 – Code: Position & Velocity Vectors from Keplerian Elements (Earth About Sun)	122
B.4 – Code: Position & Velocity Vectors from Keplerian Elements (Transfer About Sun)	124
B.5 – Code: Hohmann Transfer Wait Time	125
B.6 – Code: Hohmann Transfer Delta-V	126
B.7 – Code: Keplerian Elements from Position & Velocity Vectors.....	127
B.8 – Code: Animation of Earth, Mars, & Hohmann Orbits	129

APPENDIX C – Risk Assessment	134
C.1 – Rubrics for Ascertaining Risk Level.....	134

LIST OF TABLES

Table 2.1 – Parameters of NASA’s Deep Space Network TT&C [13].....	8
Table 2.2 – High gain antenna system X-band telemetry downlink parameters of existing space probes and MMRS (part 1).....	12
Table 2.3 – High gain antenna system X-band telemetry downlink parameters of existing space probes and MMRS (part 2).....	12
Table 2.4 – High gain antenna system X-band command uplink parameters of existing space probes and MMRS.	14
Table 2.5 – Ka-band telemetry downlink parameters of existing space probes and MMRS.	15
Table 2.6 – Low gain antenna system X-band telemetry downlink parameters of existing space probes and MMRS.	16
Table 2.7 – TWTA parameters. [15].....	18
Table 2.8 – Total communication system mass and power of existing spacecraft and MMRS.....	19
Table 2.9 – MMRS communication subsystem mass breakdown.	20
Table 2.10 – MMRS communication subsystem power breakdown.	20
Table 2.11 – Design of subsystems for communication subsystem.....	21
Table 2.12 – Communication subsystem verification and validation (part 1).	22
Table 2.13 – Communication subsystem verification and validation (part 2).	23
Table 2.14 – Communication subsystem risk assessment.	24
Table 3.1 – Solar power parameters for MMRS at Mars and Jupiter, from equation 3.1.	28
Table 3.2 – Power system parameters of existing solar-powered spacecraft and MMRS.	29
Table 3.3 – Battery data for existing spacecraft and MMRS.	30
Table 3.4 – Battery parameters for theoretical MMRS battery candidate.	31
Table 3.5 – RTG data for existing spacecraft and MMRS.....	32

Table 3.6 – Power subsystem sizing breakdown.	33
Table 3.7 – Design of experiments for power subsystem for theoretical Mars solar array.....	36
Table 3.8 – Power subsystem verification and validation (part 1).....	37
Table 3.9 – Power subsystem verification and validation (part 2).....	37
Table 3.10 – Power subsystem risk assessment.	38
Table 4.1 – Orbital insertion thruster data for existing spacecraft and MMRS.	42
Table 4.2 – Trajectory correction thruster data for existing spacecraft and MMRS.....	43
Table 4.3 – Attitude control thruster data for existing spacecraft and MMRS.	43
Table 4.4 – Commercial thruster candidate key specifications.....	44
Table 4.5 – Design of experiments for the propulsion subsystem.	45
Table 4.6 – Propulsion subsystem verification and validation (part 1).....	47
Table 4.7 – Propulsion subsystem verification and validation (part 2).....	47
Table 4.8 – Propulsion subsystem risk assessment.....	48
Table 5.1 – Typical operational and survival temperature limit ranges. [60]	49
Table 5.2 – Average planetary infrared and albedo emissions and solar constant. [60]	50
Table 5.3 – Surface finishes and properties. [60].....	51
Table 5.4 – Louver parameters.	53
Table 5.5 – Design of experiments for the thermal subsystem.	58
Table 5.6 – Thermal subsystem verification and validation (part 1).	59
Table 5.7 – Thermal subsystem verification and validation (part 2).	60
Table 5.8 – Propulsion subsystem risk assessment.....	61
Table 6.1 – Typical unmanned spacecraft test options. [64].....	63
Table 6.2 – Launch vehicles and payload to orbit masses for existing spacecraft and MMRS.....	66
Table 6.3 – Atlas V launch vehicle parameters (from appendix A.14). [66]	66

Table 6.4 – Select parameters for MMRS main structure of monocoque construction (from appendix A.12).	67
Table 6.5 – Select parameters for MMRS main structure of semi-monocoque construction (from appendix A.13).	67
Table 6.6 – Cylinder applied loads.	70
Table 6.7 – Design of experiments for the structure subsystem.	71
Table 6.8 – Mass broken down by subsystem.	72
Table 6.9 – Launch and dry mass for existing spacecraft and MMRS.	72
Table 6.10 – Dimensions of existing spacecraft and MMRS.	74
Table 6.11 – Structural parameters per element count.	77
Table 6.12 – Natural frequency (Hz) of each mode per element count.	78
Table 6.13 – Structure subsystem verification and validation (part 1).	81
Table 6.14 – Structure subsystem verification and validation (part 2).	82
Table 6.15 – Propulsion subsystem risk assessment.	82
Table 7.1 – Mass and radius constants.	85
Table 7.2 – Wait time and associated values for several values of true anomaly.	86
Table 7.3 – Keplerian elements of each orbit.	87
Table 8.1 – Communication subsystem sizing.	92
Table 8.2 – Power subsystem sizing.	93
Table 8.3 – Propulsion subsystem sizing.	94
Table 8.4 – Thermal subsystem sizing and planetary constants.	94
Table 8.5 – Structure & mechanisms subsystem sizing.	95
Table 8.6 – Orbital mechanics and mission sizing.	96

LIST OF FIGURES

Figure 2.1 – Peak gain vs. HGA diameter for HGA X-band downlink of in-family space probes and MMRS (red).....	13
Figure 2.2 – Transmit power vs. HGA diameter for HGA X-band downlink of in-family space probes and MMRS (red).....	13
Figure 2.3 – Electra UHF transceiver assembly. [15].....	17
Figure 2.4 – Total available power vs. total available mass for existing spacecraft and MMRS (red).	19
Figure 2.5 – General high-level block diagram for MMRS communication system HGA sizing.....	20
Figure 3.1 - Power generated by solar array vs. solar array area for Mars orbiters and MMRS (red).....	29
Figure 3.2 – Diagram of the GPHS-RTG used on Cassini. [41].....	33
Figure 3.3 – High-level block diagram of the power system (theoretical solar array).....	35
Figure 3.4 – High-level block diagram of the power system (RTG).	35
Figure 4.1 – High-level block diagram of propulsion subsystem.	45
Figure 5.1 – High-level block diagram of thermal subsystem.	57
Figure 6.1 – Aluminum 7075 monocoque cylindrical shell model.....	65
Figure 6.2 – Fuel mass vs. total spacecraft launch mass for existing spacecraft and MMRS (red).....	73
Figure 6.3 – Total spacecraft launch mass vs. structure volume for existing spacecraft and MMRS (red).	74
Figure 6.4 – Mesh of cylindrical beam.	76
Figure 6.5 – Contour of maximum equivalent stress.	77
Figure 6.6 – Stress convergence analysis.....	78
Figure 6.7 – The first seven mode shapes (left to right, top to bottom, modes 1 through 7).	79
Figure 6.8 – Natural frequency convergence analysis.	79
Figure 6.9 – High-level block diagram of the structure subsystem illustrating deformation.....	80

Figure 6.10 – High-level block diagram of the structure subsystem illustrating limit loads.	80
Figure 7.1 – General illustration of Earth-Mars Hohmann transfer.	83
Figure 7.3 – Animation of spacecraft Q on a Hohmann transfer from Earth to Mars.	88
Figure 8.1 – Overall high-level MMRS block diagram.	89
Figure 8.2 – MMRS random N^2 diagram.	90
Figure 8.3 – MMRS ordered N^2 diagram.	91

NOMENCLATURE

Symbol	Definition	Unit
Greek		
α	Solar absorptivity	
γ	Specific heat ratio	
ΔL	Change in length	m
ΔV	Change in velocity	m/sec
δ	Axial and lateral deflection	m
ε	IR emissivity	
ε^*	Effective emittance	
η	Antenna efficiency	
η	Interaction effect	
θ	True anomaly	deg
θ	Sun incidence angle	deg
λ	Wavelength	m
λ_{\max}	Maximum Earth central angle	deg
λ_{\min}	Earth central angle from ground station	deg
ρ	Density	kg/m ³
ρ	Average planetary albedo	
σ	Stefan-Boltzmann constant	W/m ² K ⁴
Ω	Right ascension of the ascending node	deg
ω	Argument of periapsis	deg
Alphabetical		
a	Semi-major axis length	km
A	Cross-sectional area of representative beam	m ²
A_{sa}	Solar array area	m ²
A^*	Nozzle throat area	m ²
C	Received power	W
D	Data quality	Bits
D	Distance from sun	m
D_r	Receive antenna diameter	m
e	Eccentricity	
E	Young's modulus	N/m ²
E_b	Received energy per bit	W/bit
F	Reduction in viewing angle	
F	Thrust applied by engine	N
F	Axial load	N
F_{albedo}	Thermal geometry factor	
F_{EIR}	Thermal geometry factor	
f_{nat}	Axial and lateral natural frequency	Hz
F_{tu}	Ultimate tensile strength	N/m ²
g_0	Acceleration of gravity	m/s ²

Symbol	Definition	Unit
G_r	Receive antenna gain	dB
G_t	Transmit antenna gain	dB
H_{sun}	Power intensity at surface of sun	W/m^2
H_0	Solar radiation intensity	W/m^2
i	Inclination angle	deg
I	Area moment of inertia of beam cross-section	m^4
I_{EIR}	Intensity of Earth IR	W
I_{solar}	Intensity of solar fluxes	W
I_{sp}	Specific impulse	sec
k	Boltzmann constant	J/K
K	Spring constant	N/m
L	Representative beam length	m
L_a	Transmission path loss	dB
L_l	Transmitter-to-antenna line loss	dB
L_s	Space loss	dB
M	Margin to account for missed passes	
M	Main effect	
M	Bending moment limit load	Nm
m_{dot}	Propellant mass flow rate	kg/sec
m_B	Mass of representative beam	kg
m_o	Initial total spacecraft mass, including propellant	kg
m_p	Initial propellant mass	kg
m_f	Final total spacecraft mass, excluding propellant	kg
n	Load factor	
N_o	Noise spectral density	W/Hz
P	Transmitter power	W or dBm
P_{axial}	Axial limit load	N
P_{BOL}	Solar array performance at beginning of life	W
P_c	Gas pressure in chamber	Pa
P_d	Satellite power during daylight	W
P_e	Satellite power during eclipse	W
P_e	Gas pressure at nozzle exit	Pa
P_{eq}	Equivalent axial load	N
P_{EOL}	Solar array performance at end of life	W
P_{inf}	Ambient pressure	Pa
P_{sa}	Solar array power generated during daylight	W
P_0	Efficiency factor	P_0
Q	Heat leaving radiator surface	W
$Q_{external}$	Environmental heat absorbed	W
$Q_{internal}$	Internal power dissipation	W
Q_{MLI}	Heat lost from elsewhere on spacecraft	W
$Q_{radiator}$	Heat rejected from the radiator surfaces	W
q_{albedo}	Absorbed albedo heat load per unit area	W/m^2
$q_{backload}$	Radiative heat load from external spacecraft surfaces	W/m^2

Symbol	Definition	Unit
q_{EarthIR}	Absorbed Earth IR heat load per unit area	
q_{external}	Environmental heat load on radiator per unit area	W/m^2
q_{solar}	Absorbed solar heat load per unit area	W/m^2
R	Data rate	Bits/sec
R	Gas constant	J/mol/K
R	Cylinder radius	m
R	Mass ratio of m_o/m_f	
R_{sun}	Radius of sun	m
S	Sphere radius	m
t	Cylinder thickness	m
T_c	Chamber temperature	K
T_d	Orbit period (daylight)	sec
T_e	Orbit period (ellipse)	sec
T_{initiate}	Time required to initiate a communication pass	sec
T_{max}	Maximum time satellite is in view of ground station	sec
T_s	System noise temperature	K
v_e	Propellant exhaust velocity	m/s
x_d	Efficiency of power transmission from solar arrays to batteries	
x_e	Efficiency of power transmission from solar arrays to batteries	
Acronyms		
AC	Alternating Current	
ACS	Attitude Control System	
BOL	Beginning of Life	
CAD	Computer-Aided Design	
C&DH	Command and Data Handling	
DC	Direct Current	
DSN	Deep Space Network	
DSOC	Deep Space Optical Communications Package	
EDL	Entry, Descent, and Landing	
EIRP	Effective Isotropic Radiated Power	
EOL	End of Life	
FEA	Finite Element Analysis	
FOS	Factor of Safety	
GTO	Geostationary Transfer Orbit	
HGA	High Gain Antenna	
IMU	Inertial Measurement Unit	
IR	Infrared	
LEO	Low Earth Orbit	
LGA	Low Gain Antenna	
MarCO	Mars CubeSat One	
MGA	Medium Gain Antenna	

Symbol	Definition	Unit
MLI	Multilayer Insulation	
MMH	Monomethylhydrazine	
MMRS	Multi-Mission Relay Satellite	
MMRTG	Multi-Mission Radioisotope Thermoelectric Generator	
OSR	Optical Solar Reflector	
RCS	Reaction Control System	
RF	Radio Frequency	
RHU	Radioscope Heater Units	
RTG	Radioisotope Thermoelectric Generators	
TCS	Thermal Control System	
S/C	Spacecraft	
SDPT	Small Deep Space Transponder	
SNR	Signal-to-Noise Ratio	
SNT	System Noise Temperature	
TCT	Trajectory Correction Thruster	
TT&C	Telemetry Tracking and Command	
TWTA	Traveling Wave Tube Amplifier	
UHF	Ultra High Frequency	
ULA	United Launch Alliance	
UTS	Ultimate Tensile Strength	

1.0 Introduction

1.1 Motivation

With plans for the establishment of a human presence on Mars by governments and private entities in the near term, as well as plans for the robotic exploration of Titan and other outer solar system bodies, there will be an increased demand for effective and near real-time communication between Earth and spacecraft orbiting these distant bodies. [1] Currently, deep space probes are equipped with large antennas and high-power transmitters that provide high data-rate communication between the spacecraft and the Deep Space Network antennas on Earth. However, these telecommunication instruments require a significant percentage of the spacecraft's overall power and mass. By designing purpose-built communication relay satellites to be positioned in deep space locations, future deep space missions could instead leverage the high data rates afforded by these relay satellites while benefiting from a reduction of mass and size caused by off-loading the large telecommunications systems to such relays.

1.2 Literature Review

1.2.1 Outer Solar System Exploration

Identifying existing communication satellites and deep space probes were of particular interest when considering the design of a new deep space relay satellite. The Galileo and Cassini spacecraft (launched in the late 1990s) are two prominent examples of outer solar system probes. Both spacecraft carried an array of instrumentation, including robust telecommunication systems. These telecommunication systems contained the traditional suite of instruments for command and control and for the transmission of mission data to Earth, including large high-gain antennas and high-power transmitters to provide high data-rate communication. It is assumed that future spacecraft would require a similar suite of telecommunication instruments. Telecommunication instruments require a significant allocation of a spacecraft's overall power and weight. If future outer solar system probes are scaled down in size from Galileo and Cassini, the telecommunication systems of these spacecraft would still require the same large antennas and high-power transmitters. This would thus account for a significant percentage of the overall weight, volume, and power of the spacecraft. [2]

Rather than carry a full suite of telecommunication hardware on board each future spacecraft launched into the outer solar system as the means of contact with the Deep Space Network antennas on Earth, the following approach could be taken. These future deep space spacecrafts could instead carry only a local telecommunication system and instead communicate with a relay satellite. This relay satellite would be tasked with sending the data to Earth. Relay satellites of this sort could support multiple missions to the outer solar system, with such missions benefiting from a decreased communication system mass and power allocation, and thus an increased mass and power allocation for scientific instruments. [2]

1.2.2 Application of Communication Relays

Communication between a spacecraft in deep space and the ground control team on Earth during a risky maneuver, such as entry, descent, and landing (EDL), is critical. Although the speed of light prevents instantaneous communication between the spacecraft and Earth, near real-time communication can be critical for taking corrective action following a critical event. Spacecraft generally rely on links to nearby planetary orbiters to relay data from the spacecraft to the Deep Space Network, rather than relaying data from the probe directly. This is because the rate of data transmission from the probe directly may be prohibitively long. However, a planetary relay orbiter may not always be in range of the probe.

The Mars CubeSat One mission (commonly abbreviated as MarCO) was a Mars flyby mission launched alongside the NASA InSight Mars lander in 2018. The mission consisted of two identical 6U cubesats designed to serve as near real-time communication relays for the InSight lander during the EDL phase of the InSight mission. The use of the MarCO relay cubesats reduced the data transmission time dramatically. Rather than taking several hours to relay the data back to Earth from InSight itself, the MarCO relay shortened this time to only 8 minutes, which is the Earth-Mars transmission time at the speed of light.

The MarCO CubeSats were the first spacecraft built in the CubeSat form factor for use in a deep space mission. They served as a test to validate new miniaturized communications and navigation technologies that had been designed by NASA's Jet Propulsion Laboratory specifically for the CubeSat form factor. They also served to validate the "carry your own" relay approach for use in future missions as a means to reduce mission risk during the critical EDL phase. The MarCO CubeSats were successful in completing their mission objectives, though lost contact after five weeks.

MarCO was required to receive UHF signals and simultaneously transmit the data via an X-band link to the Deep Space Network. In terms of data relay equipment, the MarCO CubeSats utilized one ultra-high frequency (UHF) antenna. This was a specially-designed wire loop deployable antenna. MarCO additionally utilized a flat array X-band antenna and a transponder capable of receiving UHF and receiving/transmitting X-band. This transponder, known as Iris, is a purpose-built low power deep-space transponder designed specifically for use in CubeSats. To relay data, a high gain reflectarray antenna was chosen due to its small, flat size. (Microstrip patch antennas and mesh reflector antennas were also considered). EDL data from the InSight lander was transmitted at 8 kbit/s to the cubesats and was then simultaneously retransmitted at an X-band frequency at 8 kbit/s to Earth. [3]

1.2.3 Deep Space Optical Communications

In 2023, NASA will launch the Psyche probe to an asteroid (also named Psyche) in the asteroid belt. The Psyche mission, in addition to carrying its scientific payload, will be carrying the Deep Space Optical Communications package (DSOC) developed by NASA. DSOC is an

experiment in high-efficiency laser communication. It is intended to show an improvement in communication performance of 10 to 100 times that of current radio frequency technology, without substantially increasing the mass, volume, or power requirements compared to a spacecraft using conventional radio frequency technology. [4] Higher data rate delivery between Earth and a spacecraft can be achieved by utilizing higher radio frequencies, notably the X-band and the Ka-band. However, stronger signal power density can be achieved using the higher optical frequencies. The technology employed by the Deep Space Optical Communications package will use near-infrared lasers operating at a wavelength of 1.55 μm . [5]

The motivation behind the DSOC package is that future missions throughout the solar system would benefit from high-definition imagery and video feeds, as well as near real-time data transmission. As a reference, the radio frequency technology on the Mars Reconnaissance Orbiter requires 7.5 hours to transmit the entirety of the data on its onboard recorder, at a maximum data rate of 5.2 Mbps. With improvements in data rates of over 10 times that of conventional deep space RF (Ka-band) systems, the volume of science data returned by NASA missions across the solar system is of particular interest to NASA. [5]

Challenges facing the use of optical deep space communications in the near-term include the lack of maturity of robust and efficient space laser transmitters. Also of consideration is the lack of data pertaining to the operational lifetime of lasers in space, in addition to the cost-effectiveness of large-diameter (8 to 12 meter) aperture ground receivers. Additionally, while it is possible to construct an optical transceiver with 10 times the RF capability with current technology, it would be prohibitively expensive when compared to constructing an analogous conventional RF system. [5]

1.2.4 Spacecraft Power

The power subsystem of a spacecraft generally must store energy in rechargeable batteries. Nickel-hydrogen batteries were among the most-commonly utilized pre-1990 due to the high energy density they provided compared to other batteries of the era, including nickel-cadmium. [6] However, since the 1990's, significant advances in lithium-ion batteries have been made, generally rendering nickel-hydrogen batteries obsolete. Thus, future spacecraft, including NASA's planned Dragonfly probe to Titan [1], will leverage lithium-ion batteries for their significantly higher energy density, lower discharge rates, and higher coulombic efficiency, when compared to nickel-hydrogen batteries. [7]

Batteries must be capable of surviving the harsh environment of space, while also enduring the shock, vibration, and acceleration loads experienced during launch. Radiation resistance and the ability to operate in temperatures as low as -80°C are required. For spacecraft applications, batteries are required to deliver maximum electrical energy while minimizing mass and volume. Spacecraft batteries must generally experience more than 30,000 cycles (orbiting spacecraft) and have a long active shelf life of between seven and ten years (planetary probes). [6] Modern

interplanetary spacecraft require between 300 W and 2.5 kW of electrical power for operation. [8]

Spacecraft designed for use in the inner solar system are generally equipped with solar panels, which recharge the batteries of the spacecraft. Conventional photovoltaic solar panels for space applications achieve an energy conversion efficiency of approximately 29%. The solar cells themselves are composed of crystalline silicon and gallium arsenide.

For spacecraft operating in the outer solar system, radioisotope thermoelectric generators (RTGs) are commonly used. Radioisotope thermoelectric generators are analogous in function to a nuclear battery, but not utilizing nuclear fusion or nuclear fission, and utilizing no moving parts. RTGs contain several kilograms of an isotopic mixture of radioactive plutonium-238 in the form of individual pellets. These pellets function as a source of heat, as the natural radioactive decay of the plutonium-238 produces heat. This heat is then converted into electricity by means of an array of thermocouples composed of silicon-germanium. A thermocouple is a thermoelectric device that can convert thermal energy directly into electrical energy using the Seebeck effect. Excess waste heat is expelled into space via radiation using metal fins. Their placement relative to infrared detecting science instruments must be considered due to the waste heat they emit.

Due to the radioactive nature of the plutonium-238 pellets, spacecraft utilizing RTGs for power are subject to a rigorous safety analysis and review by the Department of Energy before they can be launched into space. These reviews ensure that the RTGs are designed to survive launch accidents without releasing the hazardous materials they contain. The results of these reviews are evaluated by an independent panel of experts and are ultimately used by the White House to evaluate the overall risk presented by the mission, requiring presidential approval for launch.

In addition to the environmental concerns they pose, radioisotope thermoelectric generators are limited in usage by their expense. RTGs degrade in flight by 1-2% per year; this is slightly faster than the 1% degradation per year of photovoltaics. Despite this, RTGs have seen use onboard a number of NASA space probes, including Voyager 1, Voyager 2, Pioneer 10, Pioneer 11, Galileo, Ulysses, Cassini, New Horizons, and the Mars Science Laboratory. [8]

Future RTGs onboard spacecraft could see design improvements that would increase power output and operational life. As of 2016, NASA has been reviewing the design of a multi-mission radioisotope thermoelectric generator (MMRTG), which utilizes thermocouples composed of the cobalt arsenide (CoAs₃) material skutterudite. These thermocouples can operate at a smaller temperature difference than the current tellurium-based thermocouple design. The ramifications of this are that an otherwise similar RTG could generate 25% more power at mission start, and at least 50% more power after seventeen years in operation. NASA hopes to incorporate these new RTGs on their upcoming New Horizons missions. [9] One future application of these new RTGs is providing power for NASA's Dragonfly mission to Titan. Dragonfly will be powered by a lithium-ion battery, which will be recharged by a Multi-Mission Radioisotope Thermoelectric Generator. [1] As Titan is 9.5 AUs from the sun, and thus only 1.1% of the terrestrial solar constant is available, RTGs are desirable. [6]

1.2.5 Spacecraft Communications

A general communication system consists of antennas, amplifiers, and transponders, among other components. To size the communication system of a spacecraft, the data rate of the uplink and downlink must be determined, the communication frequency bands must be selected, the RF power budget for the RF links must be selected, and the and physical equipment must be selected. There are three primary types of data that a satellite receives and transmits. These include command and data handling, health and status telemetry, and mission and science data

The data handling subsystem encompasses the management of all forms of data on the spacecraft. This includes carrying out commands sent from Earth, preparing data for transmission, managing and processing data about the status of all subsystems and the payload, timekeeping, carrying out maneuvers, and monitoring and responding to problems that occur onboard. The selection of the frequency bands is constrained by regulatory bodies. The designer of the system must receive approval from the appropriate agency to operate at a specific frequency band and at a specific orbit. Bands include UHF, L, S, C, X, Ku, Ka, and V. [10]

1.2.6 Spacecraft Thermal Control

Spacecraft operating in the outer solar system, despite being far from the sun, may still approach near to the sun for the purpose of performing gravity-assist trajectories. As a result, such spacecraft may be subjected to severe temperature extremes, and thus require the appropriate thermal protection. Such thermal protection systems may be classified as either passive or active thermal control. [8]

Passive thermal control refers to the use of passive systems, which are generally used to reflect heat away from the spacecraft. This includes multi-layer insulation blankets, which are used to reflect infrared radiation. These are constructed from layers of a reflective silver-aluminum coating layered behind sheets of an amber-colored Kapton material. Such blankets also serve to retain internal spacecraft heat to prevent component temperatures from dropping below their operating tolerance. Kapton (as well as other energy-absorbing fabrics) additionally serve as micrometeoroid protection, which is of particular use for probes orbiting the Jovian planets. Optical solar reflectors (OSRs) are a type of thermal control mirrors, generally composed of quartz mirror tiles. These reflect sunlight and infrared radiation, and were used on the NASA Magellan probe to Venus. [8] Additionally, thermal paint provides efficient passive cooling, with internal components radiating more-efficiently if painted black. [11]

Active thermal control includes autonomous thermostatically-controlled resistive electric heaters to prevent component temperatures from dropping below their operating tolerance. Radioscope heater units (RHUs) may be placed throughout the interior of the spacecraft, in addition to temperature sensors. Louvers are mechanical devices (similar to household blinds). By angling their blades, louvers can vary the emission of heat from their surfaces and minimize the electrical power used for heaters to maintain a temperature range. They are positioned by bi-metallic strips that cause the louvers to open when internal temperature is high. Note, however, that

refrigeration is considered impractical as a means of cooling for satellite applications. [8]

1.2.7 Spacecraft Propulsion

Propulsion systems found on spacecraft include, but are not limited to, ion, nuclear thermal, and chemical bi or mono propellant. Chemical propulsion systems are among the most commonly used and consist of propellant tanks, plumbing systems with valves (that are either electrically or pyrotechnically operated), helium tanks for pressurization, and additional components that vary depending on the type of chemical propulsion system equipped. Ion engines operate by ionizing a gas (like xenon), which strips electrons from the atoms. This makes it responsive to electric and magnetic fields. Nuclear thermal engines offer high thrust and specific impulse compared to chemical engines, but have never seen use beyond test articles. [12]

1.3 Project Proposal

The objective of this project is to demonstrate the design of a deep space communication satellite that can act as a relay between deep space probes in the outer solar system and the Deep Space Network antennas on Earth.

1.4 Methodology

An in-depth analysis of five key subsystems, including communication, power, propulsion, thermal, and structures, will be performed. Recent advances in power and propulsion technology will be leveraged, including, but not limited to, advanced radioisotope thermal generators as a means of extending the operational life of satellites operating in deep space. Advances in communication technology will be leveraged, including, but not limited to, the use of Ka-band transmitters for increased data transmission rates from distant planetary bodies.

The general approach used for completing this project is as follows:

- Identify mission parameters for a Mars-orbiting spacecraft, with application to spacecraft operating in other outer-solar system locations.
- Derive subsystem requirements based on mission parameters.
- Using analytical design equations, regression analysis based on historical data for in-family spacecraft, and computational analysis tools, develop sizing parameters for each subsystem.

2.0 Communication Subsystem

2.1 Requirements

The general steps in designing the communication subsystem are as follows. First, the mission objectives and requirements must be defined in detail such that alternative architectures can be evaluated and compared. Second, the data rates for each of the links identified in step 1 must be identified. Third, each link in the network must be designed and sized. Fourth, the size and mass of the spacecraft antennas, the power and mass of the spacecraft transmitters, and the power and mass of all other subsystem components must be estimated. Ultimately, antenna size and transmitter power are the major drivers in sizing communication system. [13] The operational and functional requirements of the communication system for the MMRS spacecraft are outlined below and are further elaborated upon in section 2.8.

- Operational Requirements
 - Communications package shall be capable of relaying all data from a deep space probe to the Deep Space Network (DSN) antennas on Earth
 - Shall provide uplink (command), downlink (telemetry), and navigation with the DSN
 - Shall communicate with Deep Space Network antennas using X bands and Ka bands
 - Should send and receive data at high rates compared to existing spacecraft
- Functional Requirements
 - Shall have interoperability with NASA's Deep Space Network at X-band frequencies (7.2 GHz uplink, 8.4 GHz downlink) and Ka-band frequencies (32 GHz uplink) for telemetry, tracking, and command [15]
 - Should transmit at a rate of 200 kbps at Jupiter orbit [22]
 - Should transmit at a rate of 6 Mbps at Mars orbit [15]
 - Shall provide UHF forward-link and return-link relay services to landed planetary surface vehicles

2.2 Data Link Design

System functions (data links) include telemetry tracking and command (TT&C), data collection, and data relay. The purpose of the TT&C subsystem is to ensure the continued operation of the spacecraft. As such, the TT&C subsystem monitors the health and status of the subsystems of the spacecraft through the collection of data from onboard sensors, determines the exact location of the spacecraft through the reception, processing, and transmitting of ranging signals, and ensures the spacecraft is properly controlled through the reception, processing, and implementation of commands from the ground. Hundreds of onboard functions, including voltages, temperatures, and accelerations, may be monitored at a time. Using a multiplexer, each telemetry sensor may be sampled into sequence to combine all telemetry data into a single bit stream. The number and accuracy of functions being monitored in the spacecraft determines the

telemetry data rate. [13] Table 2.1 summarizes the key parameters of the TT&C ground station network of the DSN.

Table 2.1 – Parameters of NASA’s Deep Space Network TT&C [13].

Network	Command (uplink)		Telemetry (downlink)	
	Freq. (GHz)	Data rate (bps)	Freq. (GHz)	Data rate (bps)
NASA DSN	2.025-2.120 7.145-7.190	1.0-2000	2.2-2.3 8.4-8.5	8M-6.6M

The spacecraft must possess both an uplink and downlink capability. Uplink refers to communication from the ground to the satellite. Downlink refers to communication from the satellite to the ground. Crosslinks refer to inter-spacecraft communication. To design each link, the following parameters must be addressed. Note, however, that this is not an exhaustive list; additional parameters are provided in appendix A.1, A.2, and A.3. These parameters include frequency, data rate, antenna size, beamwidth, atmospheric attenuation, received noise, interface power, antenna gain, transmitter power, and modulation & coding. Duty factor, link availability, link access time, and orbit are additional considerations. [13].

The RF carrier frequency affects the transmitter power, antenna size, and beamwidth of the satellite. Data rate is the quantity of information transferred between the spacecraft and ground station per unit time. As data rate increases, so does the transmitter power and the antenna size. The ability to process spacecraft-generated data on-board the satellite reduces the data rate. [13] The relationship between data quantity (D) and data rate (R) is described in equations 2.1 and 2.2 below. Other key equations required for the design of the communication system are additionally provided. [13]

$$D = \frac{R(F * T_{max} - T_{initiate})}{M} \quad (2.1)$$

Where,

- D denotes data quantity (bits)
- R denotes data rate (bps)
- F denotes the fractional reduction in viewing time caused by passing at an Earth central angle λ_{min} away from the ground station
- T_{max} denotes the maximum time in which the satellite is in view of the ground station
- $T_{initiate}$ denotes the time required to initiate a communications pass
- M denotes the margin needed to account for missed passes

$$F = \left(\frac{1}{\lambda_{\max}} \right) \text{acos} (\text{cos}\lambda_{\max}/\text{cos}\lambda_{\min}) \quad (2.2)$$

Where,

- λ_{\max} denotes the maximum Earth central angle.
- λ_{\min} denotes an Earth central angle from the ground station

A link budget is theoretical calculation of the end-to-end performance of the communications link, which accounts for all of the gains and losses of the link. The result of this analysis is a set of figures of merit that describe the quality of the link. These figures of merit include signal-to-noise ratio (SNR), spectral efficiency (in bits per second), and throughput (in bits per second). [14] The link budget equation defines the relationship between data rate, antenna size, propagation path length, and transmitter power, and relates all the necessary parameters to calculate the signal-to-noise ratio of the communication system. This general equation used for sizing a digital data link is provided below.

$$\frac{E_b}{N_o} = \frac{PL_lG_tL_sL_aG_r}{kT_sR} \quad (2.3)$$

Where,

- E_b/N_o denotes the ratio of received energy-per-bit (W*s) to noise spectral density (W*Hz)
- P denotes transmitter power (W)
- L_l denotes transmitter-to-antenna line loss (dB)
- G_t denotes transmit antenna gain (dB)
- L_s denotes space loss. This is determined by the propagation path length between transmitter and receiver (dB)
- L_a denotes transmission path loss (dB)
- G_r denotes receive antenna gain (dB)
- K is the Boltzmann constant (J/K)
- T_s denotes system noise temperature (K)
- R denotes data rate (bps)

$$C = \frac{PL_lG_tL_aD_r^2\eta}{16S^2} \quad (2.4)$$

Where,

- C denotes the received power (W)
- D_r denotes the diameter of the receive antenna (m)
- η denotes antenna efficiency (commonly 0.55, though may be 0.7 in high-quality ground antennas)
- S denotes radius of sphere, at the center of which the transmitter is located (m)

$$E_b = \frac{C}{R} \quad (2.5)$$

Where,

- E_b denotes received energy per bit (J)

$$G_r = \frac{\pi^2 D_r^2 \eta}{\lambda^2} \quad (2.6)$$

Where,

- λ denotes wavelength (m)

These equations, in addition to others that solve for the unknown variables, were entered into an excel calculator to calculate the uplink and downlink values (for the X-band, Ka-band, and UHF band) for the communications system. This is provided in appendix A.1 and A.2. Notable parameters from these calculations are provided in table 2.2 below. Note that rain attenuation is assumed to be 0 dB for frequencies below 10 GHz.

The maximum downlink data rate achieved by the spacecraft is dependent upon the size of the ground station antenna. For the MMRS, the 70 m DSN antenna will be considered. However, deep space probes generally make use of both the 70 m and 34 m DSN antennas for a predetermined number of hours multiple times per week. Note that data rate decreases with distance from Earth due to the inverse square law. Assuming constant spacecraft power, the signal strength received by the DSN antennas on Earth decreases as the square of the distance. Data rate can be calculated using the relationship provided in equation 2.7 below.

$$R = \alpha P \frac{D^2 \eta_t}{16S^2} \quad (2.7)$$

Where,

- R denotes data rate (bps)
- P denotes transmitter power (dBm)
- D denotes antenna diameter (m)
- η_t denotes efficiency of the transmit antenna
- S denotes distance between ground station and antenna (m)

2.3 High & Low Gain Antennas

Spacecraft, such as the Mars Reconnaissance Orbiter, operate in different frequency bands. The five primary mission phases of the MMRS are launch, cruise, approach, orbit insertion, aerobraking, and relay. During the cruise phase of the mission, telecom in both directions (uplink and downlink) with the DSN occurs via the X-band (~8 GHz) for command, telemetry, and radiometric tracking. For orbit operations, the Ka-band (~32 GHz) downlink is

used. In the case of the MRO, a third band, the UHF-band (~400 MHz), is used for forward and return link services for landed surface vehicles. UHF is also used for data relay during the entry, decent, and landing phase of such surface vehicles. [15]

The communication system of the MMRS consists of the following key components, which are elaborated upon in the following subsections.

- One high gain antenna to return the majority of the communication data
- Two low-gain antennas serving as a secondary means of communication
- Two transponders to facilitate the conversion of the received communication signals into a transmittal signal in the UHF, X-Band, and Ka-band frequencies
- Three amplifiers to amplify signals in the UHF, X-Band, and Ka-band frequencies

Gain is a measure of how tightly the radio beam of an antenna can be focused. Mathematically, it is the ratio of the power of a signal beam transmitted along a single direction by a signal of the same power sent in all directions. [15] This concept is applicable to high and low gain antennas. For a transmitting antenna, gain denotes the ability of the antenna to convert input power into radio waves focused in a specific direction. For a receiving antenna, gain denotes the ability of the antenna to convert radio signals from a specific direction into electrical power. Receiving and transmitting gain are identical. Peak gain refers to gain when no direction is specified, and is thus in the direction of the antenna's main lobe.

2.3.1 High Gain Antenna

High gain antennas are used to transmit high-power signals in a narrow beam. These antennas are more highly-directional than low gain antennas, and must be precisely oriented in order to achieve a signal with a receiver. For satellite applications, high gain antennas are used to return the majority of communication data collected to Earth from deep space locations. With respect to the MMRS, a high gain antenna will serve as the primary means of communication with Earth. High gain antennas generally take the shape of large parabolic dish antennas due to their ability to focus radio beams. The larger the collecting area of the dish, the higher the gain, and the higher data transfer rate the antenna will support. [15] The HGA for the MMRS will be a Cassegrain reflector capable of X-band uplink and downlink, and Ka-band downlink transmission.

Each spacecraft described in table 2.2 utilizes a HGA of the Cassegrain reflector type, which itself is a type of parabolic reflector. The max. and min. data transfer rate denotes the rate for the spacecraft at the minimum and maximum distances from Earth, respectively. For the MMRS, HGA X-band telemetry downlink parameters are provided in table 2.2 and 2.3. The values pertaining to the MMRS are derived in the design of experiments in section 2.7 of this document, in conjunction with the excel calculator provided in appendix A.1, and are further elaborated upon in appendix A.1. These values assume the MMRS is in position around Mars when Earth and Mars are at their furthest distances apart. The max. data rate assumes a distance of 100 million kilometers from Earth. [15] These calculations may be readily modified to assume the spacecraft is positioned around another planet. This is further elaborated upon in section 2.7.

Table 2.2 – High gain antenna system X-band telemetry downlink parameters of existing space probes and MMRS (part 1).

Spacecraft	Type	HGA diameter (m)	Peak gain (dB)	Max. data transfer rate	Min. data transfer rate	Transmit power (dBm)	Max. dist. from Earth (km)
Mars Reconnaissance Orbiter [15]	Parabolic reflector	3.0	46.7	6.00 Mbps	500 kbps	42.04	400e6
Mars Odyssey [16]	Parabolic reflector	1.3	38.3	256 kbps	8 kbps	41.4	400e6
Mars Global Surveyor [17]	Cassegrain reflector	1.5	39.0		21 kbps	44.23	400e6
Juno [18]	Parabolic reflector	2.5	44.5	200 kbps	40 bps	44.4	968e6
Cassini [19]	Parabolic reflector	4.0	46.6	166 kbps	14 kbps	43.00	2850e6
New Horizons [20]	Cassegrain reflector	2.1	42.0	2.00 Mbps	600 bps		4280e6
MMRS	Parabolic reflector	3.0	44.25	6.34 Mbps	528 kbps	44.40	400e6

Table 2.3 – High gain antenna system X-band telemetry downlink parameters of existing space probes and MMRS (part 2).

Spacecraft	Frequency (GHz)	EIRP (dB)	Half-power beamwidth (deg)	Eb/No available (dB)	Eb/No required (dB)	Space loss (dB)	G/T (dB)	C/N ₀ (dB)
Mars Reconnaissance Orbiter [21]	T: 8.40 R: 7.15	96.5	0.18					
Mars Odyssey [16]	T: 8.40 R: 7.15	44.6	1.9	35.85	2.31	-191.79	0.69	10
Mars Global Surveyor [17]	T: 8.42 R: 7.16	48.83	+/-0.8	5.53	2.31	-267.49	0.90	
Juno [18]	T: 8.40 R: 7.15	87.37	+/-0.25	2.91	-0.10	-284.46	1.96	10
Cassini [19]	T: 8.43 R: 7.18	88.81	0.635	1.94	0.31	-294.50	1.15	10
New Horizons [20]	T: 8.4 R: 7.2	83.0	1.0					
MMRS	T: 8.40 R: 7.15	85.65	1.0	20.21	9.60	-284.46	49.1	77.4

Note that in table 2.3 above, G/T refers to the ratio of receiver gain to temperature. Temperature refers to system noise temperature (SNT), which is influenced by antenna gain. C/No (also referred to as CNR) denotes carrier to noise density ratio.

Using a regression analysis, which considers the high gain antenna system X-band telemetry downlink parameters of existing spacecraft (provided in tables 2.2 and 2.3), and utilizing a design of experiments (provided in section 2.7), the parameters for the MMRS were calculated using the excel calculator shown in appendix A.1. The full results of these calculations are provided in appendices A.1 and A.2. Relevant parameters considered in performing the regression analysis are plotted in figures 2.1 and 2.2 below. Note, however, that these represent only a small sample of the parameters that could be plotted from the data in tables 2.2 and 2.3.

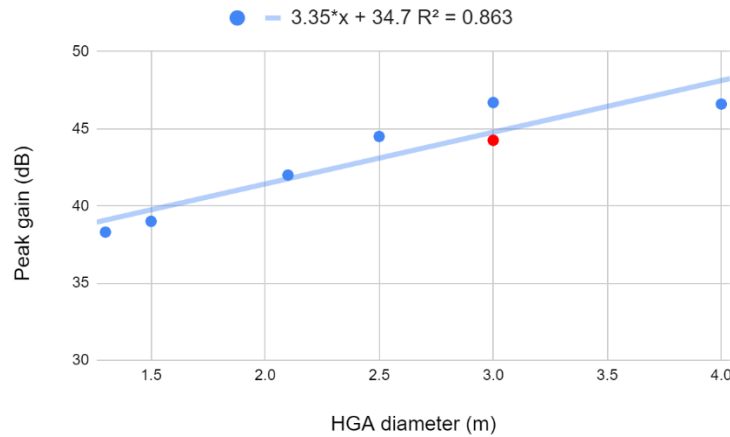


Figure 2.1 – Peak gain vs. HGA diameter for HGA X-band downlink of in-family space probes and MMRS (red).

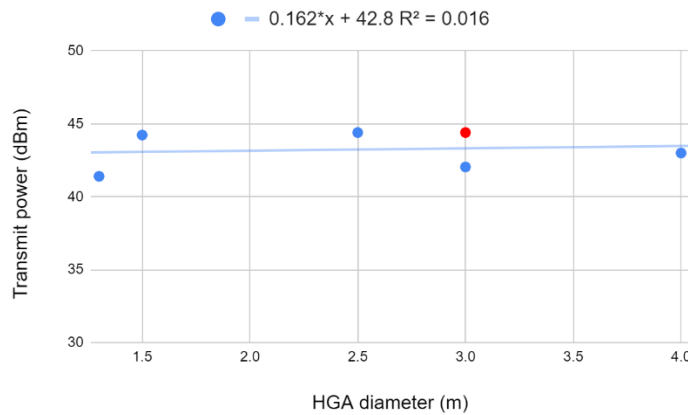


Figure 2.2 – Transmit power vs. HGA diameter for HGA X-band downlink of in-family space probes and MMRS (red).

Figure 2.1 plots peak gain versus high gain antenna diameter. The corresponding R^2 value of 0.863 indicates a good correlation. Figure 2.2 plots transmitter power versus high gain antenna diameter. The corresponding R^2 value in this case of 0.016 indicates poor correlation between

these variables. Plotting many of the other variables provided in tables 2.2 and 2.3 produces similarly poor correlations. This can be expected due to the disparate variables to consider when designing communication systems for disparate mission parameters.

The HGA used for X-band downlink will also be used for X-band uplink to receive data from the DSN antennas on Earth. Parameters of the X-band uplink are provided in table 2.4 below. These values were calculated using the excel calculator, and are further elaborated upon in appendix A.2 of this document.

Table 2.4 – High gain antenna system X-band command uplink parameters of existing space probes and MMRS.

Spacecraft	Type	HGA diameter (m)	Frequency (GHz)	Peak gain (dB)	Max. data transfer rate (bps)	G/T (dB)	Max. dist. from Earth (km)
Mars Reconnaissance Orbiter [15]	Parabolic reflector	3.0	7.15				400e6
Mars Odyssey [16]	Parabolic reflector	1.3	7.15	36.6	125	0.66	400e6
Mars Global Surveyor [17]	Cassegrain reflector	1.5	7.16	6.60	125	0.01	400e6
Juno [18]	Parabolic reflector	2.5	7.15	42.84	2000	0.11	968e6
Cassini [19]	Parabolic reflector	4.0	7.18	45.40	500	0.16	2850e6
New Horizons [20]	Cassegrain reflector	2.1	7.2				4280e6
MMRS	Parabolic reflector	3.0	7.15	44.44	2000	16.1	400e6

The MMRS will additionally possess a Ka-band downlink capability. The Ka-band (32 GHz) supports increased bandwidth and thus a higher data rate, compared to the X-band (8 GHz). This makes viable Ka-band communication highly desirable for deep space probes. The Mars Reconnaissance Orbiter served as a technology demonstrator to validate the use of Ka-band communications between deep space probes and Earth. As previously stated, the MRO was able to achieve data rates as high as 6 Mbps; far greater than that of any existing spacecraft. As such, the MMRS will be equipped with Ka-band downlink capabilities analogous to that of the Mars Reconnaissance Orbiter. The appropriate values are provided in table 2.5 below. Additional data was calculated and is provided in the excel calculator in appendix A.3. Note, however, that weather causes greater degradation of Ka-band signals than the X-band. Solutions to mitigate this were addressed in the design of the MRO communication system. [21] Note that the HGA will be used for both X-band and Ka-band communication.

Table 2.5 – Ka-band telemetry downlink parameters of existing space probes and MMRS.

Spacecraft	Frequency (GHz)	EIRP (dB)	Half-power beamwidth (deg)	Eb/No available (dB)	Eb/No required (dB)	Space loss (dB)	G/T (dB)	C/N ₀ (dB)
Mars Reconnaissance Orbiter [15]	32.0	101.3	0.18					
Mars Global Surveyor [17]	32.0	79.0					0.58	
MMRS	32.0	101.3	0.18	0.82	9.60	-296.08	60.7	68.7

2.3.2 Low Gain Antennas

Rather than send a highly-focused beam in a single direction, low gain antennas send less-focused radio signals in a much wider sweep of directions. As such, the signal received by the ground station is weaker, with a lower data rate, and is unable to carry as much information as a signal from an analogous high-gain antenna. However, the likelihood of the signal making contact with the ground station is much greater. Whereas is a spacecraft with a high gain antenna has to be precisely orientated for the signal to reach Earth, such precise orientation is not required when using a low gain antenna.

The MMRS will make use of two low gain antennas (one on opposite sides of the spacecraft) using X-band transmit and receive frequencies to provide total coverage around the entire spacecraft. Transition from usage of the low gain antennas to the high gain antenna as the means of primary communication begins at a fixed distance from Earth. For reference, this occurred at 2.7 AUs for Cassini. [19] Additionally, low gain antennas are commonly used as backups in situations where the high gain antenna cannot be used. [15] The low gain antennas of the MMRS will have heritage with the Mars Reconnaissance Orbiter, which also have heritage with the Juno spacecraft. Historical data for the LGA for various spacecraft is provided in table 2.6 below. Note that the LGA does not provide Ka-band capability.

Table 2.6 – Low gain antenna system X-band telemetry downlink parameters of existing space probes and MMRS.

Spacecraft	Type	Quantity	Frequency (GHz)	Gain (dB)	Total mass (kg)
Mars Reconnaissance Orbiter [15]	Horn	2	T: 8.40 R: 7.15	T: 8.4 R: 8.8	1.1
Mars Odyssey [16]	Patch	1 (up only)	7.15	R: 7.0	0.042
Mars Global Surveyor [17]	Patch	4 (2 up, 2 down)	T: 8.40 R: 7.15	T: 6.5 R: 6.5	1.1
Juno [18]	Horn	2	T: 8.40 R: 7.15	T: 7.7 R: 8.7	1.1
	Biconical horn	1	T: 8.40 R: 7.15	T: 6.5 R: 5.5	1.9
Cassini [19]	Horn	2	T1: 8.43 R1: 7.18 T2: 8.43 R2: 7.18	T1: 8.94 R1: 8.44 T2: 9.0 R2: 8.4	1.0
MMRS	Horn	2	T: 8.40 R: 7.15	T: 8.4 R: 8.8	1.1

2.3.3 UHF

The MMRS will additionally possess UHF capability. This will allow for data relay with planetary surface vehicles and EDL data relay and navigation support for arriving spacecraft. The UHF radio relay equipped on the MMRS will be the Electra UHF communications and navigation package, which has heritage with Mars spacecraft starting with the Mars Reconnaissance Orbiter. The Electra system includes a UHF antenna and two transceivers (each with a solid-state RF power amplifier). The UHF transmitter outputs 5 Watts, requiring an input power of 71 Watts. Electra can support data rates down to 1 kbps across a frequency band of 390 MHz to 450 MHz. The total mass of the Electra UHF subsystem totals 11.5 kg. The Electra UHF transceiver assembly is illustrated in figure 2.3 below. [15]

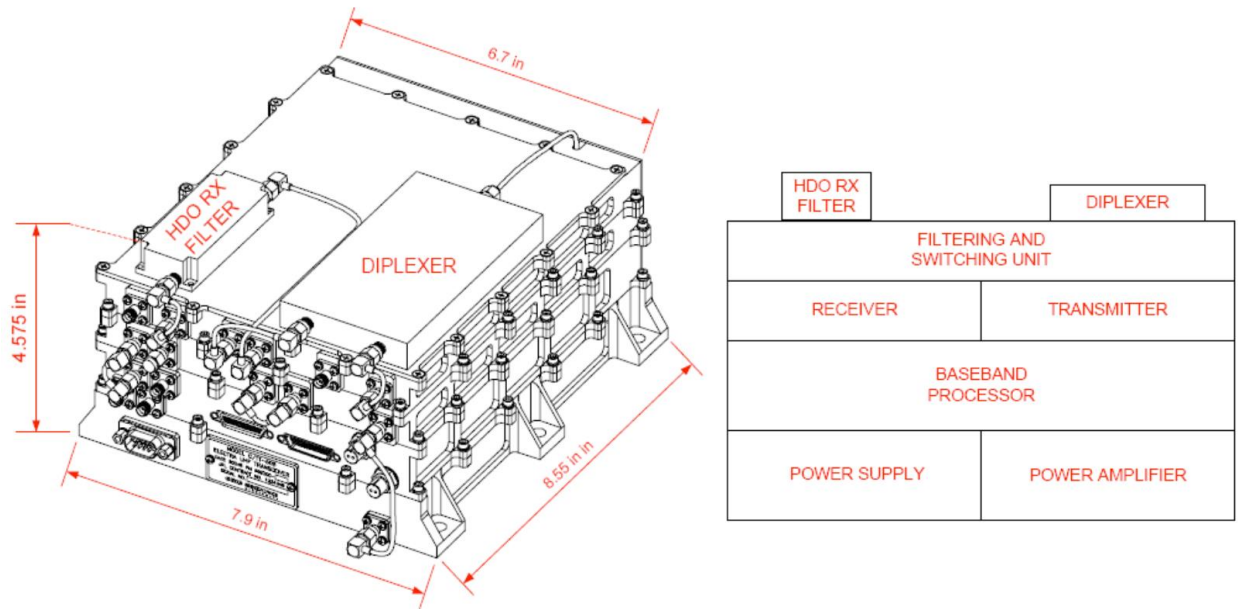


Figure 2.3 – Electra UHF transceiver assembly. [15]

2.4 Transponders & Amplifiers

2.4.1 Transponders

Transponders serve three functions. These include transmit/receive, transponding, and navigation. Transponders convert digital electrical signals into radio signal, which are then transmitted to the ground station on Earth. Conversely, transponders also convert radio signals to digital electrical signals for receiving commands from Earth. The transponding function denotes the ability to detect and automatically respond to a signal from Earth. The navigation function denotes the ability to transmit signals that provide navigational clues. [15]

Transponders in communication satellites serve as a link between the receiving and transmitting antennas of the satellite. Transponders commonly operate on the bent pipe principle, in which the received data is transmitted to the ground station with only amplification and a shift from uplink to downlink frequency. [22] This allows for data to be sent to Earth in near-real-time. However, satellites may also leverage on-board processing, where the received signal is demodulated, decoded, re-encoded, and modulated before transmission. [23] The bandwidth available for the communication system of a satellite is dependent upon the number of transponders. A link budget can be used to determine the bandwidth required to accommodate the amount required. [23]

The Small Deep Space Transponder (SDST) is a NASA-designed transponder purpose-built for use in deep space probes, having seen use onboard several spacecraft, including the Mars Reconnaissance Orbiter, Mars Odyssey, and Juno spacecraft. It is designed to handle communication downlink in the X and Ka-bands and uplink in the X-band. Given its successful

flight heritage, it will be the transponder utilized in the communication system of the MMRS spacecraft. Two SDST units will be equipped on the MMRS for redundancy, with only one being powered on at a time. Notable parameters of the Small Deep Space Transponder include the following. [24]

- Mass: 3.2 kg
- Power: 12.5 W nominal (receiver only)
- Envelope size: 7.13” X 6.55” x 4.50”
- Operating temperature: -40°C to 60°C

2.4.2 RF Amplifiers

A traveling wave tube amplifier (TWTA) is used to amplify and produce high-power RF microwave signals as part of the spacecraft transponder system. The MMRS will be equipped with three TWTAs, with heritage derived from the Mars Reconnaissance Orbiter [15]. Of these, two will operate at X-band frequencies (with only one bring powered on at a time for redundancy) and one will operate at Ka-band frequencies. Parameters of the MMRS TWTAs are provided in table 2.7.

Table 2.7 – TWTA parameters. [15]

Unit	Output power (W)	Mass (kg)
X-band TWTA (2)	100	1.9
Ka-band TWTA	35	0.8

Solid state amplifiers are another RF amplifier commonly found on spacecraft that were also investigated. Solid state amplifiers are more-reliable, lighter, and smaller. However, TWTAs have higher efficiency and must be used when RF output power requirements is too high at a given frequency for solid-state amplifiers. Additionally, solid-state amplifiers create the need for higher spacecraft complexity, whereas TWTAs shift the need for higher complexity to the ground station.

2.5 Communication Subsystem Sizing

To verify the calculated values for the sizing of the communication subsystem derived in appendix A, the analogous parameters of existing spacecraft were analyzed and compared against those of the MMRS. Values of total available mass and total available power for the communication subsystems of several existing spacecraft and the MMRS are provided in table 2.8. This data was then plotted in figure 2.4. The resulting R^2 value of 0.51 indicates a reasonable correlation. Note that the elimination of Mars Odyssey from the data set produces an R^2 value of 0.866. While this results in a significantly-better correlation, Mars Odyssey is considered in-family, and is thus included, with other factors contributing to its larger mass. Note that the values considered for mass and payload for the MMRS consider the combined values allocated

to both the communication subsystem and to the payload, as the payload is considered to be the communication subsystem.

Table 2.8 – Total communication system mass and power of existing spacecraft and MMRS.

Spacecraft	Total comm. mass (kg)	Total comm. power (W)
Mars Reconnaissance Orbiter [15]	107.70	359
Mars Odyssey [16]	23.55	282.3
MarCo CubeSats [22]	2.59	29
Juno [18]	83.20	187
Galileo [26]	73.9	191.6
MMRS	98.6	359
	12.3 (comms)	79.1 (comms)
	86.3 (payload)	279.9 (payload)

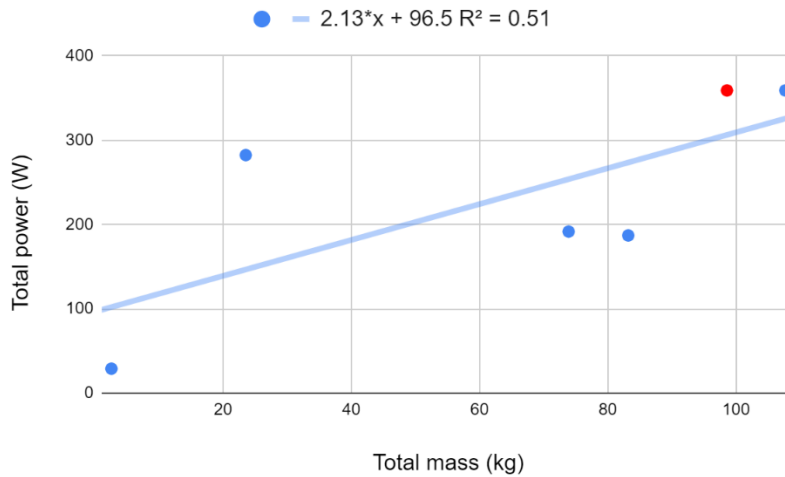


Figure 2.4 – Total available power vs. total available mass for existing spacecraft and MMRS (red).

Table 2.9 provides a mass breakdown of the communication subsystem by component. Note that a total mass of 98.6 represents the base-level MMRS. Table 2.10 provides a power breakdown of the communication subsystem by component, with a total power of 359 Watts allocated to the communication subsystem of the MMRS. Note, however, that there are 170.2 Watts of power allocated to the payload as reserve power (as is highlighted in table 8.2). This excess power exists to account for mission-specific payloads. This could include additional communication capability (such as the addition of laser communication, as discussed in chapter 9) or allow for the communication suite of future spacecraft to be upgraded over time for future MMRS missions. Note that values for power and mass are estimates based on systems used on current in-family spacecraft.

Table 2.9 – MMRS communication subsystem mass breakdown.

Communication subsystem mass breakdown (kg)	Electra UHF system	11.5
	HGA	50.3
	X-band TWTA	1.9
	Ka-band TWTA	0.8
	2 SDST	6.4
	2 LGA	2.2
	Wire harness & fasteners	5.1
	Miscellaneous (waveguides, diplexer, isolator, etc.)	20.4
Total subsystem mass (kg)		98.6

Table 2.10 – MMRS communication subsystem power breakdown.

Communication subsystem power breakdown (W)	Electra UHF system	71
	HGA	N/A
	X-band TWTA	172
	Ka-band TWTA	81
	2 SDST	16
	2 LGA	N/A
	Wire harness & fasteners	N/A
	Miscellaneous (HGA drive motors, USOs, etc.)	19
Total subsystem power (W)		359

2.6 Block Diagram

A block diagram describing the sizing of the high gain antenna of the communication subsystem is provided in figure 2.5 below. The input variables include desired data transfer per orbit (DT) and orbit period (P). The internal blocks include data rate (R) and power received (C). Calculations for the data rate were additionally investigated. These calculations, leveraging the same equation, are explored in the design of experiments in section 2.7 of this document.

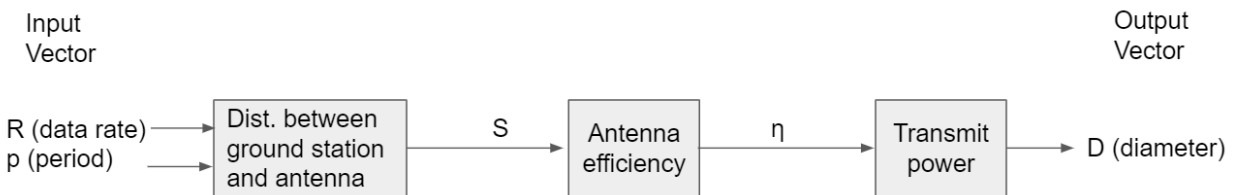


Figure 2.5 – General high-level block diagram for MMRS communication system HGA sizing.

2.7 Design of Experiments

A design of experiments was performed for the X-band downlink portion of the communication subsystem (as discussed in section 2.3.1) by leveraging the relationships of equation 2.8. These experiments assumed a constant, maximum distance from Earth to Mars (variable S in equation 2.7) of $4.00E11$ m, as described in table 2.2. Note that the values for factor α was kept constant at $6.15E27$. Efficiency factors of 0.55 and 0.70 were used, which denote the average lower and upper bounds of transmit antenna efficiency, respectively. Antenna diameter was varied between 3.0 m and 2.5 m, which are common values for in-family spacecraft. Transmitter power was varied between 42.04 dBm and 44.40 dBm, which are similarly common values. The observed value is data rate. The results of these experiments are provided in table 2.11 below. Note that additional design of experiments could be performed that vary the spacecraft distance from Earth. With increased distance from Earth, keeping all other values constant, data rate would decrease as per the inverse square law. Antenna diameter could additionally be observed when considering known values for data rate. Experiment 3 was selected for the design of the MMRS, which considers a data rate of 528 kbps at maximum Earth distance from Mars. This value is considered in table 2.2 in section 2.3 of this document. Similar analysis is applicable to the other data links discussed in this document.

Table 2.11 – Design of subsystems for communication subsystem.

Experiment number	Factor			
	D (m)	P (dBm)	η	R observation (kbps)
1	3.0	42.04	0.55	$\eta_1 = 500$
2	3.0	42.04	0.70	$\eta_2 = 636$
3	3.0	44.40	0.55	$\eta_3 = 528$
4	3.0	44.40	0.70	$\eta_4 = 672$
5	2.5	42.04	0.55	$\eta_5 = 347$
6	2.5	42.04	0.70	$\eta_6 = 442$
7	2.5	44.40	0.55	$\eta_7 = 367$
8	2.5	44.40	0.70	$\eta_8 = 467$

Using these experiments, and equations 2.8 and 2.9 below, the main effects for the communication subsystem were analyzed. Equations 2.8 and 2.9 yield an $M1$ and $M2$ value of $4.36e5$ and $5.54e5$, respectively. Subtracting $M2$ from $M1$ produces a main effect of $1.19e5$. This illustrates the main effect of antenna efficiency on data rate.

$$M1 = \frac{\eta_1 + \eta_3 + \eta_5 + \eta_7}{4} \quad (2.8)$$

$$M2 = \frac{\eta_2 + \eta_4 + \eta_6 + \eta_8}{4} \quad (2.9)$$

Where,

- M denotes the effect (kbps)
- η denotes the observation (constant)

Using equations 2.10 and 2.11, the interaction effects were analyzed. Equation 2.10 calculates the effect of a 3 m antenna diameter on data rate, yielding an N1 value of 1.40e5. Equation 2.11 calculates the effect of a 2.5 m diameter antenna on data rate, yielding an N2 value of 9.74e4. The average of equations 2.10 and 2.11 was then taken, resulting in a value of 1.19e5.

$$\eta_{D1} = \frac{(\eta_4 - \eta_3) + (\eta_2 - \eta_1)}{2} \quad (2.10)$$

$$\eta_{D2} = \frac{(\eta_6 - \eta_5) + (\eta_8 - \eta_7)}{2} \quad (2.11)$$

2.8 Verification & Validation

The tables 2.12 and 2.13 present information regarding the verification and validation of the communication subsystem. The listed requirements are designated as either “shall” or “should” requirements, and are then ranked on a scale of 1-10 as to the degree to which the requirements are verifiable, achievable, logical, integral, and definitive. [27] A verification method is then given for that requirement, as is an overall ranking, which is an average of the 5 aforementioned factors.

Table 2.12 – Communication subsystem verification and validation (part 1).

Category	System ID	Requirement Description	Justification
Comm.	1.1	Communications package shall be capable of relaying all data from a deep space probe to the Deep Space Network (DSN) antennas on Earth	Required for communication with spacecraft in deep space
	1.2	Shall provide uplink (command), downlink (telemetry), and navigation with the DSN	Required for optimal operation
	1.3	Shall communicate with Deep Space Network antennas using X bands and Ka bands	Required for optimal operation
	1.4	Should send and receive data at high rates compared to existing spacecraft	Required for optimal operation
	1.5	Shall have interoperability with NASA’s Deep Space Network at X-band frequencies (7.2 GHz uplink, 8.4 GHz downlink) and Ka-band frequencies (32 GHz uplink) for telemetry, tracking, and command [15]	Required for communication with spacecraft in deep space
	1.6	Should transmit at a rate of 200 kbps at Jupiter orbit [22]	Heritage with Juno spacecraft

Category	System ID	Requirement Description	Justification
Comm.	1.7	Should transmit at a rate of 6 Mbps at Mars orbit [15]	Heritage with MRO spacecraft
	1.8	Shall provide UHF forward-link and return-link relay services to landed planetary surface vehicles	Relay with planetary landers

Table 2.13 – Communication subsystem verification and validation (part 2).

Category	System ID	Shall / Should	Verifiable (1-10)	Achievable (1-10)	Logical (1-10)	Integral (1-10)	Definitive (1-10)	Verification Method	Overall (1-10)
Comm.	1.1	Shall	10	10	10	10	10	Analysis	10
	1.2	Shall	10	10	10	10	10	Analysis	10
	1.3	Shall	10	10	10	10	10	Analysis	10
	1.4	Should	10	8	10	10	10	RF testing	9.6
	1.5	Shall	10	10	10	10	10	RF testing	10
	1.6	Should	9	9	9	9	9	Analysis	9
	1.7	Should	9	9	9	9	9	Analysis	9
	1.8	Shall	10	10	8	10	10	10	Analysis

2.9 Test Plan

To test the communication subsystem, the Antenna Test Facility at the Johnson Spaceflight Center could be used. This facility possesses an anechoic chamber and an outdoor antenna range. The anechoic chamber is well-suited for satellite mockups with mounted antennas. The material covering the interior surfaces of the chamber is ideal for replicating the space environment, as it absorbs electromagnetic energy. Frequencies from 200 MHz to 40 GHz can be accommodated. [28]

2.10 Risk Assessment

A risk assessment was performed for the communication subsystem, which is shown in table 2.14 below. The rubrics used in determining these risk levels are provided in appendix C.1. The primary risk associated with the communication subsystem includes failure of the high gain antenna, as this is the only major part of the communication subsystem without a redundancy. While the low gain antennas would still be operable, failure of the high gain antenna would cripple the spacecraft, leaving it unable to perform its mission as designed. As the communication system has heritage, the risk of this occurring is considered minor.

Table 2.14 – Communication subsystem risk assessment.

Level	Risk	Mitigation
C,1	Transceiver failure	Redundancy & testing
C,1	Amplifier failure	Redundancy & testing
C,1	Low gain antenna failure	Redundancy & testing
E,1	High gain antenna failure	Testing & heritage

3.0 Power Subsystem

The design of the power subsystem for a spacecraft consists of the following four main steps. These include identifying requirements, selecting and sizing the power source, selecting and sizing the means of energy storage, and identifying a means of power distribution, regulation, and control. These topics are discussed below.

3.1 Requirements

When designing the power subsystem, the mission objectives and requirements must be defined in detail such that alternative architectures can be evaluated and compared. The operational and functional requirements of the power subsystem for the MMRS are outlined below.

- Operational Requirements
 - Shall provide, store, distribute, and control spacecraft electrical power
 - Shall provide sufficient power to the spacecraft over its operational lifetime (beginning to end of life) without excessive degradation
 - Shall provide power for average and peak electrical loads [29]
- Functional Requirements
 - Should produce 1068 watts of power at BOL
 - Should produce 966 watts of power at EOL
 - RTGs shall provide power to satellite subsystems at 30 volts DC

To develop a power budget, there are three primary steps. First, estimates must be derived for the power requirements of the bus subsystems for the spacecraft. If the spacecraft has multiple operating modes that differ in the amount of power they require, budgets must be created individually for each mode. Notably, peak power is of key importance. Secondly, battery sizing must be performed which takes into account the capacity and battery life cycle required. With battery size established, the recharge power of the battery can be calculated. Thirdly, subsystem degradation over time must be computed. [30]

The size of the power source is dependent upon the average electrical power required at end-of-life. Peak power is this average EOL power multiplied by a factor of 2 or 3. Note that not all subsystems will require peak power at the same time. The average EOL electrical power required dictates the size of the power-generating components, including the size of the solar array or radioisotope thermoelectric generators and battery size. The peak electrical power required dictates the size of the energy-storing components, including batteries, and the power distribution equipment. Mission life dictates the amount of design redundancy incorporated into the system, as well as battery capacity, battery charging, and solar array or RTG size. Orbital parameters dictate the amount of solar radiation that contacts the solar array. Spacecraft configuration dictates whether the solar panels are body-mounted or deployable. [29]

3.2 Power Sources

There are typically four main power sources used on spacecraft. These include photovoltaic cells (solar cells), static power sources, dynamic power sources, and fuel cells. Solar cells convert solar radiation into electrical energy and are commonly used on inner solar system spacecraft where solar radiation intensity is greatest. Static power sources utilize a radioactive heat source (commonly plutonium-238) and thermocouples to transform heat into electrical energy. These generally take the form of radioisotope thermoelectric generators (RTGs) and are most commonly used on outer solar system spacecraft. Dynamic power sources similarly use a heat source to produce electrical energy, though this is accomplished instead through the Brayton cycle or other similar cycles. Fuel cells convert chemical energy into electricity and are commonly utilized on manned space vehicles, including the Space Shuttle, and notably produce potable water as a waste product. This document will focus primarily on solar cells and RTGs. Thus, these power sources will be explained in more detail in subsequent sections of this document.

3.2.1 Solar Arrays

Spacecraft designed for use in the inner solar system are generally equipped with solar panels as the power source to recharge the batteries of the spacecraft. Conventional photovoltaic solar panels for space applications achieve an energy conversion efficiency of approximately 26%. The solar cells themselves are composed of crystalline silicon and gallium arsenide and degrade at a rate of 0.6% per year due to solar radiation absorption. [8] As a rule of thumb, the solar array of a spacecraft is assumed to produce approximately 100 W/m² of solar array area. [29]

The relationships between several parameters relevant to solar array sizing and function are described in the equations below. [29] Other key equations pertaining to battery sizing are provided in subsequent subsections. [13]

$$P_{sa} = \left(\frac{P_e T_e}{X_e} + \frac{P_d T_d}{X_d} \right) \frac{1}{T_d} \quad (3.1)$$

Where,

- P_{sa} denotes how much power the solar array must provide during daylight hours to provide enough power for a full orbit (W).
- P_e and P_d denote the satellite's power requirements during eclipse and daylight, respectively (W)
- T_e and T_d denote period lengths per orbit (sec).
- X_e and X_d denote the efficiency of power transmission from the solar arrays to the batteries. ($X_e = 0.65$ and $X_d = 0.85$)

$$A_{sa} = \frac{P_{sa}}{P_{EOL}} = \frac{P_{sa}}{P_0 L_d^2 \cos\theta} \quad (3.2)$$

Where,

- A_{sa} denotes solar array area (m^2)
- P_{EOL} denotes array performance per unit area at end of life (W)
- P_0 denotes average array performance (W)
- θ denotes sun incidence angle
- P_0 denotes an efficiency factor

$$P_{EOL} = P_{BOL} L_d \quad (3.3)$$

Where,

- P_{BOL} denotes array power per unit area at beginning of life (W)
- L_d denotes lifetime degradation

$$L_d = (1 - \text{degradation/year})^{\text{Satellite life}} \quad (3.4)$$

The effectiveness of solar panels as a means of generating electricity for spacecraft decreases in effectiveness with spacecraft distance from the sun. For reference, Earth is 150 million kilometers from the sun, Mars is 227 million kilometers from the sun, and Jupiter is 778 million kilometers from the sun. The mean solar irradiance (solar flux) for an orbiting spacecraft is 1367 W/m^2 for Earth, 588.6 W/m^2 for Mars, and 50.5 W/m^2 for Jupiter. This follows from equation 3.5 below. [31]

$$H_0 = \frac{R_{sun}^2}{D^2} H_{sun} \quad (3.5)$$

Where,

- H_0 denotes solar radiation intensity (W/m^2)
- R_{sun} denotes radius of the sun ($695 \times 10^6 \text{ m}$)
- D denotes distance from the sun (m)
- H_{sun} denotes power density at the surface of the sun ($64 \times 10^6 \text{ W/m}^2$)

Table 3.1 below provides the parameters used in solving equation 3.1. These parameters are referenced in the subsequent calculations performed in this section and are the basis of calculations provided in appendices A.4 and A.5.

Table 3.1 – Solar power parameters for MMRS at Mars and Jupiter, from equation 3.1.

	Mars	Jupiter
P_e (W)	960.1	960.1
T_e (sec)	666.0	462.2E+04
X_e	0.65	0.65
P_d (W)	960.1	960.1
T_d (sec)	666.0	462.2E+04
X_d	0.85	0.85
P_{sa} (W)	1573.5	1200.1

Table 3.2 provides the required spacecraft power and the solar array area for several spacecraft, in addition to the calculated values for the MMRS. Note that, due to the multi-mission nature of the MMRS, values for solar array area at Mars and Jupiter are provided. However, given the variability of solar radiation intensity throughout the solar system, this calls into question the viability of a solar-powered spacecraft, as will be discussed via trade study in subsequent sections. These values are additionally plotted in figure 3.1.

To calculate the required solar array area considering orbit about Mars, the orbit of the Mars Reconnaissance Orbiter was used as a baseline. The orbital period of the MRO is 111 minutes. The maximum eclipse time of the MRO is 21 minutes. [32] Additionally, a mission duration of 17 years was assumed, based on power requirements (as will be discussed further in subsequent sections). For Mars orbit, and accounting for a mean solar irradiance at Mars of 588.6 W/m^2 , the solar array area was calculated to be 27.9 m^2 . These values were calculated using equation 3.2 and the excel calculator sheet provided in appendix A.4.

To calculate the required solar array area considering orbit about Jupiter, the orbit of the Juno spacecraft was used as a baseline. The initial orbital period of Juno is 77,040 minutes. The maximum eclipse time of Juno is 0 minutes, as the orbit is such that the spacecraft is never in eclipse. [33] A mission duration of 17 years was additionally considered. For Jupiter orbit, and accounting for a mean solar irradiance at Jupiter of 50.5 W/m^2 , the solar array area was calculated to be 247.9 m^2 . These values were calculated using equation 3.2 and the excel calculator sheet provided in appendix A.5. Note that a solar panel efficiency of 26% is considered. This value is the efficiency of the solar panels of the Mars Reconnaissance Orbiter. However, as solar cell technology has advanced since 2005 (the solar panels used on Juno being a notable example), this efficiency likely could be improved upon.

Note that the mission duration plays a large effect in determining solar array area. The MMRS values shown in table 3.2 reflect a 17-year mission duration. Most space probes have a mission duration of approximately 5 years, but may continue operation for far longer periods than intended, albeit with decreased power generating capability. For reference, the original mission duration of the Mars Reconnaissance Orbiter was 5 years, but it continues to operate 17 years post-launch. [34] At a more-reasonable 8-year mission duration, the solar array area of the MMRS at Mars and the MMRS at Jupiter are 20.6 m^2 and 175.7 m^2 , respectively. As these

values agree closely with those found in the literature of analogous spacecraft solar array areas, the values scaled up for a 17-year mission duration may similarly be considered in agreement.

Table 3.2 – Power system parameters of existing solar-powered spacecraft and MMRS.

Spacecraft	Power required (W)	Solar array area (m ²)
Mars Reconnaissance Orbiter [34]	1000	20
Mars Odyssey [35]	750	10
Mars Global Surveyor [36]	980	13.3
Mars MAVEN [37]	1135	12
Juno [38]	435	60
MMRS (at Mars)	960	27.9
MMRS (at Jupiter)	960	247.9

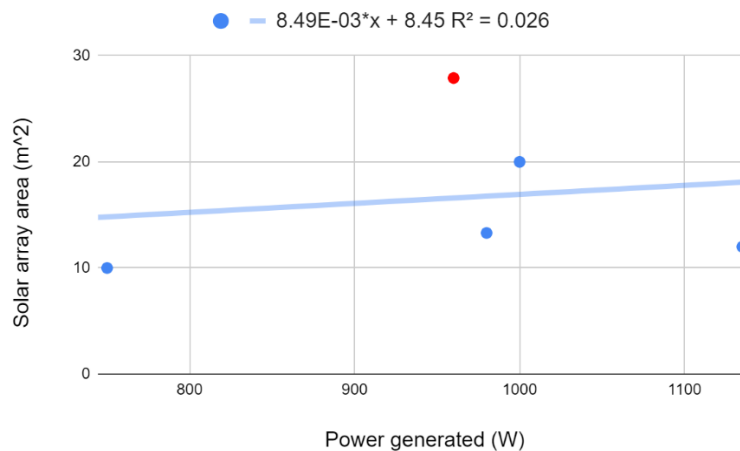


Figure 3.1 - Power generated by solar array vs. solar array area for Mars orbiters and MMRS (red).

As is shown in table 3.2, the solar array area for the Jupiter-orbiting Juno spacecraft is several times larger than the largest array size for Mars-orbiting spacecraft, and yet generates a fraction of the power. As a result, the values for Juno are not represented on figure 3.1, as it is not considered in-family for Mars-orbiting spacecraft. The trendline for Mars orbiting spacecraft indicates an R^2 value of 0.026. While this indicated a poor correlation, there are several points to note, which are described as follows. The mission duration plays a large factor, as mentioned previously. Solar array efficiency has increased in the past several decades, so spacecraft launched earlier may require larger solar arrays. Mission architecture and orbit parameters affect solar array size. Also of note is the ambiguity in the power generated by the solar arrays of the Mars Reconnaissance Orbiter; several reputable sources list the power generated as being both 1000 W and 2000 W. For this document, 1000 W was assumed. For reference, calculated solar array size for the MMRS in orbit of Mars and Jupiter are also provided in table 3.2.

Assuming the use of deployable solar panels (rather than cylindrical or omnidirectional body-mounted) for a Mars-orbiting MMRS, the total added mass of this solar array system is 153.4 kg.

This is the lightest solar array configuration, and includes the mass of the arrays themselves, the power control unit, regulators and converters, and wiring. For a Jupiter-orbiting MMRS, the total solar array system mass is increased to 649.4 kg. These values are further detailed in appendices A.4 and A.5, respectively. Given an MMRS dry mass of 492 kg (as will be discussed in chapter 6), an added solar array mass of 649.4 kg is prohibitively large when considering the entire system. As solar array efficiency additionally varies between locations within the solar system, radioisotope thermoelectric generators will be explored in a subsequent section of this document.

3.2.2 Batteries

The power subsystem of a spacecraft must store energy in rechargeable batteries. Batteries must be capable of surviving the harsh environment of space in addition to the shocks, vibrations, and accelerations experienced during launch. Radiation resistance and the ability to operate in temperatures as low as -80°C are required. For spacecraft applications, batteries are required to deliver maximum electrical energy while minimizing mass and volume. Spacecraft batteries must generally experience more than 30,000 cycles (for orbiting spacecraft) and have a long active shelf life of between seven and ten years (for planetary probes). [6] Modern interplanetary spacecraft require between 300 W and 2.5 kW of electrical power for operation. [8] Most modern spacecraft leverage lithium-ion batteries for the significantly higher energy density, lower discharge rates, and higher coulombic efficiency they afford compared to the nickel-hydrogen batteries commonly used in 1990s-era spacecraft. [7]

Many RTG-powered spacecraft, including Cassini and New Horizons, powered their systems directly off of an RTG, rather than using a battery. Others, like Galileo, utilized an RTG to recharge lithium-sulfur batteries that powered its systems. [39] Battery data for existing spacecraft and the MMRS are illustrated in table 3.3 below. Note that the amount of energy stored in each battery is given in ampere-hours (though watt-hours could also be used). Multiple batteries may be connected in parallel to increase watt-hour storage capacity, while connecting in series offers increased voltage. [29]

Table 3.3 – Battery data for existing spacecraft and MMRS.

Spacecraft	Electric charge (amp-hour)	Type	Quantity	Voltage (V)
Mars Reconnaissance Orbiter [34]	50	Ni-H ₂	2	32
Mars Odyssey [35]	16	Ni-H ₂	1	
Mars Global Surveyor [36]	20	Ni-H ₂	2	28
Mars MAVEN [37]	55	Li-ion	2	28
Juno [38]	55	Li-ion	2	28
Galileo [40]	20	Li-ion	3	37
MMRS (theoretical)	44.6	Li-ion	2	30

Of particular concern in battery selection is quantity, physical size, mass, voltage, current load, duty cycle, depth of discharge, cost, shelf life, and reliability, among other factors. [29] These parameters for the design of a theoretical battery candidate for the MMRS are explored in table 3.4. Using these parameters, battery capacity can be determined using equation 3.6. Note that battery units can be designed and fabricated by private contractors that meet the requirements of the space mission. A minimum of two batteries is generally advised for redundancy. [29] The relevant values are provided in appendix A.7 of this document.

$$C_r = \frac{P_e T_e}{(DOD)Nn} \quad (3.6)$$

Where,

- C_r denotes battery capacity (Watt-hours)
- DOD denotes depth of discharge
- N denotes number of batteries
- n denotes battery-to-battery load transmission efficiency
- P_e denotes average eclipse load (Watts)
- T_e denotes eclipse duration (min)

Table 3.4 – Battery parameters for theoretical MMRS battery candidate.

Mission length	17 years
Cell type	Secondary (rechargeable)
Battery type	Li-ion
Voltage	30 V
Number of batteries (N)	2
Transmission efficiency (n) [29]	0.90
Eclipse load (P_e)	960.1 W
Eclipse duration $T_{e, Mars}$ (T_e)	21 min
Total battery capacity (C_r)	1247.9 W-hr (44.6 A-hr)
Mass of batteries (kg)	25.0

As a solar-powered design was shown to be unfeasible in the previous section, RTGs (as will be discussed in the subsequent section) will be utilized for power generation for the MMRS. Thus, the MMRS will not carry an onboard battery and will instead use a shunt regulator unit to maintain a steady input from the RTGs. This is acceptable as RTG output power is predictable. Excess power produced from the RTGs will be dissipated.

3.2.3 Radioisotope Thermoelectric Generators

For spacecraft operating in the outer solar system, where the distance from the sun is dramatically higher, radioisotope thermoelectric generators (RTGs) are commonly used for power generation. Radioisotope thermoelectric generators contain several kilograms of an isotopic mixture of radioactive plutonium-238 in the form of individual pellets that serve as a

source of heat. This heat is converted into electricity by means of an array of thermocouples composed of silicon-germanium. Excess waste heat is expelled into space via radiation using metal fins. RTG placement relative to infrared detecting science instruments must be considered due to the waste heat they emit. [8] For reference, the RTGs powering NASA’s Galileo spacecraft are each mounted at the end of a 5-meter-long boom. [26]

The General-Purpose Heat Source Radioisotope Thermoelectric Generator (GPHS-RTG) is a specific RTG that has seen use in several outer solar system probes over the past several decades, having powered the Galileo, Cassini, and New Horizons spacecrafts. The GPHS-RTG consists of a cylindrically-shaped module with a diameter of 0.422 m, a length of 1.14 m, and a mass of approximately 55.9 kg. [41] Each GPHS-RTG unit is designed to produce electrical power at a nominal rate of approximately 250 watts to 300 watts at mission start. This rate decreases by 7.2 watts to 4 watts per year. These modules may be stacked together to meet spacecraft power requirements. [39] The Cassini probe, for example, utilized 3 for a total beginning of life power output of 885 watts. [42] This is illustrated in table 3.5 below. A diagram illustrating the components of a GPHS-RTG is provided in figure 3.2. [41]

Table 3.5 – RTG data for existing spacecraft and MMRS.

Spacecraft	Power produced (W)	Number of RTGs	Voltage (V)	Type
Galileo [26]	570 (BOL) 493 (arrival) 410 (EOL)	2	30	GPHS-RTG
Cassini [43]	885 (BOL) 663 (EOL)	3	30	GPHS-RTG
New Horizons [44]	250 (BOL) 202 (arrival)	1	30	GPHS-RTG
MMRS	1068 (BOL) 966 (EOL)	3	30	MMRTG

The Multi-Mission Radioisotope Thermoelectric Generator (MMRTG) is a more-recent iteration on the concept that utilizes thermocouples composed of the cobalt arsenide (CoAs₃) material skutterudite. These thermocouples can operate at a smaller temperature difference than the tellurium-based thermocouple design of the GPHS-RTG. This enables an otherwise similar RTG to generate 25% more power at mission start, and at least 50% more power after seventeen years in operation. As such, the MMRTG will be the RTG variant used in the MMRS.

The MMRTG consists of a cylindrically-shaped module with a diameter of 0.668 m, a length of 0.642 m, and a mass of approximately 43.6 kg. [45] Utilizing three MMRTGs, the MMRS will have a combined beginning of life power production capability of 1068 watts. This considers a nominal electrical power capability of 356 watts per MMRTG unit, which is approximately 25% more than the average nominal electrical power generating range of the GPHS-RTG. As a 17-year operational lifespan is assumed for the MMRS, this yields an end-of-life power production capability of 966 watts, as described in table 3.5.

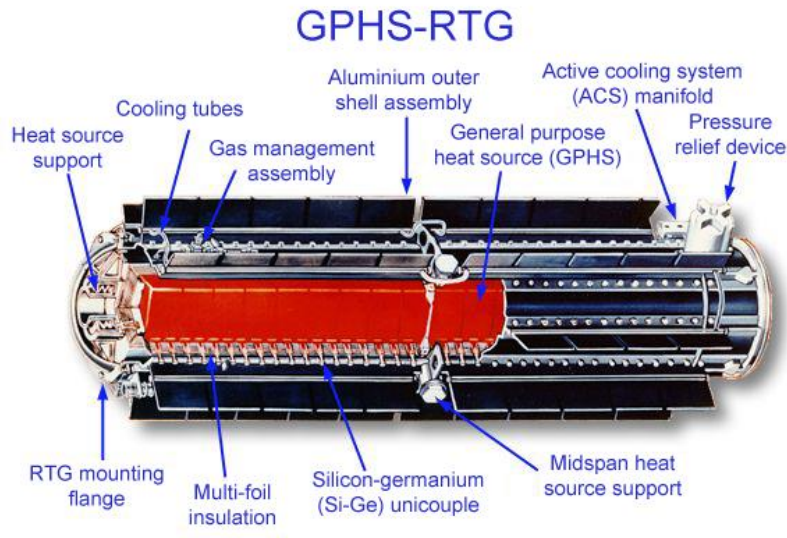


Figure 3.2 – Diagram of the GPHS-RTG used on Cassini. [41]

3.2.4 Power Breakdown By Subsystem

The power requirements for each of the five subsystems focused on in this document (in addition to a generalized ACS and C&DH) are provided in table 3.6 below. These values were initially derived as a percentage based on existing spacecraft of comparable mass, with values adjusted as necessary as each subsystem was further developed. [46] These values are further explored in appendix A.11 of this document. The total spacecraft power required, including a margin of 192 W, is 960.1 W. This requirement is easily met by the electrical power surplus output of 1068 W produced by the three MMRTGs, as described in table 3.5. At an end-of-life of 17 years, the MMRTGs are projected to produce 966 W of electrical power, considering a decay rate of 2.0 W per year per RTG. Operation beyond this point is possible, with subsystems powered-down, or operated sequentially, as necessary.

Table 3.6 – Power subsystem sizing breakdown.

Subsystem	Power (W)
Communication power	79.1
Power	110.7
Propulsion power	19.0
Thermal power	19.0
Structure power	0
ACS	63.9
C&DH	26.4
Margin`	192
Payload power	450
Total power required	960.1

The payload power requirement is assumed to be 450 W. This value is derived in appendix A.11 of this document and denotes power allocated to the communications payload.

3.2.5 Power Distribution, Regulation, & Control

The design of the power distribution system is beyond the scope of this document. However, a brief overview will be presented. The power distribution system of a spacecraft consists of cabling, fault protection, switching equipment to turn power on or off (often consisting of mechanical relays), and command decoders. The design of the power distribution system is influenced by the power source, load requirements, and system functions, while also accounting for cost, reliability, and the minimization of power losses.

The different subsystems of the spacecraft may have various voltage requirements. All power loads must be converted to the spacecraft bus voltage. Power converters are used to connect loads requiring voltage conversion or loads that are susceptible to noise. Such converters prevent load failures from damaging the power-distribution system. Direct current (DC) systems are the most commonly-used on spacecraft as spacecraft power is generated as DC, and alternating current (AC) would require added mass. The cabling that connects the power system of the spacecraft accounts for 10-25% of the system's mass. Note that cable harness length must be minimized to reduce voltage drops.

Fault protection focuses on the detection, isolation, and correction of electrical faults that could pose a mission-critical threat to the spacecraft. Such faults generally consist of short circuits, which may draw excessive power. This may additionally stress cables and drain stored energy. Faults may be isolated with fuses and detected with fault-detection circuits. [29]

3.3 Block Diagrams

A block diagram of a theoretical solar-powered power subsystem is provided in figure 3.3 below. The input variables are orbital period (p), spacecraft bus power at end-of-life (P_{bus_EOL}), and payload power at end-of-life (P_{PL_EOL}). These variables flow into solar array size and battery size. The output vector is the solar array power produced during daylight to supply power for the entire orbit (P_{sa}). The governing equations used for these calculations were provided in section 3.2.

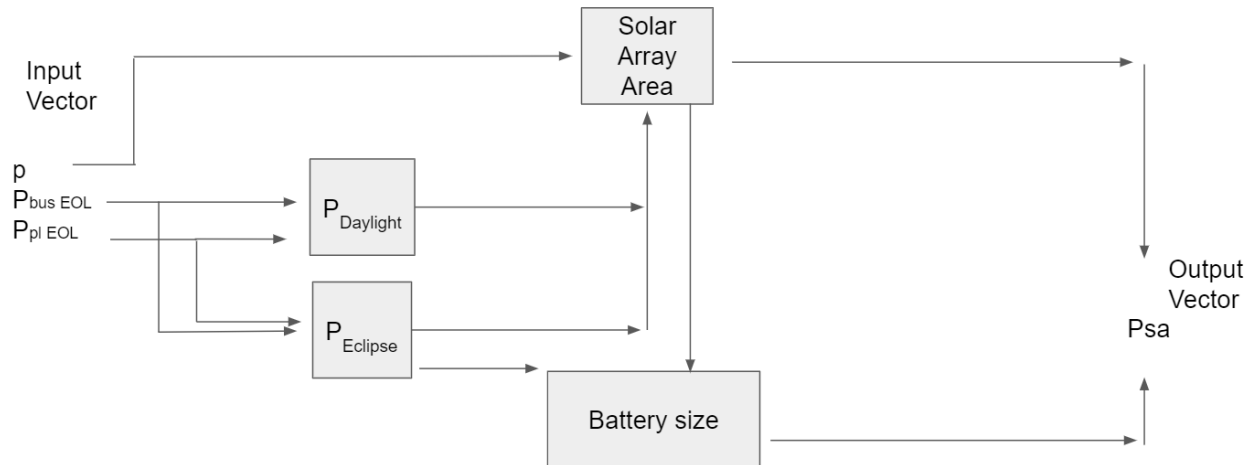


Figure 3.3 – High-level block diagram of the power system (theoretical solar array).

A block diagram of the actual RTG-powered power subsystem is provided in figure 3.4. The input variables of bus and payload power, as well as margin, for each subsystem were calculated as shown in table 3.6. This system does not include solar arrays or batteries, and is thus independent of orbit parameters (i.e., periods of eclipse and daylight). Note that each RTG decays at a rate of 2 W per unit per year. Excess thermal energy generated by the RTG is rejected as waste heat.

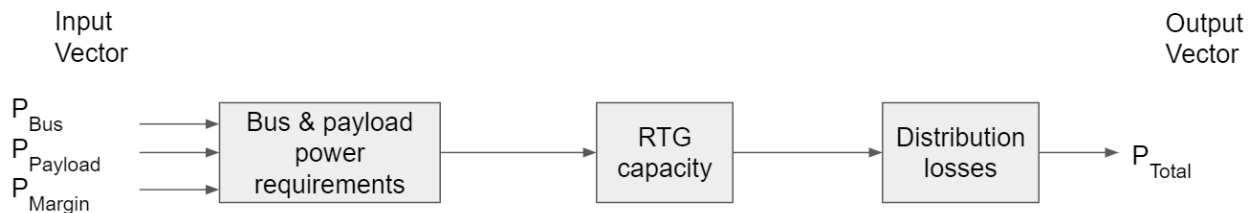


Figure 3.4 – High-level block diagram of the power system (RTG).

3.4 Design of Experiments

A design of experiments was performed for the power subsystem in determining whether a solar array would be a viable option for a power source. The relationship illustrated in equation 3.2 was leveraged to determine solar array area.

Two values for P_{sa} (power produced by the solar array), P_o (efficiency factor), and L_d (degradation factor) were chosen, with a total of eight experiments performed. The L_d factor chosen was assumed to be for a 17-year mission (considering both 3.75% and 2.75% degradation per year), as per equation 3.4. A value for θ (representing the solar incidence angle) of 23.5 degrees was assumed. This is generally considered to be the worst-case solar incidence angle for a Mars-orbiting spacecraft. A P_o efficiency factor of 0.148 and 0.185 was assumed based on the satellites observed. Varying these parameters generated a range of potential P_{sa} values. The

lowest Asa for a generated power of 1000 W was observed in experiment 4, with a value of 19.03. The Asa value in experiment 1 corresponds to the value provided in table 3.2, considering a 6.6 % error. Note that the value in table 3.2 is scaled to account for a 17-year mission duration. These values are provided in table 3 below.

Table 3.7 – Design of experiments for power subsystem for theoretical Mars solar array.

Experiment number	Factor			
	Psa (W)	Po (W/m ²)	Ld	Asa observation (m ²)
1	1000	90	0.682	$\eta_1 = 26.05$
2	1000	90	0.757	$\eta_2 = 21.14$
3	1000	100	0.682	$\eta_3 = 23.44$
4	1000	100	0.757	$\eta_4 = 19.03$
5	750	90	0.682	$\eta_5 = 19.54$
6	750	90	0.757	$\eta_6 = 19.86$
7	750	100	0.682	$\eta_7 = 17.85$
8	750	100	0.757	$\eta_8 = 14.27$

Using these experiments, and equations 3.7 and 3.8 below, the main effects for the power subsystem were analyzed. Equations 3.6 and 3.7 yield an M1 and M2 value of 21.7 and 17.6, respectively. Subtracting M2 from M1 produces a main effect of 4.1. This illustrates the main effect of power required on solar array area.

$$M1 = \frac{\eta_1 + \eta_3 + \eta_5 + \eta_7}{4} \quad (3.7)$$

$$M2 = \frac{\eta_2 + \eta_4 + \eta_6 + \eta_8}{4} \quad (3.8)$$

Where,

- M denotes the effect (W)
- η denotes the observation (m²)

Using equations 3.9 and 3.10, the interaction effects were analyzed. Equation 3.9 calculates the effect of power required with an efficiency factor of 100. Equation 3.10 calculates the effect of power required with an efficiency factor of 90. The average of equations 3.9 and 3.10 was then taken, resulting in an efficiency factor-area interaction of 4.1 m².

$$\eta_{Psa1} = \frac{(\eta_4 - \eta_3) + (\eta_2 - \eta_1)}{2} \quad (3.9)$$

$$\eta_{Psa2} = \frac{(\eta_6 - \eta_5) + (\eta_8 - \eta_7)}{2} \quad (3.10)$$

A design of experiments could similarly be completed for the design of the solar array of a Jupiter-orbiting spacecraft. However, as the analysis which showed such an array to be non-feasible for outer solar system locations was conducted earlier, this is omitted.

3.5 Verification & Validation

Tables 3.8 and 3.9 present information regarding the verification and validation of the power subsystem. The requirements are designated as either “shall” or “should” requirements, and are then ranked on a scale of 1-10 as to the degree to which the requirements are verifiable, achievable, logical, integral, and definitive. [27] A verification method is then given for that requirement, as is an overall ranking, which is an average of the 5 aforementioned factors.

Table 3.8 – Power subsystem verification and validation (part 1).

Category	System ID	Requirement Description	Justification
Power	2.1	Shall provide, store, distribute, and control spacecraft electrical power	Required for optimal operation
	2.2	Shall provide sufficient power to the satellite over its operational lifetime (beginning to end of life) without excessive degradation	Required for optimal operation
	2.3	Shall provide power for average and peak electrical loads [29]	Required for optimal operation
	2.4	Should produce 1068 watts of power at BOL	Power output of RTG units
	2.5	Should produce 966 watts of power at EOL	RTG decay of 2.0 W per RTG per year
	2.6	RTGs shall provide power to satellite subsystems at 30 volts DC	DC voltage produced by MMRTG

Table 3.9 – Power subsystem verification and validation (part 2).

Category	System ID	Shall / Should	Verifiable (1-10)	Achievable (1-10)	Logical (1-10)	Integral (1-10)	Definitive (1-10)	Verification Method	Overall (1-10)
Power	2.1	Shall	7	10	10	10	8	Load testing	9.0
	2.2	Shall	8	10	10	10	8	Analysis	9.2
	2.3	Shall	8	10	10	9	9	Load testing	9.2
	2.4	Should	10	10	9	9	9	Load testing	9.4
	2.5	Should	8	10	10	9	9	Analysis	9.2
	2.6	Shall	10	10	10	10	10	Load testing	10.0

3.6 Test Plan

To test the power subsystem, loading of the electrical system must be performed. There are a number of independent commercial companies that perform such testing for satellite applications. Ametek Programmable Power utilizes Power Special Test Equipment (PSTE) to provide DC power and loading to the electrical systems of satellites for functional testing. [47]

3.7 Risk Assessment

A risk assessment was performed for the power subsystem, which is shown in table 3.10 below. The rubrics used in determining these risk levels are provided in appendix C.1. The risks associated with the power subsystem include electrical faults that could pose a mission-critical threat to the spacecraft. Such faults generally consist of short circuits, which may draw excessive power. This may additionally stress cables and drain stored energy. As the power system has heritage with the New Horizons spacecraft, these risks are considered minor.

Table 3.10 – Power subsystem risk assessment.

Level	Risk	Mitigation
C,2	Wire jacket failure	Isolation checks
C,2	Excessive current draw	Testing / Fuses
B,1	EM discharge	Grounding
C,2	Short circuit	Fuses / Fault-detection circuits

4.0 Propulsion Subsystem

The propulsion subsystem of a satellite is used to transfer the satellite into different orbits or trajectories for mission operations and to provide thrust for attitude control and orbit correction. The design of the propulsion subsystem for a spacecraft consists of the following six main steps. These are discussed in detail in subsequent sections. [48]

1. Defining the spacecraft propulsion functions (i.e., orbit insertion, orbit maintenance, or attitude control)
2. Defining a delta-v budget and thrust level constraints for orbit maintenance
3. Defining total impulse, duty cycles, and mission life requirements
4. Defining type of propulsion system (i.e., solid, bi-propellant, or electric)
5. Defining key parameters, including specific impulse (Isp), propellant mass and propellant volume
6. Estimating the total mass and power requirements of the system

4.1 Requirements

When designing the propulsion subsystem, the mission objectives and requirements must be defined in detail such that alternative architectures can be evaluated and compared. Key performance requirements include thrust and specific impulse. Key physical characteristics include system mass, size, and volume, which are driven by the performance and efficiency of the propulsion system. The operational and functional requirements of the propulsion system for the MMRS spacecraft are outlined below. These requirements are further elaborated on in section 4.6.

- Operational Requirements
 - Orbital insertion thruster shall propel the spacecraft into station orbit
 - Trajectory correction thrusters shall fire in long-duration bursts to correct the trajectory of the spacecraft
 - Attitude control thrusters shall fire in quick bursts to gently nudge the spacecraft into the desired orientation
 - All thrusters shall operate until spacecraft end of life
- Functional Requirements
 - Orbital insertion thruster should produce 1020 N of thrust
 - Trajectory correction thrusters should provide 22 N of thrust each
 - Attitude control thrusters should provide 4.45 N of thrust each
 - Propellant tanks shall hold 1123.9 kg of propellant

4.2 Governing Equations

The key parameters for the propulsion subsystem include thrust and specific impulse. These parameters are coupled with mass flow rate, exit velocity, and exit pressure. Delta-v is also of importance, as velocity change is a primary measure of system performance for a given mission. Equations for these parameters are included below. [48] An excel calculator was used to calculate the necessary parameters for engine sizing. The results of these calculations are provided in appendix A.7. The relevant equations used in the Excel calculator for sizing the propulsion subsystem are provided below.

$$F = \dot{m}v_e + A_e(P_e - P_{inf}) \quad (4.1)$$

Where,

- F denotes thrust applied by the engine (N)
- \dot{m} denotes propellant mass flow rate (kg/sec)
- V_e denotes propellant exhaust velocity (m/s)
- P_e denotes gas pressure at the exit of the nozzle (Pa)
- P_{inf} denotes ambient pressure (Pa)

$$I_{sp} = \frac{F}{\dot{m}g_o} \quad (4.2)$$

Where,

- I_{sp} denotes specific impulse: a measure of the energy content of the propellant (sec)
- g_o denotes acceleration of gravity (m/s^2)

$$\dot{m} = p_c A^* \sqrt{\frac{\gamma}{RT_c} \left(\frac{2}{\gamma + 1} \right)^{\frac{\gamma+1}{\gamma-1}}} \quad (4.3)$$

Where,

- A^* denotes nozzle throat area (m)
- R denotes the gas constant (8.32 J/mol/K (universal))
- T_c denotes chamber temperature (K)
- γ denotes specific heat ratio (C_p / C_v)

$$V_e = \sqrt{\frac{2\gamma}{\gamma - 1} RT_c \left(1 - \left(\frac{P_e}{P_c} \right)^{\frac{\gamma-1}{\gamma}} \right)} \quad (4.4)$$

Where,

- P_e denotes exit pressure (Pa)
- P_c denotes chamber pressure (Pa)

$$\Delta V = gI_{sp} \ln\left(\frac{m_o}{m_o - m_p}\right) = gI_{sp} \ln\left(\frac{m_o}{m_f}\right) = gI_{sp} \ln(R) \quad (4.5)$$

Where,

- m_o denotes initial total vehicle mass, including propellant (kg)
- m_p denotes the mass of the propellant consumed (kg)
- m_f denotes final total vehicle mass ($m_o - m_p$) (kg)
- R denotes the mass ratio of m_o/m_f

4.3 Thrusters

Spacecraft propulsion systems generally may be broken into four main types. These include cold gas, solid, liquid (mono-propellant, bi-propellant, or dual-mode), and electric. Cold gas systems are of low performance and are rarely used. Solid propellant systems are commonly used for orbit insertion maneuvers but are ill-suited for providing orbit maintenance and attitude control functions. Thus, satellites equipped with a solid propulsion system must be augmented with a secondary system to perform these maneuvers. Liquid mono-propellant thrusters are well-suited for orbit maintenance and attitude control functions, but are ill-suited for providing the delta-v required for orbit insertion. Liquid bi-propellant systems are well-suited for all three functions (attitude control, orbit maintenance, and orbit insertion). However, they are more complex.

Dual-mode propulsion systems are integrated mono and bi-propellant systems. They use hydrazine (N_2H_4) as a fuel and nitrogen tetroxide (N_2O_4) as an oxidizer for the high-performance bipropellant thrusters, while using hydrazine as a monopropellant for the low-thrust catalytic thrusters. The hydrazine is fed to both mono and bi-propellant thrusters from a common fuel tank. Dual-mode propulsion provides high I_{sp} for large delta-v burns at high thrust while also providing precise, low-impulse burns for attitude control. [48] Dual-mode propulsion will be utilized for the MMRS spacecraft, making use of hydrazine and nitrogen tetroxide.

The MMRS spacecraft will make use of three types of thrusters; one for each mode of propulsion. These include a main thruster for orbital insertion (large), trajectory correction thrusters (medium), and attitude control thrusters (small). These are detailed as follows, with data from existing spacecraft provided in tables 4.1, 4.2, and 4.3.

4.3.1 Orbital Insertion Thrusters

The orbital insertion thrusters of a spacecraft are the largest of the thrusters equipped on a spacecraft in terms of physical size and thrust output. These thrusters are used to perform the orbit insertion burn when arriving at the target planet. Parameters for the MMRS orbital insertion thrusters are provided in table 4.1 below. Calculations related to the sizing of the orbital inserting thruster are provided in appendix A.7.

Table 4.1 – Orbital insertion thruster data for existing spacecraft and MMRS.

Spacecraft	Total nominal thrust (N)	Per-thruster nominal thrust (N)	Number of thrusters	Type
Mars Reconnaissance Orbiter [49]	1020	170	6	N ₂ H ₄ monopropellant
Mars Odyssey [50]	640	640	1	MMH propellant / N ₂ O ₄ oxidizer
Mars Global Surveyor [36]	596	596	1	MMH propellant / N ₂ O ₄ oxidizer
Mars MAVEN [37]	1020	170	6	N ₂ H ₄ monopropellant
Juno [51]	645	645	1	MMH propellant / N ₂ O ₄ oxidizer
Galileo [52]	400	400	1	MMH propellant / N ₂ O ₄ oxidizer
Cassini [53]	445	445	1	MMH propellant / N ₂ O ₄ oxidizer
MMRS	1020	170	6	MMH propellant / N ₂ O ₄ oxidizer

4.3.2 Trajectory Correction Thrusters

The trajectory correction thrusters (TCT) of a spacecraft are commonly identical to those used for attitude control. However, instead of firing in quick bursts to gently nudge a spacecraft to the desired orientation, TCTs fire in longer-duration continuous bursts to correct the trajectory of the spacecraft. Unlike attitude control thrusters, which may be placed in various locations around the spacecraft, TCTs are commonly found oriented along a single direction. [54] Parameters for the MMRS trajectory correction thrusters are provided in table 4.2 below.

Table 4.2 – Trajectory correction thruster data for existing spacecraft and MMRS.

Spacecraft	Per-thruster nominal thrust (N)	Number of thrusters	Type
Mars Reconnaissance Orbiter [49]	22	6	N ₂ H ₄ monopropellant
Mars Odyssey [50]	22.5	4	MMH propellant / N ₂ O ₄ oxidizer
Mars Global Surveyor [36]	4.45	12	MMH propellant / N ₂ O ₄ oxidizer
Mars MAVEN [37]	22	6	N ₂ H ₄ monopropellant
Galileo [52]	10	12	MMH propellant / N ₂ O ₄ oxidizer
New Horizons [55]	4.4	4	N ₂ H ₄ monopropellant
MMRS	22	6	N ₂ H ₄ monopropellant

4.3.3 Attitude Control Thrusters

The reaction control system (RCS) of a spacecraft, also referred to as the attitude control system (ACS), commonly uses thrusters and reaction control wheels to provide attitude control and, in some applications, propulsion. Spacecraft reaction control systems provide several functions, including attitude control, station keeping, maneuvering during spacecraft docking, and controlling spacecraft orientation. For the MMRS spacecraft, only attitude control thrusters will be considered. This is done to eliminate the need for a separate reaction control wheel, as the spacecraft will already possess the N₂H₄ propellant used in the orbital insertion and trajectory correction thrusters. Unlike orbital insertion thrusters, attitude control thrusters are commonly used for only minor corrections, firing for only fractions of a second at a time. [54] Parameters for the MMRS reaction control system are provided in table 4.3 below.

Table 4.3 – Attitude control thruster data for existing spacecraft and MMRS.

Spacecraft	Per-thruster nominal thrust (N)	Number of thrusters	Type
Mars Reconnaissance Orbiter [49]	1	8	N ₂ H ₄ monopropellant
Mars Odyssey [50]	1	4	MMH propellant / N ₂ O ₄ oxidizer
Mars MAVEN [37]	1	8	N ₂ H ₄ monopropellant
Juno [51]	4.45	12 (3 per module)	N ₂ H ₄ monopropellant
Cassini [53]	1	8	MMH propellant / N ₂ O ₄ oxidizer
New Horizons [56]	0.8	12	N ₂ H ₄ monopropellant
MMRS	4.45	12 (3 per module)	N ₂ H ₄ monopropellant

4.3.4 Commercial Off-The-Shelf Thrusters

Table 4.4 below provides the specifications for several off-the-shelf thruster units that are currently commercially available and which approximately meet the requirements of the MMRS. The Aerojet Rocketdyne R-42DM thruster was selected as the orbital insertion thruster, while the MOOG MONARC-22-6 and MONARC-5 were chosen as the trajectory correction and attitude control thrusters, respectively.

Table 4.4 – Commercial thruster candidate key specifications.

	R-42DM [57]	MONARC-22-6 [58]	MONARC-5 [58]
Thrust (N)	890	22	4.5
Isp (s)	327	230	226
Valve power (W)	45	30	18
Mass (kg)	7.3	0.72	0.49
Type	MMH propellant / N ₂ O ₄ oxidizer	N ₂ H ₄ monopropellant	N ₂ H ₄ monopropellant
Application	Orbital insertion	Trajectory correction	Attitude control

Using equation 4.5, the parameters of the R-42DM engine in table 4.4, and the excel calculator provided in appendix A.7, the quantity of fuel required to perform a Hohmann transfer from Earth to Mars using the orbital insertion thruster can be determined. Using a delta-v 6.84 km/s (which is derived in section 7.1.2), a spacecraft wet mass of 1615.9 kg, the acceleration of gravity of 9.81 m/s², and the R-42DM engine Isp of 327 seconds, a theoretical propellant mass of 1424.30 kg for the burn is required. Note, however, that this does not consider the use of the launch vehicle’s upper stage, which would, in practice, offload the fuel mass requirement from the MMRS to the launch vehicle.

Considering a delta-v budget of 3.19 km/s for only the orbit-insertion phase of the Hohmann transfer, this reduces the fuel consumption to 1018.12 kg. Given a total spacecraft propellant mass allocation of 1123.9 kg, this is theoretically acceptable. Note, however, that additional propellant mass is allocated to the spacecraft to operate all three thruster types over the operational life of the spacecraft. Thus, additional propellant may be required depending on the requirements of the mission parameters over the spacecraft’s operational life. This will be further addressed in section 4.5, chapter 7, and table 8.3 of this document.

4.4 Block Diagram

A block diagram of the propulsion subsystem is provided in figure 4.1 below. The input variables are specific impulse (Isp), initial total vehicle mass (Mo), and initial propellant mass (Mp). These variables flow into tank size, thrust (and thus the mass flow rate), and total spacecraft mass. The output vector is the delta-v produced by the propulsion system. The governing equations used for these calculations are provided in the section 4.2.

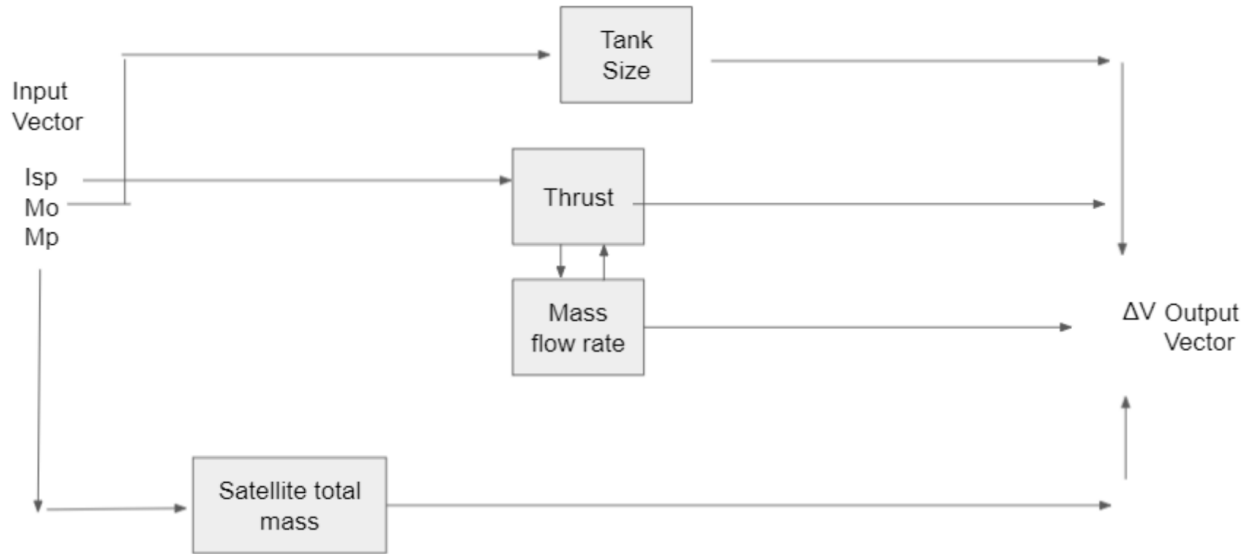


Figure 4.1 – High-level block diagram of propulsion subsystem.

4.5 Design of Experiments

A design of experiments was performed for the propulsion subsystem by leveraging the relationships of the delta-v equation provided in equation 4.5. Two values for specific impulse, initial total vehicle mass, and initial propellant mass were chosen, with a total of eight experiments performed. Varying these parameters generated a range of potential delta-v values. The highest delta-v observed occurred in experiment 3, in which specific impulse was 327 seconds, initial total mass (M_o) was 2180 kg, and initial propellant mass (M_p) was 2032 kg. The delta-v in this experiment was 8.629 km/s. These values are provided in table 4.5.

Table 4.5 – Design of experiments for the propulsion subsystem.

Experiment number	Factor			ΔV observation (m/s)
	Isp (s)	M_o (kg)	M_p (kg)	
1	327	3625	2032	$\eta_1 = 2638$
2	327	3625	1149	$\eta_2 = 1223$
3	327	2180	2032	$\eta_3 = 8629$
4	327	2180	1149	$\eta_4 = 2402$
5	230	3625	2032	$\eta_5 = 1855$
6	230	3625	1149	$\eta_6 = 860$
7	230	2180	2032	$\eta_7 = 6069$
8	230	2180	1149	$\eta_8 = 1690$

Using these experiments, and equations 4.6 and 4.7 below, the main effects for the propulsion subsystem were analyzed. Equations 4.6 and 4.7 yield an M_1 and M_2 value of 4.798 km/s and

1.544 km/s, respectively. Subtracting M2 from M1 produces a main effect of 3.254 km/s. This illustrates the main effect of the propellant mass on the delta-v budget.

$$M1 = \frac{\eta1 + \eta3 + \eta5 + \eta7}{4} \quad (4.6)$$

$$M2 = \frac{\eta2 + \eta4 + \eta6 + \eta8}{4} \quad (4.7)$$

Where,

- M denotes the effect (m/s)
- η denotes the observation (m/s)

Using equations 4.8 and 4.9, the interaction effects were analyzed. Equation 4.8 calculates the average propellant mass effect with the Isp of 327. Equation 4.9 calculates the average propellant mass effect with the Isp of 230. The average of equations 4.8 and 4.9 was then taken, resulting in a propellant mass-Isp interaction of 567 m/s.

$$\eta_{Isp1} = \frac{(\eta_4 - \eta_3) + (\eta_2 - \eta_1)}{2} \quad (4.8)$$

$$\eta_{Isp2} = \frac{(\eta_6 - \eta_5) + (\eta_8 - \eta_7)}{2} \quad (4.9)$$

4.6 Verification & Validation

Tables 4.6 and 4.7 present information regarding the verification and validation of the propulsion subsystem. The listed requirements are designated as either “shall” or “should” requirements, and are then ranked on a scale of 1-10 as to the degree to which the requirements are verifiable, achievable, logical, integral, and definitive. [27] A verification method is then given for that requirement, as is an overall ranking, which is an average of the 5 aforementioned factors.

Table 4.6 – Propulsion subsystem verification and validation (part 1).

Category	System ID	Requirement description	Justification
Propulsion	3.1	Orbital insertion thruster shall propel the satellite into station orbit	Required for optimal operation
	3.2	Trajectory correction thrusters shall fire in long-duration bursts to correct the trajectory of the spacecraft	Required for optimal operation
	3.3	Attitude control thrusters shall fire in quick bursts to gently nudge the spacecraft into the desired orientation	Required for optimal operation
	3.4	All thrusters shall operate until satellite end of life	Required for optimal operation
	3.5	Orbital insertion thruster should produce 1020 N of thrust	Orbital insertion
	3.6	Trajectory correction thrusters should provide 22 N of thrust each	Station keeping
	3.7	Attitude control thrusters should provide 4.45 N of thrust each	Attitude control
	3.8	Propellant tanks shall hold 1123.9 kg of propellant	Mission duration and scope

Table 4.7 – Propulsion subsystem verification and validation (part 2).

Category	System ID	Shall / Should	Verifiable (1-10)	Achievable (1-10)	Logical (1-10)	Integral (1-10)	Definitive (1-10)	Verification method	Overall (1-10)
Propulsion	3.1	Shall	10	10	10	10	8	Analysis	9.6
	3.2	Shall	10	10	10	10	8	Analysis	9.6
	3.3	Shall	10	10	10	10	8	Analysis	9.6
	3.4	Shall	10	10	10	8	8	Analysis	9.2
	3.5	Should	10	10	8	10	10	Static testing	9.6
	3.6	Should	10	10	8	10	8	Static testing	9.2
	3.7	Should	10	10	8	10	10	Static testing	9.6
	3.8	Shall	10	10	8	8	8	Testing	8.8

4.7 Test Plan

To test the propulsion subsystem, a facility with a test stand and vacuum chamber will be required. The thermal vacuum chamber V-20 located at Marshall Space Flight Center would be acceptable for this. This test facility complex is capable of mimicking high vacuum and extreme temperature ranges. [59] Testing may also be performed at the sub-scale, with testing of the injectors, thrusters, gas generators, turbopumps, ignitors, and other necessary components.

4.8 Risk Assessment

A risk assessment was performed for the propulsion subsystem, which is shown in table 4.8. The rubrics used in determining these risk levels are provided in appendix C.1. The risks associated with the propulsion system include nozzle ablation, excessive burn duration, and leaks in the propellant lines. Excessive burn duration of the orbital insertion thruster could cause the spacecraft to enter into the incorrect orbit, while misfiring of the trajectory correction and attitude control thrusters could have similarly undesirable results. Leaks in the propellant lines would additionally lead to fuel waste, which would endanger the longevity of the spacecraft. As the propulsion system has heritage, these risks are considered minor.

Table 4.8 – Propulsion subsystem risk assessment.

Level	Risk	Mitigation
C,1	Nozzle ablation	Testing
A,1	Excessive burn duration	Testing
C,1	Propellant leaks	Testing

5.0 Thermal Subsystem

5.1 Subsystem Overview

The thermal control system (TCS) of a spacecraft is used to maintain the temperature of all spacecraft subsystems and components within each of their respective high and low temperature limits for each phase of the space mission. These limits can be divided into operational limits and survival limits. Operational limits denote temperature limits of components while operating. Exceeding these limits can cause off-nominal performance. Survival limits denote temperature limits that components must remain at during all times, even when unpowered. Exceeding these limits can cause permanent component damage. Large temperature gradients across the spacecraft must also be considered to prevent structural deformation. [60] Typical operational and survival temperature limit ranges are provided in table 5.1.

Table 5.1 – Typical operational and survival temperature limit ranges. [60]

Component	Typical temperature ranges (°C)	
	Operational	Survival
Batteries	0 to 15	-10 to 25
Antennas	-100 to 100	-120 to 120
Antenna gimbals	-40 to 80	-50 to 90
Solar panels	-150 to 110	-200 to 130
IMU	0 to 40	-10 to 50
N ₂ H ₄ tanks and lines	15 to 40	5 to 50

Methods of thermal control can be categorized as either passive or active. Passive thermal control denotes the use of coatings, surface finishes, and materials. Active thermal control denotes temperature maintenance through electric heaters, coolers, or other more-complex active means.

The design of the thermal control system for a spacecraft consists of the following seven main steps. These are discussed in detail in subsequent sections. [60]

1. Identify thermal requirements and constraints
2. Determine the thermal environment
3. Identify thermal challenges or problem areas
4. Identify applicable thermal control techniques
5. Determine radiator and heater requirements
6. Estimate thermal control system mass and power
7. Document and iterate

In identifying requirements, the temperature ranges of components are of particular interest. Determining the thermal environment involves characterizing the heat inputs experienced by the

spacecraft, most notably from the sun. The orbit, maximum and minimum distance from the sun, as well as spacecraft size and shape are important considerations. In identifying thermal challenge areas, the thermal requirements of components are compared with actual heat sources and equipment placement to identify locations where temperature may exceed the accepted limits. Components that generate large amounts of heat, require cryogenic temperatures, or have narrow temperature ranges are of particular concern. Identifying thermal control techniques involves determining whether the use of coatings/paints or insulating blankets is prudent, in addition to considering component placement and the types of active cooling or heating systems to be used. Determining radiator and heater requirements involves identifying the worst-case hot and cold conditions. Radiator size and heater power are of particular concern, as are degradation of thermal surfaces over spacecraft life and time out of the sun. [60]

5.1.1 Spacecraft Thermal Environment

Once in space, the significant sources of environmental heating for a spacecraft include direct and reflected sunlight, and infrared radiation emitted from the atmosphere of the planet about which the spacecraft is orbiting. Sunlight is a main source of environmental heating experienced by a spacecraft. The intensity of sunlight is known as the solar constant. The solar constant at Earth is 1367 W/m², 590 W/m² at Mars, and 53.48 W/m² at Jupiter, on average. Sunlight reflected off of a planetary body is known as albedo. All sunlight not reflected as albedo is absorbed by the planetary body and then re-emitted as IR energy. For spacecraft in interplanetary space, sunlight is the only source of environmental heating. The infrared and albedo environments the spacecraft will encounter at its destination planet can vary. Several notable planets are provided in table 5.2.

Table 5.2 – Average planetary infrared and albedo emissions and solar constant. [60]

Planet	Average albedo	Average IR (W/m ²)	Average solar constant (W/m ²)
Earth	0.37	231	1361
Mars	0.29	141	590
Jupiter	0.34	13.5	53

Thermal control of a spacecraft is achieved by balancing the heat emitted from the spacecraft as infrared radiation against the sum of the heat dissipated by internal components and the heat absorbed from the environment.

5.2 Thermal Control Components

5.2.1 Surface Finishes

Wavelength-dependent coatings made from white-colored paints, quartz mirrors, or silver or aluminum-backed teflon may be used to reflect and emit solar energy. Black paint coatings are commonly used in the interior of the spacecraft if energy exchange between components or compartments is desired. Such coatings have heritage and are commercially available from a

variety of manufacturers. When considering coatings, the surface properties of IR emissivity, ϵ , and solar absorptivity, α , are of particular interest. Emissivity denotes the effectiveness of a surface at emitting thermal radiation. Emissivity ranges from 0 to 1, with 0 denoting a perfect reflector (i.e., polished silver) and 1 denoting a perfect emitter (i.e., black soot). Note that a theoretical perfect black body emits thermal radiation at 448 W/m^2 at 298.15 K. These coatings may, however, degrade while in orbit due to charged particles and radiation, which increases solar absorptivity. Thus, spacecraft radiators must be oversized to account for this increase in running temperature that occurs over the operational life of the spacecraft. Table 5.3 details surface finish properties for the MMRS.

Table 5.3 – Surface finishes and properties. [60]

Surface finish	α (BOL)	ϵ
Optical solar reflectors: 5 mil aluminized teflon	0.10 to 0.16	0.78
White paint: Z93	0.17 to 0.20	0.92
Black paint: 3M Black Velvet	0.97	0.84
Aluminized Kapton: 2 mil	0.41	0.75
Metallic: Anodized aluminum	0.25 to 0.86	0.04 to 0.88

5.2.2 Insulation

Multilayer insulation (MLI) blankets are used to prevent excessive heating or excessive heat loss on a spacecraft. They cover large portions of the spacecraft, including propellant tanks and propellant lines, with cutouts provided for thermal radiators. MLI is composed of multiple layers of low-emission, low-conductivity films commonly formed from $\frac{1}{4}$ inch mylar or Kapton sheets with an aluminum finish on one side. 25 insulative layers are common per blanket. The effective emittance, ϵ^* , of MLI blankets for medium-sized area applications is between 0.015 and 0.030, with lower ϵ^* being preferred. As application size increases, performance increases due to the relative decrease in losses due to edges, seams, and cable penetration locations. Aluminized Kapton is commonly used, operates over large temperature ranges between -260°C and 480°C , is capable of reflecting up to 97% of radiated heat, and is commercially available. [61]

Single-layer radiation blankets may be used in areas requiring less thermal protection and are cheaper to manufacture. In other areas, such as internal propellant lines, surface coatings may be used in place of MLI blankets, as they provide the same level of effectiveness for lower cost. To provide thermal protection under atmospheric conditions, foam or aerogel materials are commonly used, as MLI materials lose efficacy when exposed to atmosphere.

5.2.3 Radiators

Radiators are used to expel waste heat via IR radiation from a spacecraft and may include structural panels, flat-plate radiators, or deployable panels. Radiators are commonly given an IR emissivity of $\epsilon > 0.8$ and solar absorptivity of $\alpha < 0.2$, and thus have a high IR emissivity and low solar absorptivity. Note that emissivity is the ratio of energy radiated by a material's surface to the energy radiated by a perfect emitter under the same conditions. Absorptivity and emissivity are equal for an object in thermal equilibrium with its environment. The total heat expelled from a radiator surface is given by equation 5.1.

$$Q = \epsilon\sigma AT^4 = Q_{internal} + q_{external}A \quad (5.1)$$

Where,

- Q denotes the total heat leaving a radiator surface (W)
- ϵ denotes emissivity
- σ denotes the Stefan-Boltzmann constant ($5.67051 \times 10^{-8} \text{ W}/(\text{m}^2\text{K}^4)$)
- A denotes radiator surface area (m^2)
- T denotes absolute temperature (K)

Spacecraft radiators generally expel between $100 \text{ W}/\text{m}^2$ and $350 \text{ W}/\text{m}^2$ of internally-generated waste heat. Spacecraft weight allocated to radiators can range from being negligible (if existing structural panels are used for radiators) to $12 \text{ kg}/\text{m}^2$ (if a heavy deployable radiator and its support/deployment structure are considered). Sizing is determined by thermal analysis that considers operating temperature, worst-case waste heat, environmental heating, and radiative/conductive interactions with spacecraft surfaces. Leveraging equation 5.1, the Stefan-Boltzmann constant, an emissivity of 0.8, and a temperature of 393K (which corresponds to the maximum antenna survival temperature provided in table 5.1), a radiator area of 0.887 m^2 for the MMRS can be calculated. The full calculations are provided in appendix A.10. Deployable radiators are commercially available and may be adapted for a variety of sizes.

5.2.4 Heaters, Louvers, & Heat Pipes

Heaters are another form of thermal control used to warm components to their minimum operating temperature. The most commonly-used types of spacecraft heaters include patch and cartridge heaters. Patch heaters consist of a resistive element sandwiched between sheets of an insulative material such as Kapton. Patches may be custom-made or are commercially available in rectangular segments of varying dimension. A cartridge heater is used to heat high-temperature components, such as heating the catalyst beds on hydrazine thrusters to 100°C before they can fire. Heater systems also contain a control switch, fuse, and a thermostat or solid-state controller to enable activation at pre-set temperatures. A variety of thermostats are commercially available with differing set points (the temperature at which the thermostat activates) and dead bands (the temperature difference between which the thermostat switches on and off). Dead bands below 4°C are not recommended and may cause component failure. Typical satellites contain hundreds of thermostats. However, solid-state controllers are becoming

increasingly common due to their increased reliability, life expectancy, and precise temperature control (supporting dead bands of less than 0.1°C).

Louvers are used to modulate radiant heat transfer in a spacecraft and are often used when internal heat dissipation varies due to equipment duty cycles. They are often placed over radiators and open directly into space. In a fully-open state, a louver may allow for the rejection of six times as much heat as it would in a fully-closed state. The venetian-blind-type louver assembly is the most commonly-used and consist of blades, actuators, sensing elements, and structural elements. Each blade is independently-controlled and actuated based on radiator temperature. Louvers are commercially available in a number of configurations from different manufacturers. Parameters of the Starsys louvers, which have been used on the Cassini and Voyager probes are provided in table 5.4 below for reference. [60]

Table 5.4 – Louver parameters.

Parameter	Value
Blade number	1 to 16
Open set points (°C)	-20 to 50
Open/close differential (°C)	14
Dimensions (cm)	8 to 43 x 22 to 40 x 6.4
Area (m ²)	0.02 to 0.2
Weight/area (kg/m ²)	5.2 to 11.6

Heat pipes are used to transport large amounts of heat between locations in a spacecraft without the use of electricity via capillary pumping. They are often used when a physical separation exists between a heat source and a heat sink. They can additionally be used to create isothermal surfaces or distribute heat from a localized area to a larger area. The most basic heat pipes consist of a working fluid (commonly ammonia for spacecraft applications), a wick structure, and an envelope. They are formed from axial grooves of rectangular or trapezoidal shape (though other geometries can be employed) extruded in the walls of aluminum tubing. Traditional heat pipes operate most-efficiently without the presence of gravity or acceleration. However, loop heat pipes and capillary pumped loops can operate effectively under the effects of gravity and acceleration with varying heat loads.

Common classifications of heat pipes include diode and variable-conductance. Diode heat pipes are used as a means of connecting a heat source to multiple radiator panel of opposite sides of the spacecraft. As such, one radiator panel will always be facing away from the sun and will be able to efficiently radiate heat. Variable-conductance heat pipes can be used to control the amount of active radiator area. These are attractive if electrical power on the spacecraft is limited. [60]

5.3 Requirements

When designing the thermal control system, the mission objectives and requirements must be defined in detail such that alternative architectures can be evaluated and compared. Key

performance requirements include the acceptable temperature ranges of individual components and the thermal interfaces between components. The operational and functional requirements of the thermal subsystem for the MMRS spacecraft are outlined below and are elaborated upon in section 5.7.

- Operational Requirements
 - TCS should maintain all components within the acceptable temperature ranges under all mission conditions until spacecraft end of life.
 - Thermal interfaces with each subsystem should be maintained.
- Functional Requirements
 - Thermal paint/coatings/blankets on transponders and antenna shall not block or interfere with RF transmission or receiving.
 - Antennas shall maintain operational temperature range of -100°C . to 100°C with the associated gimbal temperature operational range of -40°C to 80°C .
 - IMU shall maintain operational temperature range of 0°C to 40°C .
 - Heat transfer between propellant tank heating system and thruster heating system shall maintain temperature range of -20°C to 113°C .
 - N_2H_4 tanks and lines shall maintain an operational temperature range of 15°C to 40°C .
 - Thermal and battery interface temperature range shall be -20°C to 60°C . [62]
 - Thermal and structure interface temperature range shall be -50°C to 60°C .
 - Thermal and communications interface temperature range shall be -20°C to 50°C .
 - Heaters shall heat the catalyst beds on hydrazine thrusters to 100°C before firing.
 - Radiators should expel 350 W/m^2 of internally-generated waste heat. [60]
 - Total radiator area shall be 0.887 m^2 .

After the design requirements have been identified, the thermal design development process can be completed. This entails selecting enclosures that will serve as a thermal sink for the spacecraft and selecting the thermal designs for the internal and external spacecraft components. It will initially be assumed that a fully-passive TCS will be sufficient to meet the thermal requirements for the spacecraft. This is assumed as passive systems are far less complex to design, build, test, and maintain, and are far cheaper and lighter than active systems. Active systems will only be employed where absolutely necessary.

The standard approach to thermal control for conventional spacecraft involves insulating the spacecraft from the space environment with MLI blankets while also providing locations for radiators that have low solar absorptivity and high emittance. Components that emit large amounts of heat are mounted on the walls of the spacecraft to create a direct path to the exterior radiating surfaces. Heat pipes may be employed for particularly hot components to distribute their heat over a larger area such that the heat can be radiated outward at a reasonable temperature.

Beyond the initial preliminary design, a thermal analysis of the design must be completed that considers the thermal environments encountered during the mission. This involves creating two types of analytical models. The geometric math model is a mathematical model that represents

the physical surfaces of the spacecraft (or spacecraft components) and is used to determine the radiation coupling between each surface and the heating rates on each surface due to external sources (solar, IR, and planetary albedo). The thermal math model is analogous to an RC electrical network and provides a representation of thermal capacitance. These models may be run to predict worst-case temperature conditions that arise due to an array of factors (including surface properties and sun incidence angle). If strictly passive thermal control is found by these models to be inadequate, they are conducted again with components that are increasingly additive in nature until a satisfactory configuration is found. Estimates of subsystem weight and power for all components can then be determined. Note, however, that this is beyond the scope of this document.

5.4 Governing Equations

As described in previous sections, thermal control systems must be designed to consider the operational environment of the spacecraft under a variety of thermal conditions. For example, the total radiator area must be sufficient to accommodate the maximum power output of the spacecraft while the spacecraft is in the hottest operational environment such that the appropriate component temperature range is maintained. Likewise, heaters must sufficiently warm components while in their coldest operational environment. Variations in environment and power dissipation, as well as degradation, over the spacecraft life must be considered. Such factors illustrate the large number of thermal conditions that must be designed for when designing a TCS. As the MMRS spacecraft is designed for interplanetary missions, those conditions will be the focus of this document.

Solar flux can vary considerably for interplanetary missions as solar flux varies inversely with the square of the distance from the sun. For spacecraft performing flyby maneuvers in the inner solar system, the solar flux encountered can be significantly greater than in the outer solar system. For reference, the average solar constant is 1361 W/m^2 at Earth, 590 W/m^2 at Mars, and 53 W/m^2 at Jupiter. The maximum and minimum solar constants differ based on the 11-year solar cycle. However, the variation is on the order of 0.1%. Thus, for this analysis, the average value per planet will be assumed for both the worst-case hot and worst-case cold scenarios.

The heat balance on the spacecraft radiators is the primary factor when considering the design of the TCS. The total radiator area required to expel the maximum operational heat load during the hottest environmental conditions is the first value to be calculated. This relationship is shown in equation 5.1. Note that this considers that the temperature gradients and operational temperature ranges of components are respected. Additionally note that the energy balance is initially considered to be steady state, which entails that all of the heat sources of the spacecraft are equal to all of the heat lost to space.

The heat balance equation is provided in equation 5.2. Note that Q_{MLI} can be assumed negligible when considering the maximum hot scenario.

$$Q_{internal} + Q_{external} = Q_{radiator} + Q_{MLI} \quad (5.2)$$

Where,

- $Q_{external}$ denotes the environmental heat absorbed (W)
- $Q_{internal}$ denotes the internal power dissipation (W)
- $Q_{radiator}$ denotes the heat rejected from the radiator surfaces (W)
- Q_{MLI} denotes the heat lost from elsewhere on the spacecraft (W)

$$q_{external} = q_{solar} + q_{albedo} + q_{EarthIR} + q_{backload} \quad (5.3)$$

Where,

- $q_{external}$ denotes the environmental heat load on the radiator per unit area (W/m^2)
- q_{solar} denotes the absorbed solar heat load per unit area (W/m^2)
- q_{albedo} denotes the absorbed heat load per unit area (W/m^2)
- $q_{EarthIR}$ denotes the absorbed Earth IR load per unit area (W/m^2)
- $q_{backload}$ denotes the radiative heat load from external spacecraft surfaces (i.e. solar panels, antennas) that is absorbed on the radiator per unit area (W/m^2)

Equation 5.3 provides the environmental heat load on the radiator per unit area, taking into account solar, albedo, Earth IR, and backload effects. These terms are defined as follows. Note that F is a thermal geometry factor. To derive this value, the spacecraft is approximated as an amalgam of flat plates, with the F value of each plate calculated separately as a function of the spacecraft orbital parameters. Calculating $q_{backload}$ requires geometric modeling that is beyond the scope of this design.

$$q_{EarthIR} = \varepsilon I_{EIR} F_{EIR} \quad (5.4)$$

Where,

- I_{EIR} denotes the intensity of Earth IR (W)
- F_{EIR} denotes a thermal geometry factor dependent upon altitude and attitude

$$q_{albedo} = \alpha I_{solar} \rho_{albedo} F_{albedo} \quad (5.5)$$

Where,

- I_{solar} denotes the intensity of solar fluxes (W)
- ρ_{albedo} denotes the average planetary albedo about which spacecraft orbits
- F_{albedo} denotes a thermal geometry factor dependent upon altitude and attitude

An excel calculator utilizing these equations was used to calculate the relevant parameters for the design of the thermal control system. The relevant excel sheets are provided in appendix A.9 and A.10 of this document. Parameters for Mars were used in these calculations, though the same calculations could be applied to Earth, Jupiter, or any other planetary body by replacing the appropriate constants. Mars parameters are provided in table 5.2. The average Mars IR of 141

W/m² was used for the maximum and minimum IR emission. The average albedo of 0.29 and the average solar constant of 590 W/m² were considered. A total spacecraft surface area of 68.74 m² was considered and was derived from the excel calculator provided in appendix A.9. An altitude of 370 km was considered. The full list of inputs is provided in appendix A.9. For these inputs, the following notable parameters are highlighted below.

- Radiator area to accommodate spacecraft power dissipation: 0.323 m²
- Minimum temperature for given radiator area: 14.3°C
- Solar energy absorbed: 6083.5 W
- Albedo energy absorbed: 1572.7 W
- Maximum IR energy absorbed: 1731.7 W

5.5 Block Diagram

A block diagram of the thermal subsystem is provided in figure 5.1. The input variables are internal spacecraft heat (Q_{in}), environmental heat absorbed (Q_{ex}), and the Stefan-Boltzman constant (σ). The internal blocks of the diagram are radiator emittance (ϵ) and radiator temperature (T). The output vector is radiator area (A). Thus, using this block diagram and the governing equations associated with these variables, the size of the satellite’s radiators can be determined. The governing equations used for these calculations are provided in section 5.4.

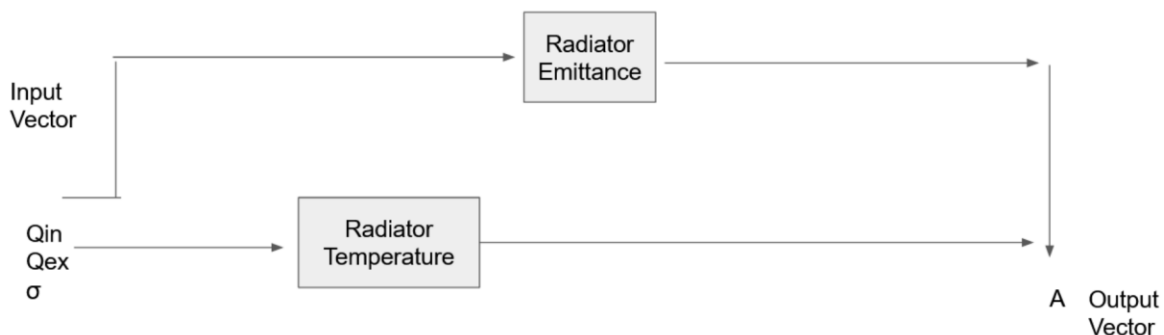


Figure 5.1 – High-level block diagram of thermal subsystem.

5.6 Design of Experiments

A design of experiments was performed for the thermal subsystem by leveraging the relationships of the total heat expelled by the radiator surface provided in equation 5.1. Two values for radiator emittance (ϵ), radiator temperature (T), and radiator area (A) were chosen, with a total of eight experiments performed. Varying these parameters generated a range of potential Q values. The highest Q observed occurred in experiment 8, in which radiator emittance was 0.88, radiator temperature was 373 K, and area was 1.0 m². The Q in this experiment was 965.9 W. These values are provided in table 5.5 below. Values of radiator emittance were chosen assuming anodized aluminum as the material, as described in table 5.3.

[60] Common values for radiator temperature were chosen based on existing systems. Using a radiator area of 0.887 m², as was calculated in appendix A.9, results in a Q value of 856.8 W. This Q value is in relative agreement with the calculated maximum power dissipation of 965.9 W, as described in appendix A.9, differing by 11.3%.

Table 5.5 – Design of experiments for the thermal subsystem.

Experiment number	Factor			
	ϵ	T (K)	A (m ²)	Q observation (W)
1	0.04	273	0.5	$\eta_1 = 6.23$
2	0.04	273	1.0	$\eta_2 = 12.6$
3	0.04	373	0.5	$\eta_3 = 22.0$
4	0.04	373	1.0	$\eta_4 = 43.9$
5	0.88	273	0.5	$\eta_5 = 138.6$
6	0.88	273	1.0	$\eta_6 = 277.2$
7	0.88	373	0.5	$\eta_7 = 483.0$
8	0.88	373	1.0	$\eta_8 = 965.9$

Using these experiments, and equations 5.6 and 5.7 below, the main effects for the thermal subsystem were analyzed. Equations 5.6 and 5.7 yield an M1 and M2 value of 162.5 W and 324.9 W, respectively. Subtracting M2 from M1 produces a main effect of 162.4 W. This illustrates the main effect of the radiator area on the heat budget.

$$M1 = \frac{\eta_1 + \eta_3 + \eta_5 + \eta_7}{4} \quad (5.6)$$

$$M2 = \frac{\eta_2 + \eta_4 + \eta_6 + \eta_8}{4} \quad (5.7)$$

Where,

- M denotes the effect (W)
- η denotes the observation (W)

Using equations 5.8 and 5.9, the interaction effects were analyzed. Equation 5.8 calculates the average radiator area effect with a radiator emittance of 0.04. This results in a value of 14.1. Equation 5.9 calculates the average radiator area effect with a radiator emittance of 0.88. This results in a value of 310.8. The average of equations 5.8 and 5.9 was then taken, resulting in an area-emittance interaction of 162.5.

$$\eta_{\epsilon 1} = \frac{(\eta_4 - \eta_3) + (\eta_2 - \eta_1)}{2} \quad (5.8)$$

$$\eta_{\varepsilon 2} = \frac{(\eta_6 - \eta_5) + (\eta_8 - \eta_7)}{2} \quad (5.9)$$

5.7 Verification & Validation

Tables 5.6 and 5.7 present information regarding the verification and validation of the thermal control subsystem. The listed requirements are designated as either “shall” or “should” requirements, and are then ranked on a scale of 1-10 as to the degree to which the requirements are verifiable, achievable, logical, integral, and definitive. [27] A verification method is then given for that requirement, as is an overall ranking, which is an average of the 5 aforementioned factors.

Table 5.6 – Thermal subsystem verification and validation (part 1).

Category	System ID	Requirement description	Justification
Thermal	4.1	TCS should maintain all components within the acceptable temperature range under all mission conditions until spacecraft end of life.	Required for optimal operation
	4.2	Thermal interfaces with each subsystem should be maintained.	Required for optimal operation
	4.3	Thermal paint/coatings/blankets on transponders and antenna shall not block or interfere with RF transmission or receiving.	Required for optimal operation
	4.4	Antennas shall maintain operational temperature range of -100°C. to 100°C with the associated gimbal temperature operational range of -40°C to 80°C.	Required for optimal operation
	4.5	IMU shall maintain operational temperature range of 0°C to 40°C.	Required for optimal operation
	4.6	Heat transfer between propellant tank heating system and thruster heating system shall maintain temperature range of -20°C to 113°C.	Required for optimal operation
	4.7	N ₂ H ₄ tanks and lines shall maintain an operational temperature range of 15°C to 40°C.	Required for optimal operation
	4.8	Thermal and battery interface temperature range shall be -20°C to 60°C. [62]	Required for optimal operation
	4.9	Thermal and structure interface temperature range shall be -50°C to 60°C.	Required for optimal operation
	4.10	Thermal and communications interface temperature range shall be -20°C to 50°C.	Required for optimal operation
	4.11	Heaters shall heat the catalyst beds on hydrazine thrusters to 100°C before firing.	Required for optimal operation

Category	System ID	Requirement description	Justification
Thermal	4.12	Radiators should expel 350 W/m ² of internally-generated waste heat. [60]	To accommodate spacecraft power dissipation.
	4.13	Total radiator area shall be 0.887 m ² .	To accommodate spacecraft power dissipation.

Table 5.7 – Thermal subsystem verification and validation (part 2).

Category	System ID	Shall / Should	Verifiable (1-10)	Achievable (1-10)	Logical (1-10)	Integral (1-10)	Definitive (1-10)	Verification method	Overall (1-10)
Thermal	4.1	Should	10	8	10	8	10	Analysis	9.2
	4.2	Should	10	9	10	8	10	Analysis	9.4
	4.3	Shall	10	9	9	8	9	Analysis	9
	4.4	Shall	10	10	9	8	8	Analysis	9
	4.5	Shall	10	10	9	8	8	Analysis	9
	4.6	Shall	10	10	9	8	8	Analysis	9
	4.7	Shall	10	10	9	8	8	Analysis	9
	4.8	Shall	10	10	9	8	8	Analysis	9
	4.9	Shall	10	10	9	8	8	Analysis	9
	4.10	Shall	10	10	9	8	8	Analysis	9
	4.11	Shall	10	10	9	8	8	Analysis	9
	4.12	Should	10	10	9	8	10	Analysis	9.4
	4.13	Shall	10	10	9	9	10	9	Analysis

5.8 Test Plan

To test the thermal control subsystem, individual spacecraft components must be subjected to thermal cycling tests to replicate the large temperature swings of the space environment. The thermal vacuum chamber V-20 located at Marshall Space Flight Center would be acceptable for this as the test facility complex is capable of mimicking high vacuum and extreme temperature ranges for the fully-integrated satellite. [63] Factors to consider for thermal testing include the testing of thermocouples placed on propellant tanks and components and the cycling of electrical heaters to simulate flight conditions.

5.9 Risk Assessment

A risk assessment was performed for the thermal control subsystem, which is shown in table 5.8 below. The rubrics used in determining these risk levels are provided in appendix C.1. The risks associated with the thermal subsystem have a low likelihood of occurring given the heritage associated with the components. Risks include thermal coating ablation, thermal blanket

tearing, excessive heat transfer between components of the spacecraft, failure of a heater to maintain the proper component operating temperature range, and radiator failure. The failure of a heater or radiator would cause a significant degradation in the technical performance of the spacecraft as it could render key systems inoperable. Risks can be mitigated with testing and redundant design. As the propulsion system has heritage, these risks are considered minor.

Table 5.8 – Propulsion subsystem risk assessment.

Level	Risk	Mitigation
B,3	Thermal coating ablation	Testing
C,1	MLI blanket puncture	Testing
C,1	Excessive heat transfer	Testing
D,1	Heater failure	Redundant design
D,1	Radiator failure	Redundant design
D,1	Louver failure	Testing
D,1	Heat pipe failure	Testing

6.0 Structures and Mechanisms Subsystem

6.1 Subsystem Overview

The design of the structures and mechanisms subsystem must meet all strength, stiffness, and frequency requirements of the spacecraft and that of the interface between the spacecraft and launch vehicle. The primary structure must support all major loads while the secondary structure supports non-structural loads, including wire bundles, propellant lines, and brackets for smaller components. The structure must also be able to withstand the loads and vibrations incurred during launch. The design of the structures and mechanisms subsystem for a spacecraft consists of the following main steps. These are discussed in detail in subsequent sections. [64]

1. Identify requirements with respect to the mission, launch vehicle, and operating environment.
2. Developing packaging configurations with respect to the subsystem requirements, envelope, accessibility, and producibility.
3. Consider design options, including construction methods and materials.
4. Develop test and analysis criteria for each structural member, assessing for likely failure modes, weight saving, and reinforcements.
5. Size structural members and iterate.

6.1.1 General Structural Requirements

The main body structure of the spacecraft typically accounts for between 10% to 20% of the total spacecraft dry mass, with the mass of secondary structures allocated to their respective subsystems. The estimated spacecraft structure mass is increased by 10% above the calculated value to account for fasteners and fittings. Additionally, an extra 25% margin is budgeted to allow for design changes and underestimating. However, this 25% value can be decreased as the subsystem design matures.

The launch vehicle, in part, dictates structural requirements in the form of the weight, rigidity, and strength of the spacecraft. The launch vehicle structure possesses natural frequencies that may respond to forces induced internally by engine oscillations or externally from aerodynamic effects. The natural frequencies for a given launch vehicle are a known quantity and are provided by the launch provider, along with the associated axial or torsional modes. The launch vehicle will be further discussed in subsequent sections. These natural frequencies and modes are avoided when designing the spacecraft structure, with typical resonance sources including oscillations in the propulsion system and aerodynamic buffeting on ascent. The firing of engines during staging produces steady state accelerations while firing, and produces transient accelerations at burnout and ignition oriented along the axis of the spacecraft. Wind gusts and maneuvers can produce lateral transient accelerations. Such accelerations are known as load factors. Pyrotechnic shock, another source of load, results from impulses of booster separation, payload fairing separation, and the release of solar panels or other deployable equipment.

However, such shock loads attenuate quickly and rarely are a source of damage to the structure. [64]

6.1.2 Design Options & Criteria

In designing a spacecraft structure, trade studies must be performed to determine the materials, type of structure, and method of construction. In terms of materials, aluminum alloy is among the most commonly-used metals for spacecraft structures. This is, in part, due to the lightweight, easy to machine, low cost, and low-density nature common among most aluminum alloys. However, steel, magnesium, titanium, and beryllium alloys, in addition to composite materials, may also be used depending on the material properties required. An extensive description of material properties for aerospace vehicle structures can be found in MIL-HDBK-5. [65]

Structure types include skin panel assemblies, trusses, ring frames, fittings, and brackets. Structural elements may be attached with adhesive bonds, welds, or fasteners, with fasteners and fittings contributing significantly to the weight of the structure. Local stress concentrations around fasteners may result in structural failures. Welding is another option, though the heat produced can dramatically decrease material strength immediately surrounding the weld.

Random variables can affect the adequacy of spacecraft structures. Such variables include those caused by an unpredictable environment (i.e., acoustics, engine vibration, air turbulence, and wind gusts during launch) or process variation during manufacturing. Due to this uncertainty, structural viability must be approximated and design criteria must be established to ensure acceptable reliability. Such design criteria include the following.

- Utilize a design-allowable strength for the selected material that all specimens must meet.
- Derive a design limit load equivalent to the average load value plus 3 standard deviations.
- Multiply the design limit load by a factor of safety. Note that this value does not exceed the allowable strength.
- Test the structure.

The following test options, as outlined in Space Mission Analysis and Design and described in table 6.1 below, may be performed. [64] Note that neglecting structural testing is extremely risky and could lead to structural failure even with the associated factors of safety.

Table 6.1 – Typical unmanned spacecraft test options. [64]

Testing option	Design factors of safety	
	Yield	Ultimate
Ultimate test of dedicated qualification article	1.0	1.25
Proof test of all flight structures	1.1	1.25
Proof test of one flight unit of a fleet	1.25	1.4
No structural test	1.6	2.0

Fatigue analysis must also be performed to ensure that the structure will withstand multiple loading cycles. Such loading cycles may be induced by ground testing, ground transportation, and the launch environment. Fatigue analysis is performed by comparing the number of cycles at the limit stress with the average number of cycles at which failure occurs.

6.1.3 Sizing & Analysis of Structural Members

In sizing the structural members of the spacecraft, stiffness, strength, and weight are the three primary initial considerations, with later iterations additionally considering fatigue life and cost. The mode shapes and natural frequencies of the spacecraft depend on the stiffness and mass properties of the structure. The primary natural frequencies of a stowed spacecraft can be approximated by representing the spacecraft as a beam, which simulates the mass properties and core stiffness. Finite element modeling can then be performed. Such a model can also be used to predict the distribution of internal loads, which reflect strength. To have sufficient strength, structural members must not rupture, collapse, yield, or deform under tensile or compressive loads. Design ultimate loads are used to assess rupture and collapse.

There are two approaches to begin the process of sizing the spacecraft structure. In one approach, the structure can be sized to meet load requirements and the resulting natural frequencies can be checked. In the second approach, a frequency requirement could be defined, the structure could then be sized, and the strength of the structure could then be checked. As the frequency requirements are dictated by the launch vehicle, which is known, this second approach will be utilized for the MMRS. The size and mass of the structure are driven by either strength or stiffness requirements. In general, short and heavy spacecraft are driven by strength requirements, while long and light spacecraft are driven by stiffness requirements.

6.2 Requirements

When designing the spacecraft structure, the mission objectives and requirements must be defined in detail such that alternative architectures can be evaluated and compared. Key performance requirements include structural rigidity, strength, and natural frequency. The operational and functional requirements of the structure of the MMRS spacecraft are outlined below and are elaborated upon in section 6.9.

- Operational Requirements
 - Structure shall support the weight of the entire spacecraft bus and payload during each mission phase
 - Structure shall support mounting of all the subsystem modules, decks, and equipment
 - MMRS spacecraft shall withstand launch dynamics
 - Structure shall possess sufficient rigidity to keep the MMRS from violating the dynamic envelope of the launch vehicle fairing
- Functional Requirements
 - Structure should be able to support a weight of approximately 1616 kg

- The spacecraft shall withstand 10 g axial and 5 g lateral vibration loads during launch
- The first axial natural frequency of the MMRS shall be above 15 Hz
- The first lateral (bending) natural frequency shall be above 8 Hz
- A factor of safety of 1.25 (ultimate) and 1.10 (yield) should be heeded

6.3 Structural Design & Analysis

The MMRS spacecraft will be idealized as a cantilevered cylinder, with all spacecraft mass uniformly distributed throughout. This cylinder can be of monocoque construction, consisting of panels and shells without attached stiffening members. This approach is used when applied loads are distributed rather than concentrated. This cylinder could also be of semi-monocoque construction, consisting of added closely-spaced stiffening members to increase buckling strength. This cylinder could additionally be of skin-stringer construction, having longitudinal members (stringers) and lateral members (frames) to accept concentrated loads, and skin to spread those loads out and to transfer shear. [64] Monocoque and semi-monocoque construction will be investigated for the MMRS.

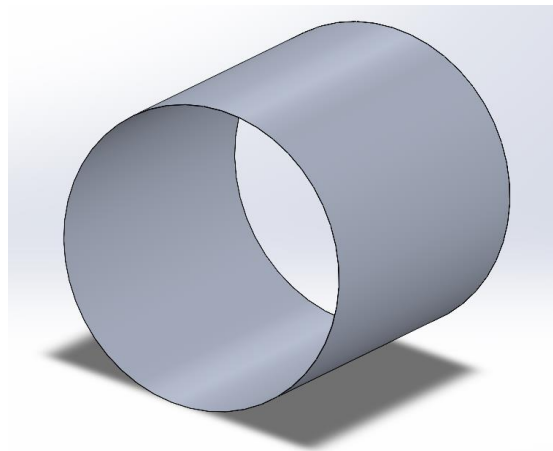


Figure 6.1 – Aluminum 7075 monocoque cylindrical shell model.

A monocoque structure for the MMRS will be investigated first. Assuming a cylindrical shape of length 2.93 m and radius 1.32 m, a spacecraft mass of 1615.9 kg, and axial and lateral acceleration load factors of 6.0 G's and 2.0 G's, respectively, monocoque structure parameters can be calculated. These axial and lateral vibration values are derived from the design load factors of the United Launch Alliance (ULA) Atlas V-401 launch vehicle. [66] Several launch vehicles and their respective masses to orbit are elaborated upon in table 6.2. Values specific to the ULA Atlas V-401 are provided in table 6.3 and are further elaborated upon in appendix A.14. Values for the cylindrical length and radius are derived from the overall spacecraft sizing, as calculated in appendix A.11. These values are shown in detail in appendix A.14. Considering this monocoque construction, the parameters for the MMRS main structure, as calculated in appendix A.14, are provided in table 6.4. A three-dimensional computer aided design (CAD) model of the

idealized monocoque uniform cylindrical shell was modeled using SolidWorks. This model is shown in figure 6.1 above.

Table 6.2 – Launch vehicles and payload to orbit masses for existing spacecraft and MMRS.

Spacecraft	Launch vehicle	Payload to LEO (kg)	Payload to GTO (kg)	Total S/C launch mass (kg)
Mars Reconnaissance Orbiter [66]	Atlas V - 401	9797	4750	2180 [49]
Mars Odyssey [67]	Delta II - 7925	6097	2171	758 [50]
Mars Global Surveyor [67]	Delta II - 7925	6097	2171	1031
Mars MAVEN [66]	Atlas V - 401	9797	4750	2454 [37]
Juno [66]	Atlas V - 551	18814	8900	3625 [51]
Galileo [68]	Space Shuttle	27500	10890	2223 [52]
Cassini [69]	Titan IV – 401B	17700	6350	5712 [53]
New Horizons [66]	Atlas V - 551	18814	8900	478 [55]
MMRS	Atlas V - 401	9797	4750	1615.9

Table 6.3 – Atlas V launch vehicle parameters (from appendix A.14). [66]

Payload dimensions	Payload compartment diameter	4.6 m
	Payload compartment cylinder length	5.0 m
	Payload compartment cone length	5.3 m
Accelerations	Axial acceleration	6.0 g's
	Lateral acceleration	2.0 g's
Frequencies	Fundamental axial frequency	15.0 Hz
	Fundamental lateral frequency	8.0 Hz
Cost	Estimated launch price	\$83,000,000

Note that in tables 6.4 and 6.5 below, the cylinder parameters of skin thickness, cross-sectional area, and area moment of inertia are adjusted such that the axial and lateral natural frequencies are within the acceptable range of those generated by the Atlas V during launch conditions. The axial and lateral natural frequencies are 15.0 Hz and 8.0 Hz, respectively. Converted to radians per second, this is 94.9 r/s and 67.8 r/s, respectively. The thickness of the cylinder can be calculated using equations 6.7 and 6.8 below. However, in order to meet the stiffness requirement dictated by the axial and lateral natural frequencies, the thickness was increased to 1.156e-1 cm. This is illustrated in table 6.4.

Table 6.5 below provides structure parameters assuming a semi-monocoque construction. Note that the parameters omitted from table 6.5 are identical to those provided in table 6.4. The material properties provided in table 6.4 assume aluminum 7075. As per this analysis, monocoque construction was selected for the MMRS.

Table 6.4 – Select parameters for MMRS main structure of monocoque construction (from appendix A.12).

Material properties (7075 Aluminum)	Young's modulus	7.100e10 N/m ²
	Material density	2.800e3 kg/m ³
	Ultimate tensile stress	5.240e8 N/m ²
	Yield tensile stress	4.480e8 N/m ²
	Factor of safety (ultimate)	1.25
	Factor of safety (yield)	1.10
Cylinder parameters	Length	2.93 m
	Radius	1.32 m
	Spacecraft mass	1615.9 kg
	Skin thickness	1.156e-1 cm
	Cross sectional area	9.621e1 cm ²
	Area moment of inertia	8.434e5 cm ⁴
Structure components	Skin mass	79.0 kg
	Fastener & fitting mass	7.9 kg
	Total mass	86.9 kg
Rigidity	Axial deflection	0.020 cm
	Lateral deflection	0.017 cm

Table 6.5 – Select parameters for MMRS main structure of semi-monocoque construction (from appendix A.13).

Cylinder parameters	Skin thickness	1.336e-1 cm
	Cross sectional area	1.112e2 cm ²
	Area moment of inertia	9.745e5 cm ⁴
Structure components	Number of stringers	4
	Total cross-sectional area per stringer	27.8 cm ²
	Area moment of inertia of all stringers	5.864e3 cm ⁴
	Skin mass	91.3 kg
	Stringer mass	0.5 kg
	Ring frames and fasteners mass	22.8 kg

The Atlas V – 401 launch vehicle configuration possesses a 4-meter diameter payload fairing. This will easily accommodate the 2.64-meter diameter idealized cylindrical envelope of the MMRS. However, a 5-meter 500-series configuration for the Atlas V is also available. Payload fairings may also be custom-made up to 3.2-meters, allowing for the 2.93-meter length of the MMRS to be accommodated. [66]

As shown in table 6.4, the total main structure mass is 86.9 kg. The total spacecraft dry mass is 492 kg, as shown in table 6.7. Taking the product of these values, the main structure mass is 17.67% of the total dry spacecraft mass. This falls between the standard 10% to 20% range, as was described in subsection 6.1.1.

6.4 Governing Equations

The natural frequencies induced by the launch vehicles by axial and lateral loads are of particular interest. Axial loads experienced during launch are driven by vehicle thrust and drag profiles. Lateral loads are driven primarily by atmospheric disturbances, engine gimbal maneuvers, engine shutdown, and other limited-duration events. Using equation 6.1 (and by association equation 6.2), the minimum cylinder thickness can be determined for a given axial and lateral natural frequency.

$$f_{nat} = \frac{1}{2\pi} \sqrt{\frac{k}{m_B}} \quad (6.1)$$

Where,

- f_{nat} denotes the natural frequency of the equivalent beam representing the spacecraft (Hz)
- k denotes the spring constant, representing stiffness (N/m)
- m_B denotes the uniformly-distributed beam mass (kg)

$$k = \frac{m_B g}{\delta} \quad (6.2)$$

Where,

- δ denotes deflection (m)

Note that the equation used to estimate the representative beam deflections for axial, lateral, or bending loads vary by situation. For the purposes of representing the MMRS in the launch vehicle at launch, the MMRS can best be represented as a uniform distributed load fixed at one end. The axial natural frequencies and deflections are thus represented by equations 6.3 and 6.4, respectively. The lateral natural frequencies and deflections are represented by equations 6.5 and 6.6, respectively.

$$f_{nat,axial} = 0.250 \sqrt{\frac{AE}{m_B L}} \quad (6.3)$$

Where,

- $f_{nat,axial}$ denotes axial natural frequency (Hz)
- A denotes cross-sectional area of the beam (m^2)
- E denotes Young's modulus (N/m^2)
- L denotes beam length (m)

$$\delta_{axial} = 0.5 \left(\frac{m_B L}{AE} \right) ng \quad (6.4)$$

Where,

- δ_{axial} denotes axial deflection (m)
- n denotes the load factor

$$f_{nat,lateral} = 0.560 \sqrt{\frac{EI}{m_B L^3}} \quad (6.5)$$

Where,

- $f_{nat,lateral}$ denotes lateral natural frequency (Hz)
- I denotes the area moment of inertia of the cross section of the beam (m⁴)

$$\delta_{lateral} = 0.125 \left(\frac{m_B L^3}{EI} \right) ng \quad (6.6)$$

Where,

- $\delta_{lateral}$ denotes lateral deflection (m)

To calculate the thickness of the cylinder, equations 6.7 and 6.8 were utilized using the values provided in table 6.6. Note that the MMRS total mass of 1615.9 kg was converted to Newtons. Additionally note that the limit loads (P_{axial} and $P_{lateral}$ used in equation 6.8) represent the mass (in Newtons) multiplied by the load factor. Note that $P_{bending}$ is the limit load also multiplied by the moment arm. The axial load factor assumes a steady state factor of 2.5 and a transient factor of 4.0 for a total load factor of 6.5. A lateral load factor of 3.0 was considered. The distance considers the length of the moment arm, which is considered to be the middle of the cylinder. The limit load is the product of the weight and the load factor. These values are provided in table 6.6.

$$F_{tu} = \frac{P_{eq}}{2\pi R t} \quad (6.7)$$

Where,

- F_{tu} denotes ultimate tensile strength (N/m²)
- P_{eq} denotes the equivalent axial limit load (N)
- R denotes cylinder radius (m)
- t denotes cylinder thickness (m)

The equivalent axial load P_{eq} is solved by adding P_{axial} (the axial limit load) to the quotient of 2 times the bending moment limit load divided by the cylinder radius. This relationship is illustrated in equation 6.8. The calculated value for P_{eq} is 208,533, as shown in table 6.6.

Considering a factor of safety of 1.25, this equivalent axial load is increased to 260,667 N. This value (which includes a 1.25 FOS) is used as the P_{eq} variable in the design of experiments in section 6.5. A FOS of 1.5 is additionally explored in the design of experiments.

$$P_{eq} = P_{axial} + \frac{2M}{R} \quad (6.8)$$

Where,

- P_{axial} denotes the axial limit load (N)
- M denotes the bending moment limit load (Nm)

Equations 6.7 and 6.8 yield a skin thickness of 6.000e-3 cm. This is in moderate agreement with the excel-calculated value of 4.736e-3 cm. However, in order to meet the rigidity requirement imposed by the 15.0 Hz axial and 8.0 Hz lateral natural frequencies, this thickness was scaled up to 1.156e-1 cm. Note that skin thickness and other calculated cylinder parameters are provided in tables 6.4 and 6.5.

Table 6.6 – Cylinder applied loads.

Type	Weight (N)	Distance (m)	Load factor	Limit load (P)	Equivalent axial load (P_{eq})
Axial	15847	N/A	6.5	103,006 N	208,533 N
Lateral	15847	N/A	3.0	47,541 N	N/A
Bending moment	15847	1.465	3.0	69,648 Nm	N/A

6.5 Design of Experiments

A design of experiments was performed for the structures and mechanisms subsystem by leveraging the relationships of cylinder skin thickness developed in equations 6.7 and 6.8. The equivalent axial limit load (P_{eq}) is held constant at the calculated value of 208,533 N. However, two factors of safeties are investigated; a FOS of 1.25 (yielding a limit load of 260,667 N) and a FOS of 1.5 (yielding a limit load of 312,800). Two candidate metals commonly used in spacecraft structures were identified. These include 7075 aluminum (with a UTS of 5.24E+08 N/m²) [64] and 304 stainless steel (with a UTS of 5.05E+08 N/m²) [70]. Two cylindrical radii were investigated. These include 1.32 m and 1.82 m. The results of these experiments are shown in table 6.7 below. While thinner thickness may be preferred for weight savings, ultimately experiment 1 was selected as the baseline value due to smaller radius, smaller factor of safety, and the material choice of 7075 aluminum. However, in order to meet the rigidity requirement imposed by the 15.0 Hz axial and 8.0 Hz lateral natural frequencies, this thickness was scaled up to 1.156e-1 cm, as described previously.

Table 6.7 – Design of experiments for the structure subsystem.

Experiment number	Factor			
	P _{eq} (N)	F _{tu} (N/m ²)	R (m)	t observation (m)
1	260667	5.24E+08	1.32	η ₁ = 6.00E-05
2	260667	5.24E+08	1.82	η ₂ = 4.35E-05
3	260667	5.05E+08	1.32	η ₃ = 6.22E-05
4	260667	5.05E+08	1.82	η ₄ = 4.51E-05
5	312800	5.24E+08	1.32	η ₅ = 7.20E-05
6	312800	5.24E+08	1.82	η ₆ = 5.22E-05
7	312800	5.05E+08	1.32	η ₇ = 7.47E-05
8	312800	5.05E+08	1.82	η ₈ = 5.42E-05

Using these experiments, and equations 6.9 and 6.10 below, the main effects for the structure subsystem were analyzed. Equations 6.9 and 6.10 yield an M1 and M2 value of 6.72E-05 m and 4.88E-05 m, respectively. Subtracting M2 from M1 produces a main effect of 1.85E-05 m. This illustrates the main effect of the radius size on the cylinder skin thickness.

$$M1 = \frac{\eta_1 + \eta_3 + \eta_5 + \eta_7}{4} \quad (6.9)$$

$$M2 = \frac{\eta_2 + \eta_4 + \eta_6 + \eta_8}{4} \quad (6.10)$$

Where,

- M denotes the effect (m)
- η denotes the observation (m)

Using equations 6.11 and 6.12, the interaction effects were analyzed. Equation 6.11 calculates the effect of cylinder skin thickness with a FOS of 1.25. This results in a value of 1.68E-05 m. Equation 6.12 calculates the effect of cylinder skin thickness with a FOS of 1.50. This results in a value of 2.01E-05. The average of equations 6.11 and 6.12 was then taken, resulting in an FOS-thickness interaction of 1.85E-05 m.

$$\eta_{Peq1} = \frac{(\eta_4 - \eta_3) + (\eta_2 - \eta_1)}{2} \quad (6.11)$$

$$\eta_{Peq2} = \frac{(\eta_6 - \eta_5) + (\eta_8 - \eta_7)}{2} \quad (6.12)$$

6.6 Spacecraft Mass, Dimensions, & Packaging

6.6.1 Spacecraft Mass & Sizing

The masses of the individual subsystems allocated to the MMRS are provided in table 6.8 below. The baseline values were derived from the excel calculator, which is based on a computed mass distribution percentage of existing in-family spacecraft. [64] These values were further-refined by breaking each subsystem into their main elements (where possible) and identifying masses of those elements from historical data. A margin of 78.84 kg is considered as a more-detailed design of each subsystem down to the component level would be required. These values are further elaborated upon in appendix A.11.

Table 6.8 – Mass broken down by subsystem.

Subsystem	Mass (kg)
Payload	86.3
ACS	29.2
C&DH	15.1
Power	143.88
Propulsion	27.08
Structure	86.9
Thermal	12.4
Communication	12.3
Margin	78.84
Propellant	1123.9

The total dry, total launch, and total fuel masses of several in-family spacecraft were investigated and compared to the analogous values of the MMRS. These values are provided in table 6.9 below and are plotted in figure 6.2, yielding an R^2 value of 0.88, indicating a strong correlation. To calculate the mass values for the MMRS, the excel calculator was used (as indicated previously) and the individual subsystem masses were summed. The results of these calculators are provided in appendix A.11.

Table 6.9 – Launch and dry mass for existing spacecraft and MMRS.

Spacecraft	Total S/C launch mass (kg)	Dry mass (kg)	Fuel mass (kg)	Fuel mass % of total mass
Mars Reconnaissance Orbiter [49]	2180	1031	1149	52.71
Mars Odyssey [50]	758	376	382	50.40
Mars MAVEN [37]	2454	809	1645	67.03
Juno [51]	3625	1593	2032	56.06
Galileo [52]	2223	1880	343	15.43
Cassini [53]	5712	2523	3189	55.83

Spacecraft	Total S/C launch mass (kg)	Dry mass (kg)	Fuel mass (kg)	Fuel mass % of total mass
New Horizons [55]	478	401	77	16.11
MMRS	1615.9	492	1123.9	69.55

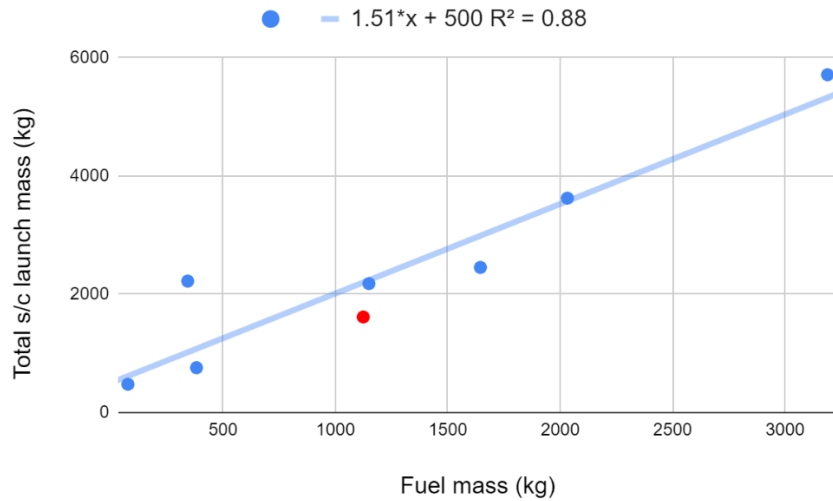


Figure 6.2 – Fuel mass vs. total spacecraft launch mass for existing spacecraft and MMRS (red).

Note that the MMRS “fuel mass percentage of total mass” value of 69.55% in table 6.9 is reasonably high compared to the average value of 56.40% (not considering Galileo or New Horizons). However, this is only slightly higher than that of MAVEN, with a percentage of 67.03%, and is thus considered acceptable. The orbital delta-v budget considers a 3.19 km/s delta-v for the orbit-insertion phase of the Hohmann transfer, which is discussed in chapter 7. Note that considering a smaller delta-v value would decrease the fuel requirement and mass.

6.6.2 Approximate Spacecraft Dimensions

Table 6.10 below provides the dimensions and structure volume of several in-family spacecraft. These values consider only the spacecraft bus and omit solar panels or antennas, where applicable. Note that the structure volume assumes that the spacecraft is a perfect cylinder. Figure 6.3 plots spacecraft launch mass against spacecraft volume for existing spacecraft and MMRS. The resulting R^2 value of 0.468 indicates that only a loose correlation between these parameters exists.

Table 6.10 – Dimensions of existing spacecraft and MMRS.

Spacecraft	Structure height (m)	Structure width (m)	Structure depth (m)	Structure volume (m ³)
Mars Reconnaissance Orbiter [71]	6.5	2.9	2.9	54.67
Mars Odyssey [72]	1.7	2.6	2.2	9.72
Mars Global Surveyor [73]	1.80	1.17	1.17	2.46
Mars MAVEN [37]	2.3	2.3	2.0	10.58
Juno [38]	3.5	3.5	3.5	42.76
Galileo [74]	5.3	4.6	4.6	112.15
Cassini [42]	6.7	4.0	4.0	107.20
New Horizons [75]	2.7	2.2	2.1	12.47
MMRS	2.93	2.64	2.64	20.42

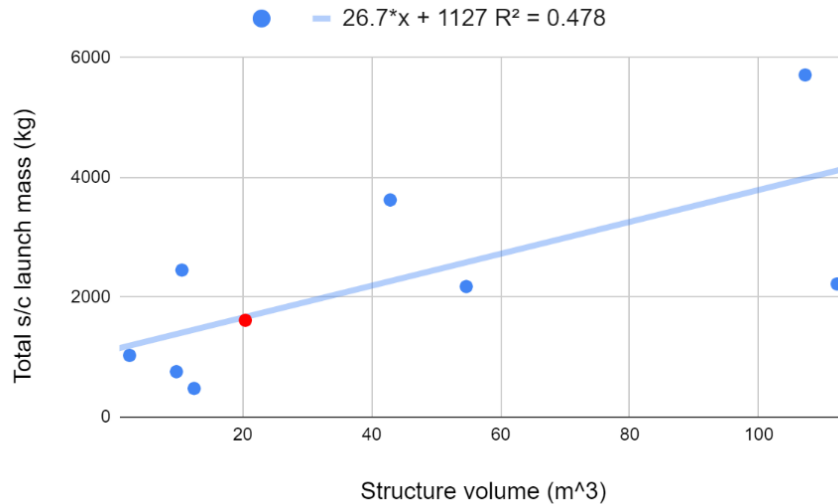


Figure 6.3 – Total spacecraft launch mass vs. structure volume for existing spacecraft and MMRS (red).

6.6.3 Mechanisms, Deployables, & Packaging

A low-weight high-density design must be traded against the ability to access individual internal components before launch for testing or replacement. The payload and means of attitude control influence the configuration of the spacecraft. For spin-stabilized spacecraft, the mass moment of inertia must be greatest about the spin axis. In 3-axis stabilized spacecraft, the magnetometer and magnetic torque rods must be placed such that no magnetic interference occurs between them. Sensors must be positioned such that their field of view is unobstructed by such components as antennas or solar arrays. Communication antennas, in addition to requiring a clear field of view, also require rigidity and thermoelastic stability. Such sensors and antennas may be constructed of composite materials and mounted on deployable appendages to meet such

requirements. Command and data handling (C&DH) components are often buried in the center of the spacecraft to shield them from the harsh radiation environment of space, as C&DH components are particularly vulnerable. Thruster modules are located far from the center of mass of the spacecraft and must be placed such that their exhaust plume doesn't contaminate other spacecraft components. Batteries must be accessible for pre-launch testing and replacement and placed such that they can maintain their required temperature range.

Components may be made part of the load-bearing structure of the spacecraft if the structure is configured and components are packaged concurrently. Using common members and joints, fabrication costs can be lowered and weight allocations can more-easily be met. The structure should be designed with routes for wire bundles and propellant lines to eliminate the need to cut through the structure later. Joints connecting members made of different materials should be designed to allow for varying rates of thermal expansion.

Mechanisms can be classified as either high-cyclic or low-cyclic. High-cyclic mechanisms require frequent articulation. Such mechanisms include antenna gimbals, boom extensions, solar array pointing and tracking. Low-cyclic mechanisms are used less frequently and include antenna launch retention and deployment, solar array retention and deployment, and spacecraft/launch vehicle separation.

6.7 Structural Analysis

The primary natural frequencies of a stowed spacecraft can be approximated by representing the spacecraft as a beam that simulates the mass properties and core stiffness of the spacecraft. The axial natural frequencies and deflections are represented by equations 6.3 and 6.4, respectively. The lateral natural frequencies and deflections are represented by equations 6.5 and 6.6, respectively. For the MMRS, a three-dimensional computer aided design (CAD) model of an idealized uniform cylindrical beam composed of 7075 Aluminum was modeled in SolidWorks and imported into Ansys. This model is shown in figure 6.1 and incorporates the parameters provided in table 6.4. This notably includes a length of 2.93 m and radius of 1.32 m. Finite element analysis (FEA) was then performed using Ansys software, through which the first seven natural frequencies and mode shapes of this idealized MMRS were determined. This will be discussed in detail in sections 6.3.2 and 6.3.3.

6.7.1 Geometry, Mesh Generation, Boundary Conditions, & Load Factors

For the purposes of representing the stowed MMRS in the launch vehicle at launch, the MMRS can best be represented as a uniform cantilevered beam (with a distributed load) fixed at one end. To apply the boundary conditions in Ansys mechanical, a fixed support was applied to one face of the cylinder. To apply load factors in Ansys mechanical, a lateral acceleration load of 2.0 G's and an axial acceleration load of 6.0 G's was applied to the cylinder. These load factors consider both the steady-state (static) and transient vibration (dynamic) loads experienced, and are derived from the user manual of the Atlas V 400-series launch vehicle. Additional parameters of this vehicle and its launch environment are provided in table 6.3. As described in section 6.3,

the natural frequencies induced on the launch vehicles by axial and lateral loads are of particular interest. Axial loads experienced during launch are driven by vehicle thrust and drag profiles. Lateral loads are driven primarily by atmospheric disturbances, engine gimbal maneuvers, engine shutdown, and other limited-duration events. As this is an idealized analysis, only these axial and lateral loads will be considered.

In conducting the analysis, a mesh was first created. In Ansys mechanical, under “mesh” in the project tree, the element order was set to “program controlled” and the element size was specified as 1 in. Given the symmetry of the geometry, a mesh was generated with uniform elements distributed evenly throughout the shape. This resulted in a mesh of 265,876 nodes and 38,048 elements. The mesh generated for this analysis is provided in figure 6.4. Note that the mesh is composed of uniform rectangular elements (with any visible distortion being a product of scaling the image to fit on this document). Mesh parameters used in completing a grid convergence study are provided in tables 6.11 and 6.12.

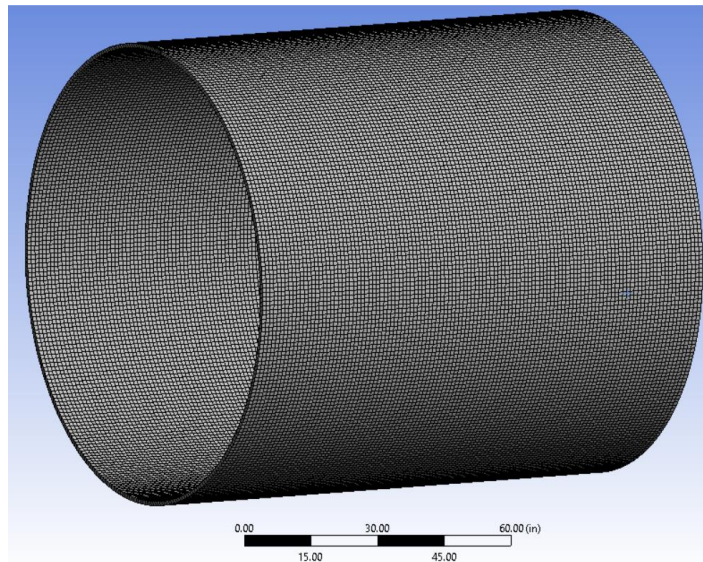


Figure 6.4 – Mesh of cylindrical beam.

6.7.2 Static Structural Analysis

In identifying the maximum stress experienced by the beam, equivalent (von-mises) stress was the parameter of interest. However, total deformation, max principal stress, and strain were also computed. These values are provided in table 6.11. For a maximum element number of 134,288, the von mises stress converged to a value of $6.41E+05$. However, by 38,048 elements, the solution is already reasonably converged.

Table 6.11 – Structural parameters per element count.

Element #	Total deformation (m)	Equivalent stress (Pa)	Max. principal stress (Pa)	Strain
352	9.90E-6	5.05E+05	6.54E+05	7.11E-6
816	9.90E-6	5.24E+05	7.12E+05	7.37E-6
3168	9.90E-6	5.38E+05	7.64E+05	7.57E-6
12408	9.90E-6	5.48E+05	8.04E+05	7.57E-6
24288	9.90E-6	5.80E+05	7.98E+05	8.25E-6
38048	9.91E-6	6.40E+05	8.55E+05	9.07E-6
134288	9.91E-6	6.41E+05	9.22E+05	9.04E-6

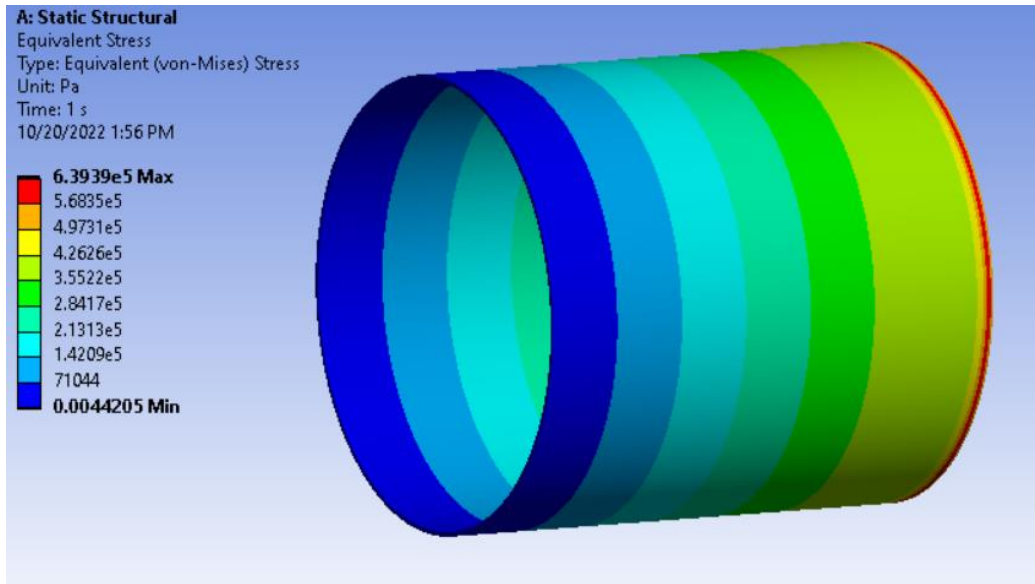


Figure 6.5 – Contour of maximum equivalent stress.

To ensure that the mesh size is adequate and that the value of equivalent stress is converged, a convergence analysis was conducted. This is shown in figure 6.6. Equivalent principal stress is plotted against element number.

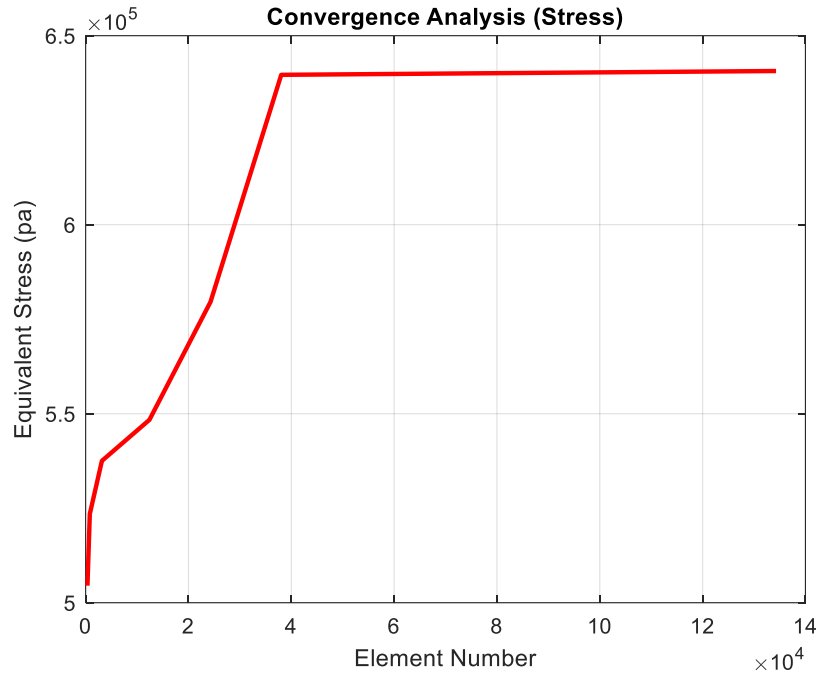


Figure 6.6 – Stress convergence analysis.

6.7.3 Modal Analysis

In identifying the first seven natural frequencies and modes experienced by the beam, a modal analysis was conducted. Values of natural frequency with respect to mode shape per number of elements are provided in table 6.12. Value convergence occurs at approximately 38,048 elements, though more elements were used to show convergence. These first seven mode shapes were then plotted. Still images of each mode are provided in figure 6.7.

Table 6.12 – Natural frequency (Hz) of each mode per element count.

Element #	Mode 1	Mode 2	Mode 3	Mode 4	Mode 5	Mode 6	Mode 7
352	48.414	48.414	56.438	56.438	74.783	74.783	83.016
816	48.408	48.408	56.407	56.407	74.789	74.789	82.933
3168	48.394	48.394	56.395	56.395	74.77	74.77	82.912
12408	48.378	48.379	56.38	56.382	74.745	74.745	82.884
24288	48.373	48.373	56.381	56.383	74.735	74.736	82.895
38048	48.367	48.367	56.377	56.378	74.725	74.726	82.888
134288	48.361	48.361	56.376	56.376	74.715	74.715	82.892

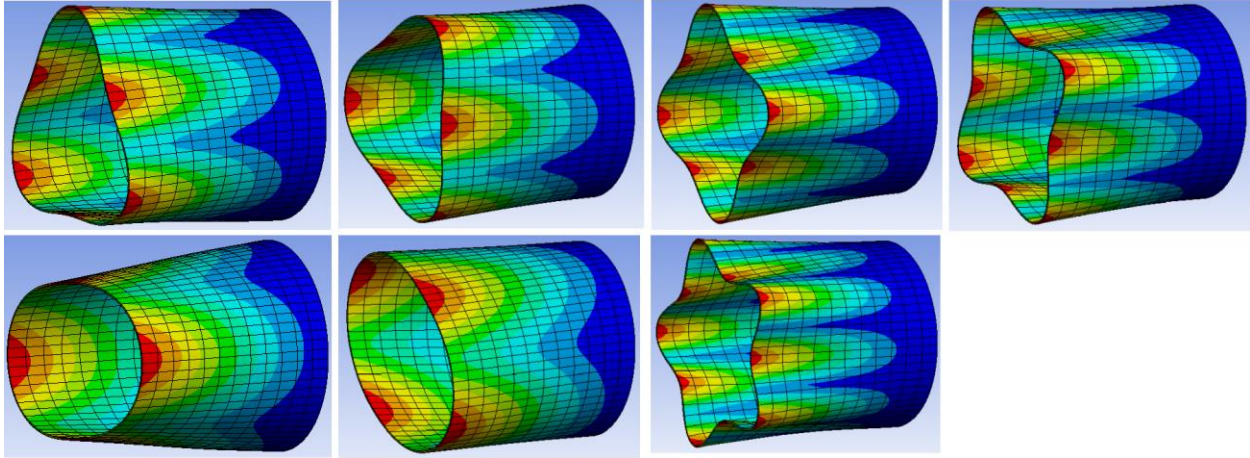


Figure 6.7 – The first seven mode shapes (left to right, top to bottom, modes 1 through 7).

To ensure that the mesh size is adequate and that the natural frequency for each mode is converged, a convergence analysis was conducted, and is shown in figure 6.8. In this plot, natural frequency is plotted against element number. Note that there is overlap.

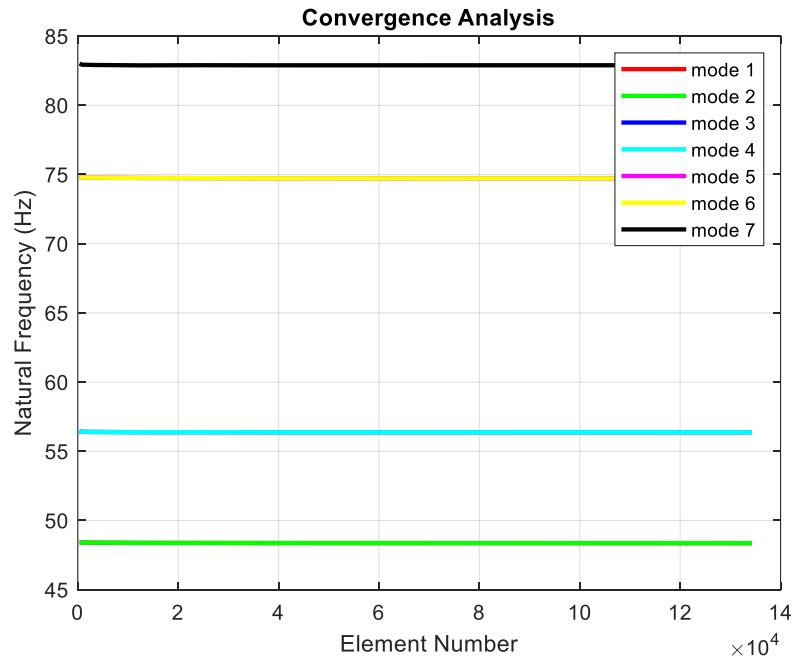


Figure 6.8 – Natural frequency convergence analysis.

6.8 Block Diagram

A block diagram of the structure subsystem illustrating deformation is provided in figure 6.9 below. The input variables are axial load (F), cross section area (A), young's modulus (E), and length (L). These variables flow into the material, structural loads, and the satellite's geometry and mass. The output vector is the change in length produced by deformation. The governing equations used for these calculations are provided in the section 6.3 of this document.

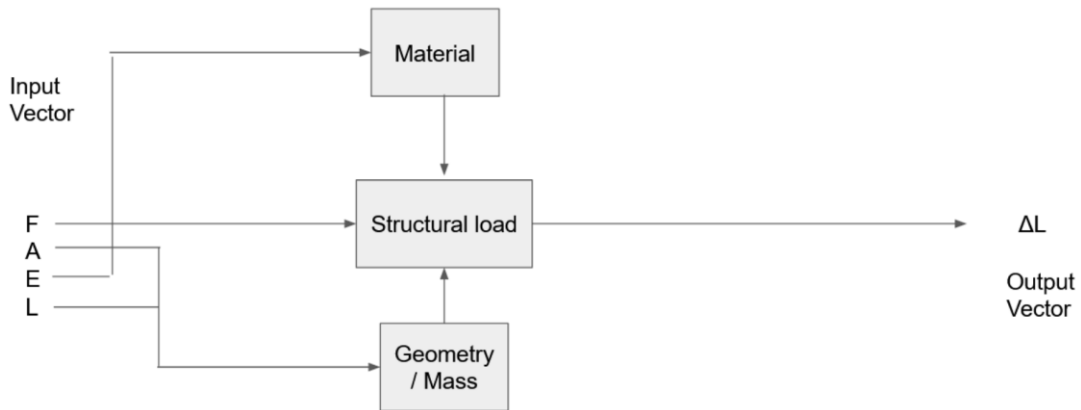


Figure 6.9 – High-level block diagram of the structure subsystem illustrating deformation.

The block diagram shown in figure 6.10 illustrates the derivation of spacecraft equivalent axial loads. The input vectors consist of the axial limit load (P_{axial}), idealized cylinder radius (R), bending moment of the limit load (M), and spacecraft mass (m). The governing equations pertaining to these vectors are equations 6.9 and 6.10.

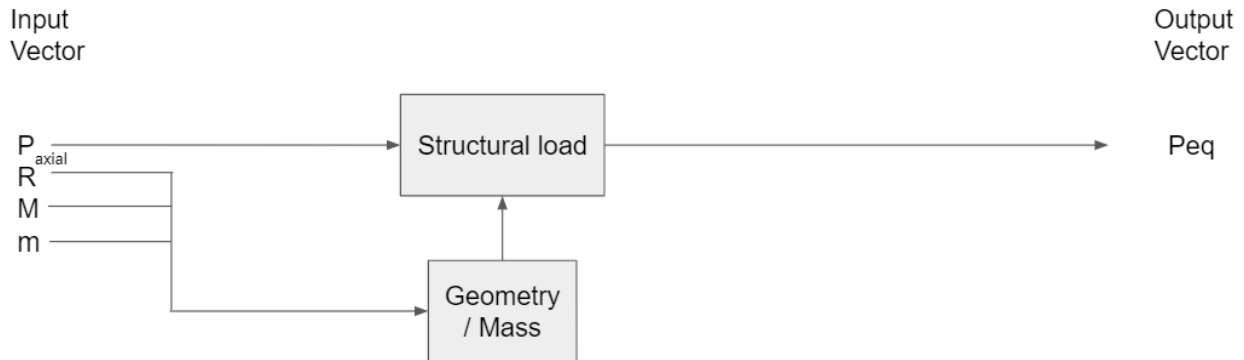


Figure 6.10 – High-level block diagram of the structure subsystem illustrating limit loads.

6.9 Verification & Validation

Tables 6.13 and 6.14 present information regarding the verification and validation of the structure subsystem. The listed requirements are designated as either “shall” or “should” requirements, and are then ranked on a scale of 1-10 as to the degree to which the requirements are verifiable, achievable, logical, integral, and definitive. [27] A verification method is then given for that requirement, as is an overall ranking, which is an average of the 5 aforementioned factors.

Table 6.13 – Structure subsystem verification and validation (part 1).

Category	System ID	Requirement description	Justification
Structure	5.1	Structure shall support the weight of the entire spacecraft bus and payload during each mission phase	Required for optimal operation
	5.2	Structure shall support mounting of all the subsystem modules, decks, and equipment	Required for optimal operation
	5.3	MMRS spacecraft shall withstand launch dynamics	Dictated by launch environment
	5.4	Structure shall possess sufficient rigidity to keep the MMRS from violating the dynamic envelope of the launch vehicle fairing	Required for optimal operation
	5.5	Structure should be able to support a weight of approximately 1616 kg	Calculated mass of MMRS
	5.6	The spacecraft shall withstand 10 g axial and 5 g lateral vibration loads during launch	Dictated by launch vehicle
	5.7	The first axial natural frequency of the MMRS shall be above 15 Hz	Dictated by launch vehicle
	5.8	The first lateral (bending) natural frequency shall be above 8 Hz	Dictated by launch vehicle
	5.9	A factor of safety of 1.25 (ultimate) and 1.10 (yield) should be heeded	Convention

Table 6.14 – Structure subsystem verification and validation (part 2).

Category	System ID	Shall / Should	Verifiable (1-10)	Achievable (1-10)	Logical (1-10)	Integral (1-10)	Definitive (1-10)	Verification method	Overall (1-10)
Structure	5.1	Shall	9	8	10	8	10	FEA	9
	5.2	Shall	9	9	10	8	10	FEA	9.2
	5.3	Shall	9	9	9	8	9	FEA	8.8
	5.4	Shall	9	10	9	8	8	FEA	8.8
	5.5	Should	10	10	9	8	8	Static testing	9
	5.6	Shall	10	10	10	10	10	FEA	10
	5.7	Shall	10	10	10	10	10	FEA	10
	5.8	Shall	10	10	10	10	10	FEA	10
	5.9	Should	10	10	9	8	8	FEA	9
	5.10	Should	10	10	9	8	8	Static testing	9

6.10 Test Plan

To test the structure and mechanisms subsystem, the spacecraft must be subject to shock and vibration testing to simulate launch characteristics. Such vibration testing may be performed at NASA Johnson Spaceflight Center. This center specializes in shock testing, vibroacoustics, and is able to simulate launch-induced vibrations. The Spacecraft Vibration Laboratory in particular has been used to test large space structures, including for the International Space Station. In this facility, large test articles may be supported by pneumatic springs and subjected to high force to simulate rocket-induced loads. Tests performed include high-force vibration, shock vibration, and fixed-base modal testing. [76]

6.11 Risk Assessment

A risk assessment was performed for the structures and mechanisms subsystem, which is shown in table 6.15 below. The rubrics used in determining these risk levels are provided in appendix C.1. The risks associated with the spacecraft structure include outgassing, hardware decay, sharp corners, and deformation. Sharp corners can be mitigated with proper manufacturing techniques. Outgassing can be mitigated by material testing. Structural deformation can be mitigated through finite element analysis. The risks associated with the thermal subsystem have a low likelihood of occurring given the heritage associated with the components.

Table 6.15 – Propulsion subsystem risk assessment.

Level	Risk	Mitigation
B,1	Outgassing	Testing
A,1	Hardware decay	Vibration testing
A,1	Sharp corners	Machining
A,1	Deformation	FEA

7.0 Orbital Mechanics and Mission Design

Several interplanetary mission profiles were investigated for the purpose of sending the MMRS spacecraft to outer solar system destinations. For the purpose of this document, a Hohmann transfer from Earth to Mars will be investigated.

7.1 Hohmann Transfer

A Hohmann transfer is a type of elliptical orbit used to travel between any two circular orbits. A notable attribute of Hohmann transfers that makes them desirable for certain mission architectures is that they consume the lowest possible quantity of propellant required for a transfer between two circular orbits. A general overview of a Hohmann transfer between Earth and Mars is shown in figure 7.1.

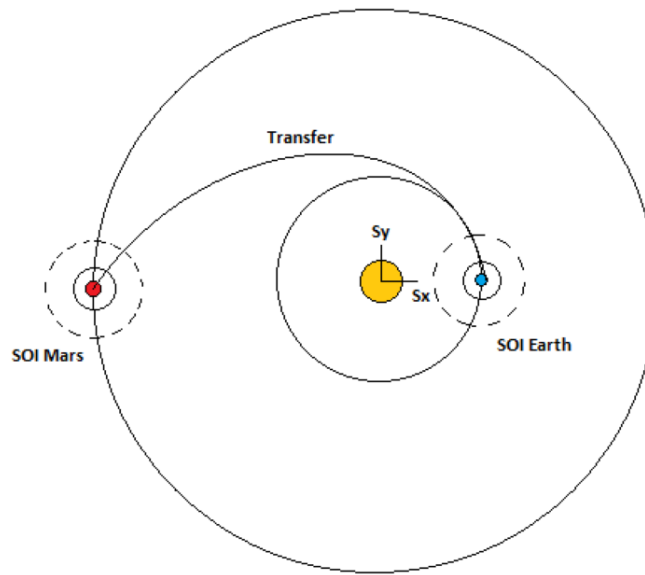


Figure 7.1 – General illustration of Earth-Mars Hohmann transfer.

For the mission profile discussed in this document, the spacecraft (identified as a point-mass, Q) is initially in a LEO parking orbit. From LEO, a delta- v burn is made that boosts the spacecraft into a hyperbolic departure trajectory (with respect to Earth). This hyperbolic departure trajectory has velocity V_{inf_d1} . As the spacecraft crosses the sphere of influence (SOI) boundary of Earth, it will have the correct velocity for the heliocentric transfer ellipse. No actual propulsive burn is required to transfer the spacecraft from the hyperbolic departure trajectory (with respect to Earth) to the heliocentric ellipse (with respect to the sun). It is only required that V_{inf} of the hyperbola (with respect to Earth) is equal to the velocity increment required for the transfer ellipse (with respect to the sun).

At the SOI boundary of Earth (which will be considered planet 1), the velocity of spacecraft Q with respect to Earth is V_{inf_d1} . When spacecraft Q arrives at Mars (which will be considered

planet 2), it will enter a circular orbit. The velocity increment needed for Q to transfer from the heliocentric ellipse to the circular orbit of Mars is V_{inf_a2} .

Rather than treat this as a traditional three-body problem, this mission profile will be broken into a series of two-body problems. This can ultimately be broken up into five conic sections. These include:

- Circular LEO
- Hyperbola around Earth
- Ellipse around the Sun
- Hyperbola around Mars
- Circular LMO

Starting at a circular LEO, a burn is made to go on the transfer trajectory. This is a hyperbolic trajectory with Earth as the primary. When the spacecraft approaches the sphere of influence boundary of Earth, this hyperbolic trajectory with respect to Earth becomes an elliptical trajectory with respect to the sun. When the spacecraft approaches Mars, the trajectory of the spacecraft with respect to the sun is an ellipse. When the spacecraft passes through the sphere of influence boundary of Mars, the trajectory is a hyperbola with respect to Mars. At this point, a burn may be made to either get into a circular low Mars orbit, or perform a gravity assist to another planet. For the purposes of this mission, the spacecraft will enter into a circular low Mars orbit.

7.1.1 Constants & Assumptions

The following assumptions are considered.

- Patched-conic approximation will be considered.
- Restricted 2-body problem will be considered.
- The transit time for a flyby is small with respect to large orbits
- The center of planet one (Earth) is the departure location. The center of planet 2 (Mars) is the arrival location.
- Earth and Mars are in near-circular heliocentric orbits.

Due to the patched-conic approximation, the trajectory can be divided into a series of two-body segments where the motion during each orbit segment is dominated by just one central attracting body. Due to the restricted 2-body problem assumption, the gravity of the spacecraft is considered to have a negligible effect on Earth or Mars (or any other body involved). As the transit time for the flyby is considered to be small with respect to large orbits, the cross product of (angular velocity of Earth with respect to the sun) x (position of the spacecraft with respect to Earth) is 0.

The following constants are considered, as shown in table 7.1. Note that the gravitational constant G has a value of $6.67 \times 10^{-20} \text{ km}^3/(\text{kg} \cdot \text{sec}^2)$.

Table 7.1 – Mass and radius constants.

	Mass (kg)	GM (km ³ /sec ²)	Radius (km)	Distance to Sun (km)
Earth	5.972 x 10 ²⁴	398,332	6,378	150,000,000
Mars	6.4169 x 10 ²³	42,800	3,389	211,339,054
Sun	1.989 x 10 ³⁰	1.327 x 10 ¹¹	695,800	N/A

7.1.2 Delta-V Calculations

The total delta-v required to send a spacecraft on an interplanetary trajectory from Earth to Mars using a Hohmann transfer was calculated. A delta-v of 3.65 km/sec is required to boost the spacecraft from LEO onto the transfer ellipse around the sun. This value agrees with the value established in the literature. An additional delta-v of 3.19 km/sec is required to enter the spacecraft into orbit around Mars. This results in a total delta-v of 6.84 km/sec. The time required for this Hohmann transfer to be completed is 278.5 days. These calculations are provided in appendix B. As the time required for the delta-v burn is small compared to total time required to complete the orbit, the delta-v burn is assumed to be instantaneous. Thus, transient effects will be neglected. Were an electric propulsion system chosen instead chemical propulsion, transient effects would need to be considered. [77]

7.1.3 Wait Time

A critical factor in designing a Hohmann transfer is determining the wait time. Wait time refers to the time that is required before the Hohmann transfer can occur such that the interceptor body can rendezvous with the target body once the Hohmann transfer is complete. An equation for calculating wait time is provided in equation 7.1 below. This equation, and the others necessary for calculating wait time, are provided in appendix B.

$$wait\ time = \frac{\Phi_i - \Phi_f}{\omega_{int} - \omega_{tgt}} \quad (5.1)$$

Wait time was calculated for several values of true anomaly. A true anomaly of 180 degrees was used in one case, indicating conditions when Earth and Mars are on opposite sides of the sun when the Hohmann transfer is initiated (which is the case shown in figure 7.1). Thus, the spacecraft and Mars are also on opposite sides of the sun. Table 7.2 below provides wait time, in addition to the angles that the spacecraft and Mars sweep out during the wait time, for several true anomaly values. For the Hohmann transfer itself, the transfer time and the angle through which Mars moves during the maneuver are provided below.

- Transfer time: 6,684.2 hours = 287.5 days = 9.2 months
- Angle through which Mars moves during Maneuver: 127.6 deg

Table 7.2 – Wait time and associated values for several values of true anomaly.

True Anomaly (deg)	Wait time (days)	Angle Earth Travels during Wait Time (deg)	Angle Mars Travels during Wait Time (deg)
0	531.65	537.33	243.59
52.39306	0	0	0
90	65.00	65.69	29.78
180	220.55	222.91	101.05
270	376.10	380.12	172.32

7.1.4 Equations of Motion

Using the reference frame illustrated in figure 7.2, the equations of motion for a spacecraft orbiting a central body can be derived. These derivations are detailed extensively in appendix B of this document. Note that, instead of Earth being the central body, the sun is considered the central body. Using the rotation tables developed in appendix B, the spacecraft particle Q can be resolved into the sun-centered (ECI) basis vectors.

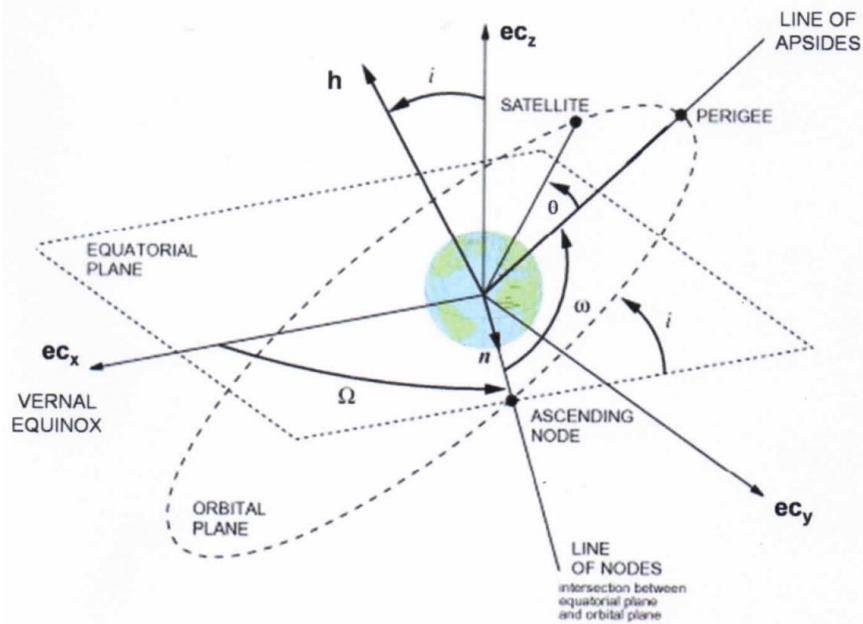


Figure 7.2 – Depiction of Earth-centered reference frame. [78]

7.1.5 Orbit Simulation

Using the MATLAB script provided in appendix B, several position and velocity vectors were calculated. The orbits of Mars, Earth, and the elliptical transfer orbit between Mars and Earth about the sun were calculated using the following orbital parameters and Keplerian elements, which are the real orbit parameters of Earth and Mars. Several of the Keplerian elements of the transfer orbit are the same as those of Earth for simplicity.

Table 7.3 – Keplerian elements of each orbit.

	Earth	Mars	Transfer
ra (km)	152.1×10^6	249.261×10^6	249.261×10^6
rp (km)	147.095×10^6	206.650×10^6	147.095×10^6
a	149.597×10^6	227.955×10^6	198.178×10^6
e	0.0167	0.0935	0.2578
θ (deg)	0	0	0
i (deg)	0.00005	1.85061	0.00005
Ω (deg)	-11.26064	49.57854	-11.26064
ω (deg)	102.94719	336.04084	102.94719

The following position and velocity vectors were then calculated. A plot of the orbits of Earth and Mars about the sun, as well as the Hohmann transfer orbit, are shown in figure 7.3.

Earth

- $R: -0.0433 \times 10^8 \mathbf{s_x} + 1.4703 \times 10^8 \mathbf{s_y} + 0 \mathbf{s_z}$
- $V: -30.2688 \mathbf{s_x} - 0.8912 \mathbf{s_y} + 0 \mathbf{s_z}$

Mars

- $R: 1.8630 \times 10^8 \mathbf{s_x} + 0.8938 \times 10^8 \mathbf{s_y} - 0.0271 \times 10^8 \mathbf{s_z}$
- $V: -11.4466 \mathbf{s_x} + 23.8820 \mathbf{s_y} + 0.7819 \mathbf{s_z}$

Transfer

- $R: -0.0433 \times 10^8 \mathbf{s_x} + 1.4703 \times 10^8 \mathbf{s_y} + 0 \mathbf{s_z}$
- $V: -33.6661 \mathbf{s_x} - 0.9913 \mathbf{s_y} + 0 \mathbf{s_z}$

For a trajectory to a planet other than Mars, the Keplerian of the transfer orbit can be modified such that the elliptical orbit would intersect the orbit of the planet chosen. Varying radius of perigee and apogee accordingly, calculating new Keplerian elements, and using these Keplerian elements as inputs to the MATLAB code provided in appendix B, would allow this to be done. Likewise, parameters of the planetary orbit can be modified to solve for the appropriate delta-v and wait time of the maneuver.

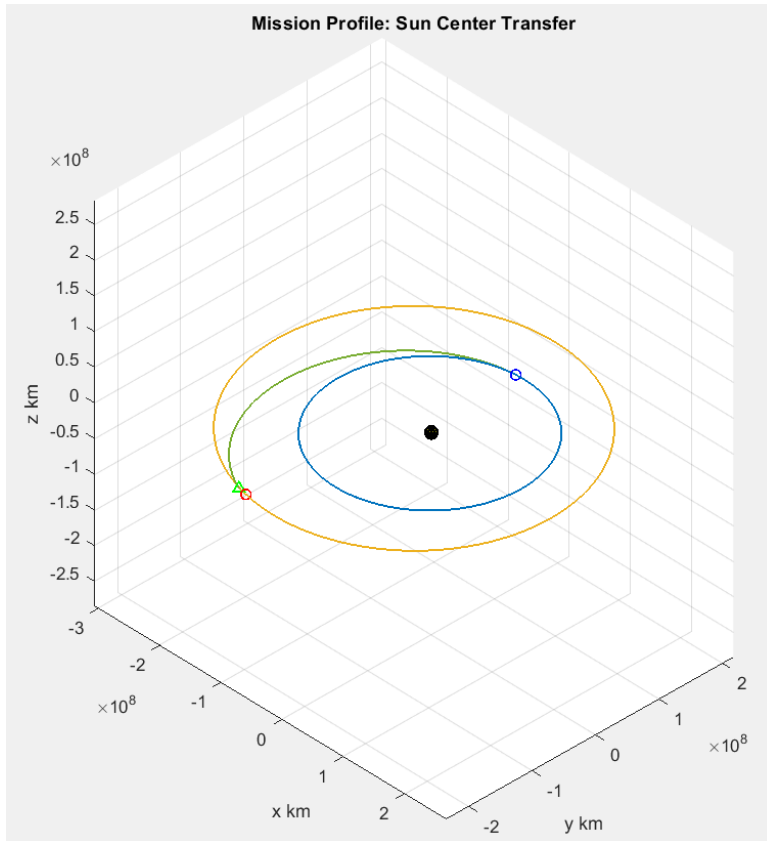


Figure 7.3 – Animation of spacecraft Q on a Hohmann transfer from Earth to Mars.

7.2 Launch Vehicle

The selected launch vehicle for the MMRS is the United Launch Alliance Atlas V 401 series. Several launch vehicles and their respective masses to orbit are elaborated upon in table 6.2. Values specific to the ULA Atlas V-401 are provided in table 6.3 of this document and are further elaborated upon in appendix A.14. Note that other similarly-classed launch vehicles could also be used. However, the natural frequencies of the launch vehicle would need to be taken into account, following the procedure performed in chapter 6. Additional considerations include launch system reliability, availability, cost, fairing size, orbital insertion accuracy, and interfaces to the launch site and spacecraft. Note, however, that this list is far from exhaustive. [79]

8.0 Overall System Diagrams & Specifications

8.1 System Diagrams

A block diagram of the five spacecraft subsystems discussed in this document and their relevant variables is provided in figure 8.1 below. The input variables are the variables from each of the individual subsystem block diagrams from the previous sections of this document, aggregated together. The output variables are antenna diameter, thermal radiator area, delta-v, and solar array area with the addition of cost, which are similarly the output variables of the aforementioned individual block diagrams. Together, this illustrates a general high-level overview of the relationships between the variables and subsystems of the MMRS discussed in this document.

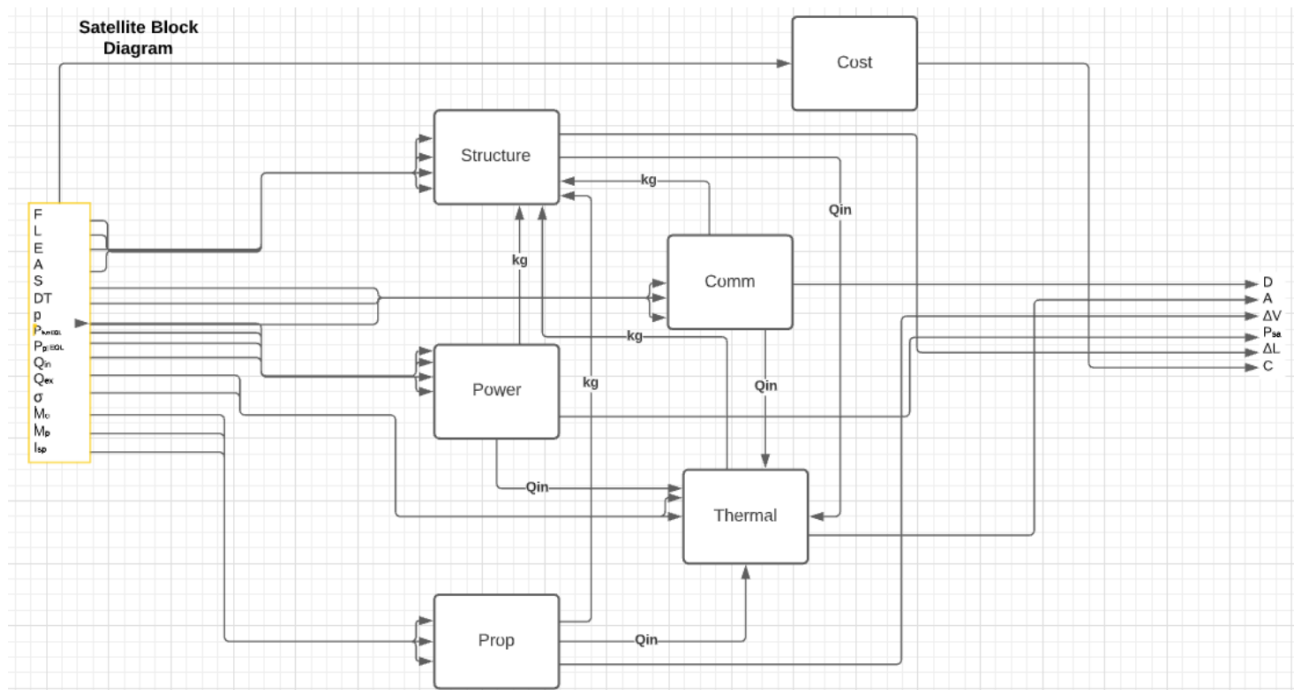


Figure 8.1 – Overall high-level MMRS block diagram.

Figures 8.2 and 8.3 provide a random and ordered N^2 diagram, respectively, of the five subsystems of the MMRS explored in this document. The lines connecting each subsystem represent the interface variables between subsystems. The random N^2 diagram represents an initial guess (i.e., iteration) of the overall system design with the presence of feedback loops. The ordered N^2 diagram represents the point at which the convergence threshold has been reached, with feedback loops eliminated.

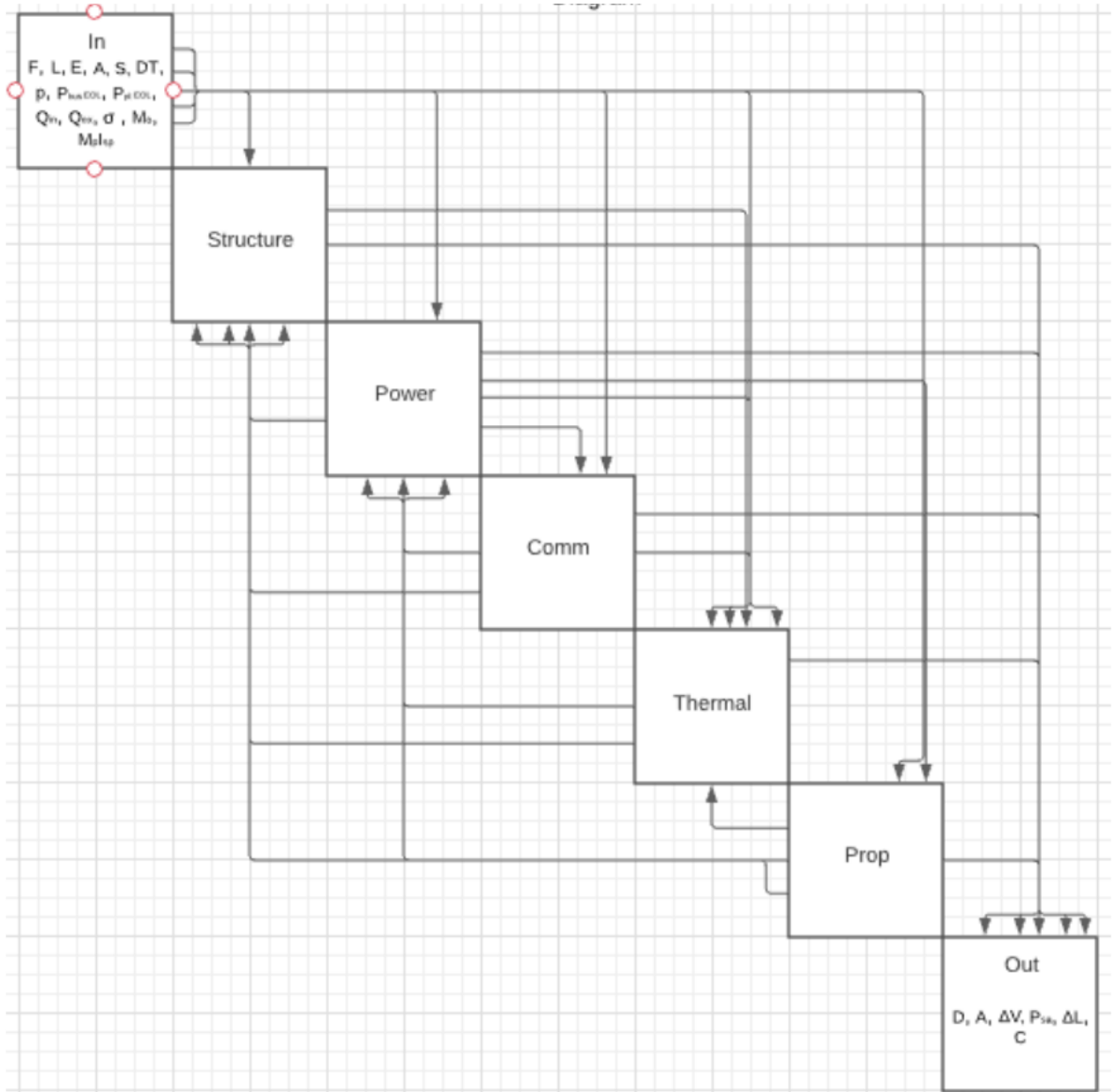


Figure 8.2 – MMRS random N^2 diagram.

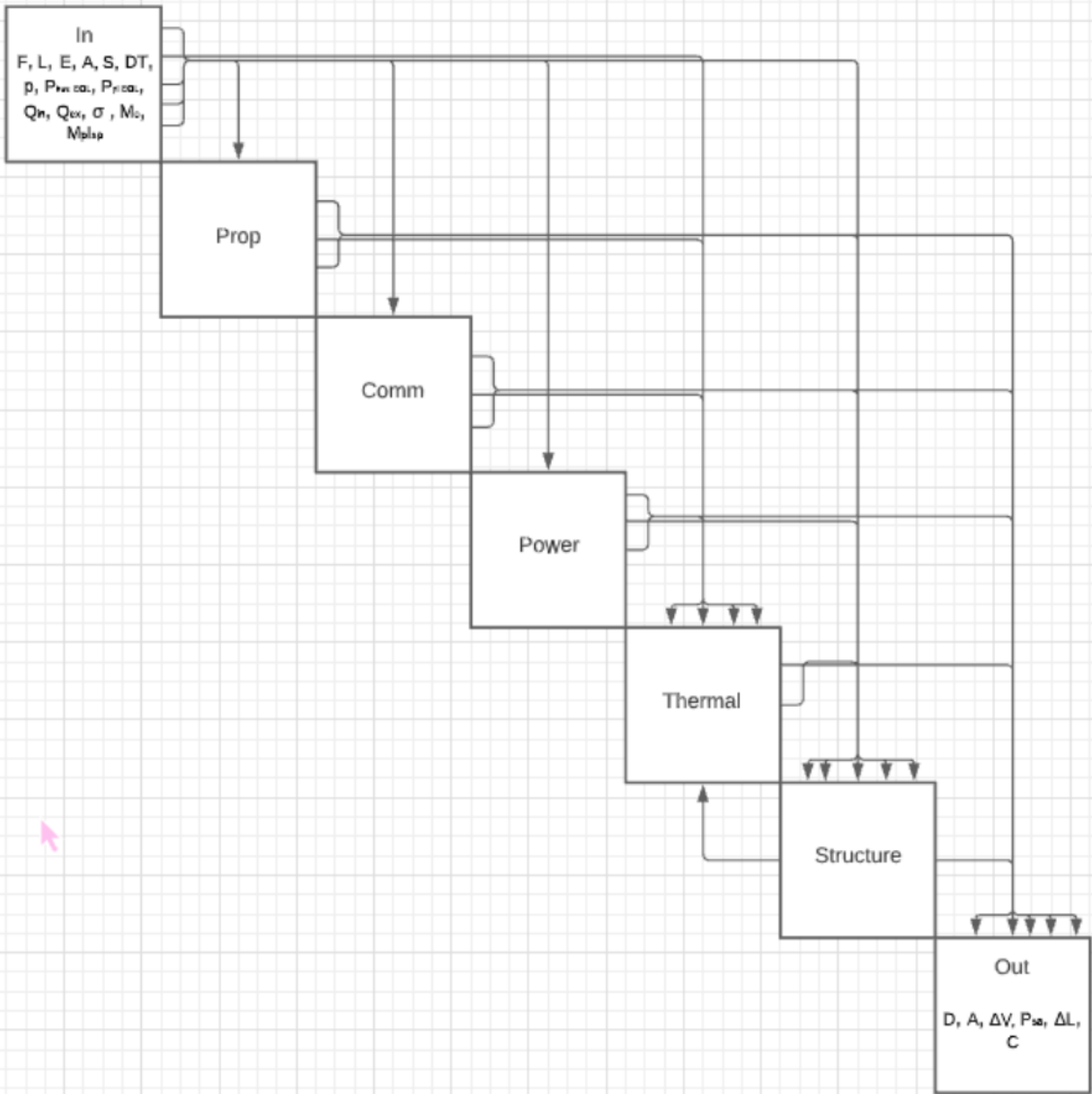


Figure 8.3 – MMRS ordered N^2 diagram.

8.2 System Specifications

Utilizing the information presented in the preceding sections of this document, a select number of the key sizing parameters of the communication, power, propulsion, thermal, and structure subsystems have been aggregated for reference purposes and are provided in the tables below. The full range of parameters are provided in appendix A of this document.

Table 8.1 – Communication subsystem sizing.

X-band data downlink (telemetry)	Max. data rate	6.34 Mbps
	Efficiency factor	0.55
	Antenna diameter	3.0 m
	Antenna mass	50.3 kg
	Transmit power	44.40 dBm
	Frequency	8.40 GHz
	Peak Gain	44.25 dB
	EIRP	85.65 dB
	Half-power beamwidth	1.0 deg
	Eb/No available	20.21 dB
	Eb/No required	9.60 dB
	Space loss	-284.46 dB
	G/T	49.1 dB
	C/No	77.4 dB
X-band data uplink (command)	Max. data rate	2000 bps
	Efficiency factor	0.55
	Antenna diameter	N/A
	Antenna mass	N/A
	Frequency	7.15 GHz
	Peak Gain	44.44 dB
	Half-power beamwidth	1.00
	Space loss	-283.06 dB
	G/T	16.06 dB
	C/No	-38.12 dB
Ka-band downlink (telemetry)	Max. data rate	6.34 Mbps
	Efficiency factor	0.55
	Antenna diameter	N/A
	Antenna mass	N/A
	Transmit power	45.15 dBm
	Frequency	32.0 GHz
	Peak Gain	59.15 dB
	EIRP	101.3 dB
	Half-power beamwidth	0.18 deg
	Eb/No available	0.82 dB
	Eb/No required	9.60 dB
	Space loss	-296.08 dB
	G/T	60.67 dB
	C/No	68.60 dB
Communication subsystem mass breakdown (kg)	Electra UHF system	11.5
	HGA	50.3
	X-band TWTA	1.9
	Ka-band TWTA	0.8
	2 SDST	6.4

	2 LGA	2.2
	Wire harness & fasteners	5.1
	Miscellaneous (waveguides, diplexer, isolator, etc.)	20.4
	Total subsystem mass	98.6
Communication subsystem power breakdown (W)	Electra UHF system	71
	HGA	N/A
	X-band TWTA	172
	Ka-band TWTA	81
	2 SDST	16
	2 LGA	N/A
	Wire harness & fasteners	N/A
	Miscellaneous (HGA drive motors, USOs, etc.)	19
	Total subsystem power	359

Table 8.2 – Power subsystem sizing.

Power by subsystem (W)	Communication power	79.1
	Power subsystem power	110.7
	Propulsion power	19.0
	Thermal power	19.0
	Structure power	0
	ACS	63.9
	C&DH	26.4
	Margin`	192
	Payload power	279.9
	Reserve payload power	170.1
RTG parameters	Electrical power per RTG unit	356 W
	Type	MMRTG
	Quantity	3
	Total power decay per year	6 W
Power subsystem power breakdown (W)	Total spacecraft power required	960.1
	Spacecraft power generated BOL	1068
	Spacecraft power generated EOL	966
Power subsystem mass breakdown (kg)	Total RTG mass	130.8
	Miscellaneous (cabling, etc.)	13.08
	Total power subsystem mass	143.88

Table 8.3 – Propulsion subsystem sizing.

Tank parameters	Total propellant mass (kg)	1123.9
	Fuel mass (kg)	249.8
	Fuel tank volume (m ³)	0.29
	Fuel tank radius (m)	0.413
	Oxidizer mass (kg)	874.1
	Oxidizer tank volume (m ³)	0.62
	Oxidizer tank radius (m)	0.530
	Fuel type	1: MMH propellant / N ₂ O ₄ oxidizer 2: N ₂ O ₄ monopropellant
Propellant mass allocation (kg)	Orbit maneuver propellant mass allocation	839.5
	Attitude control propellant mass allocation	42.0
	Margin propellant mass allocation	220.4
	Residual propellant mass allocation	22.0
Performance parameters	Specific impulse (sec)	327
	Thrust (orbital insertion) (N)	1020
	Thrust (trajectory correction) (N)	22
	Thrust (attitude control) (N)	4.45
Propulsion subsystem mass breakdown (kg)	Total thruster mass	13.58
	Miscellaneous (lines, valves, tanks, regulators, etc.)	13.5
	Total propulsion subsystem mass	27.08
Propulsion subsystem power breakdown (W)	Miscellaneous	19

Table 8.4 – Thermal subsystem sizing and planetary constants.

Mars parameters	Solar flux at Mars	590 W/m ²
	Average Mars albedo	29%
	Maximum Mars IR emission	141 W/m ²
Absorbed/expelled heat parameters	Radiator area	0.887 m ²
	Radiator heat expelled	350 W/m ²
	Maximum power dissipation on spacecraft	960.1 W
	Solar energy absorbed	4570.0 W
	Albedo energy absorbed	1181.4 W
	Maximum IR energy absorbed	1300.9 W
Thermal subsystem mass breakdown (kg)	Total thermal subsystem mass	12.4

Thermal subsystem power breakdown (W)	Total thermal subsystem power	19.0
---------------------------------------	-------------------------------	------

Table 8.5 – Structure & mechanisms subsystem sizing.

Mass by subsystem (kg)	Payload	130
	ACS	29.2
	C&DH	15.1
	Power	101.9
	Propulsion	13.5
	Structure	79.2
	Thermal	12.4
	Communication	12.3
	Margin	98.4
	Propellant	1123.9
	Spacecraft dry mass	492
	Spacecraft wet mass	1615.9
	Fuel mass % of total mass	69.55
	Material properties (7075 Aluminum)	Young's modulus
Material density		2.800e3 kg/m ³
Ultimate tensile stress		5.240e8 N/m ²
Yield tensile stress		4.480e8 N/m ²
Factor of safety (ultimate)		1.25
Factor of safety (yield)		1.10
Rigidity	Axial deflection	0.020 cm
	Lateral deflection	0.017 cm
Cylinder parameters	Length	2.93 m
	Radius	1.32 m
	Skin thickness	1.156e-1 cm
	Cross sectional area	9.621e1 cm ²
	Area moment of inertia	8.434e5 cm ⁴
	Spacecraft volume	20.42 m ³
	Structure height	2.93 m
	Structure width	2.64 m
	Structure depth	62.64 m
Total monocoque structure components mass (kg)	Structural skin mass	79.0
	Fastener & fitting mass	7.9
	Total structure mass	86.9
Total structure subsystem power (W)	Total power	0

Table 8.6 – Orbital mechanics and mission sizing.

Mission sizing	Delta-v budget at Mars	3.19 km/s
	Delta-v fuel requirement for Hohmann orbit insertion	1018.12 kg
	Mission life	17 yr

9.0 Path Forward

Each individual component in the spacecraft was not specified in this document. As such, the design of each subsystem is limited in scope. Future work would entail a more-detailed design of the MMRS spacecraft overall, such that components and interfaces between components could be defined in more detail. Each subsystem would then have dozens of individual requirements (with this document currently listing only high-level requirements). Interface requirements between subsystems additionally could be more-deeply explored (with such interfaces being illustrated by the N^2 diagram of chapter 8). More-thorough description of testing procedures could be included, as could a more-exhaustive list of risks in risk analysis for each subsystem. Additional and more-comprehensive block diagrams could be generated for individual subsystem components. Additional design iterations could be performed that consider more-accurate component masses for each subsystem.

With respect to the communication subsystem, lasers generating narrow-band energy at optical frequencies have been identified in the literature as an alternative to using microwave frequencies. This approach is best-suited for satellite-to-satellite communication as atmospheric effects severely attenuate optical links. Such links have been designed with capacities above 300 Mbps. Optical crosslinks allow for high data rates compared to microwave crosslinks as they can obtain extremely narrow beamwidths and high gains. Unlike with microwave communication, frequency allocation is not a concern. [13] Reserve power was allocated to the MMRS communication subsystem with the intent that laser communication could be explored and implemented on future spacecraft.

With respect to the power subsystem, mission to Mars, Jupiter (i.e., NASA's Juno spacecraft), and Jupiter's moon Europa (i.e., NASA's Europa Clipper spacecraft) have flown (or will be flown) utilizing advanced solar panels capable of producing energy with only a fraction of the sunlight received by inner solar system spacecraft. For the purpose of versatility of mission destination, mission length, and mission composition, radioisotope thermal generators were chosen for the MMRS spacecraft. However, the use of advanced solar panels could be investigated for future spacecraft. This may be relevant, as the regulatory approval for MMRTGs is a lengthy process. Additionally, the quantity of available plutonium may hinder the production of future RTGs. Furthermore, excess power generating capability was designed into the MMRS as to promote mission versatility, enabling power to be available for added or upgraded instruments. This power is allocated by the 170.1 Watts of reserved power, as listed in table 8.2. Additional instruments (such as the aforementioned laser communication) could be explored. The design of the power distribution subsystem could additionally be addressed.

With respect to the thermal subsystem, calculating q_{backload} requires geometric modeling that is beyond the scope of this design. As such, approximate values were used based on historical data. However, this calculation could be explored as part of future work.

With respect to the structures and mechanisms subsystem, the mechanical design of the actual spacecraft structure could be investigated as, currently, this paper approximates the MMRS to be a cylinder.

References

- [1] Lorenz, D. R., “Post-Cassini Exploration of Titan: Science Rationale and Mission Concepts,” *Journal of the British Interplanetary Society*, Vol. 53, 2000, pp. 218-234.
<https://www.lpl.arizona.edu/~rlorenz/jbis.pdf>
- [2] Chandler, W. C., “The Case for Deep Space Telecommunications Relay Stations,” NASA CR-2004-213053, April 2004.
<https://ntrs.nasa.gov/api/citations/20040066071/downloads/20040066071.pdf>
- [3] Asmar, S., Matousek S., “Mars Cube One (MarCO) Shifting the Paradigm in Relay Deep Space Operations,” AIAA Paper 2016-2483, May 2016.
<https://doi.org/10.2514/6.2016-2483>
- [4] Harbaugh, J., “Deep Space Optical Communications (DSOC),” NASA: Space Technology Mission Directorate, retrieved 22 Feb. 2022.
https://www.nasa.gov/mission_pages/tdm/dsoc/index.html
- [5] Yuen, J., “Deep Space Communications,” NASA Jet Propulsion Laboratory, retrieved 22 Feb. 2022.
<https://web.archive.org/web/20161203150128/http://scienceandtechnology.jpl.nasa.gov/research/research-topics-list/communications-computing-software/deep-space-communications>
- [6] Halpert, G., Frank, H., Surampudi, S., “Batteries and Fuel Cells in Space,” *The Electrochemical Society Interface*, Vol. 8, No. 3, 1999.
<https://www.semanticscholar.org/paper/Batteries-and-Fuel-Cells-in-Space-Halpert-Frank/0dde71431469fd095015681aea9223cd30c55d02>
- [7] Torabi, F., Ahmadi, P., “Battery Technologies,” *Simulation of Battery Systems: Fundamentals and Applications*, 1st ed., Academic Press, Massachusetts, 2020, pp. 6-35.
<https://www.sciencedirect.com/book/9780128162125/simulation-of-battery-systems>
- [8] Doody, D., “Basics of Space Flight,” NASA Jet Propulsion Laboratory, retrieved 22 Feb. 2022.
<https://web.archive.org/web/20080518124056/http://www2.jpl.nasa.gov/basics/bsf11-3.html>
- [9] Landau, E., “Spacecraft 'Nuclear Batteries' Could Get a Boost from New Materials,” NASA Jet Propulsion Laboratory, 13 Oct. 2016.
<https://www.jpl.nasa.gov/news/spacecraft-nuclear-batteries-could-get-a-boost-from-new-materials>
- [10] “NANOSTAR Methodology Documentation Release 1.0rc2,” NANOSTAR Project, 12 Sept. 2019.
<https://nanostar-project.gitlab.io/main/assets/NANOSTARMethodology.pdf>

[11] Pastore, R., Delfini, A., Santoni, F., Marchetti, M., Albano, M., Piergentili, F., Matassa, R., “Space Environment Exposure Effects on Ceramic Coating for Thermal Protection Systems,” *Journal of Spacecraft and Rockets*, Vol. 58, No. 5, 2021, pp. 1387-1393.

<https://doi.org/10.2514/1.A34997>

[12] Junwei, W., Lei, Z., Qingsheng, X., Gao, L., Xiao, H., Bing, B., “Research on Key Techniques of the Verification and Testing System for Spacecraft Propulsion,” *Proceedings of 2nd International Conference on Mechanical, Material and Aerospace Engineering*, Wuhan, China, 2018.

<https://doi.org/10.1051/mateconf/201817903008>

[13] Wertz, J. R., and Larson, W. J., “Communications Architecture,” *Space Mission Analysis and Design*, 3rd ed., Vol. 1, Springer, New York, 1999, pp. 533-585.

[14] “Link Budget Calculations For a Satellite Link With An Electronically Steerable Antenna Terminal,” Kymeta Corporation, Redmond, WA, June 2019.

<https://www.kymetacorp.com/wp-content/uploads/2020/09/Link-Budget-Calculations-2.pdf>

[15] Taylor, J., Lee, K. D., and Shambayati, S., “Mars Reconnaissance Orbiter Telecommunications,” NASA, Pasadena, CA, Sept. 2006.

https://descanso.jpl.nasa.gov/DPSummary/MRO_092106.pdf

[16] Makovsky, A., Barbieri, A., and Tung, R., “Odyssey Telecommunications,” NASA, Pasadena, CA, Oct. 2002.

https://descanso.jpl.nasa.gov/DPSummary/odyssey_telecom.pdf

[17] Taylor, J., Cheung, K., and Wong, C., “Mars Global Surveyor Telecommunications,” NASA, Pasadena, CA, May 2001.

https://descanso.jpl.nasa.gov/DPSummary/MGS_07Aug01.pdf

[18] Mukai, R., Hansen, D., Mittskus, A., Taylor, J., Danos, M., and Kwok, A., “Juno Telecommunications,” NASA, Pasadena, CA, Aug. 2017.

https://descanso.jpl.nasa.gov/DPSummary/Descanso16_Juno_RevA.pdf

[19] Taylor, J., and Wong, C., “Cassini Orbiter/Huygens Probe Telecommunications,” NASA, Pasadena, CA, Jan. 2002.

<https://descanso.jpl.nasa.gov/DPSummary/Descanso3--Cassini2.pdf>

[20] DeBoy, C. C., Haskins, C. B., Brown, T. A., Schulze, R. C., Bernacik, M. A., Jensen, J. R., Millard, W., Duven, D., and Hill, S., “The RF Telecommunications System for the New Horizons Mission to Pluto,” Institute of Electrical and Electronics Engineers, published online 22 Dec. 2003.

https://www.boulder.swri.edu/~tcase/NH%20RF%20Telecom%20Sys%20ID1369%20FINAL_Deboy.pdf

- [21] Shambayati, S., Morabito, D., Border, J. S., Davarian, F., Lee, D., Mendoza, R., Britcliffe, M., and Weinreb, S., “Mars Reconnaissance Orbiter Ka-band (32 GHz) Demonstration: Cruise Phase Operations,” NASA, Pasadena, CA, 16 June 2006.
<https://trs.jpl.nasa.gov/bitstream/handle/2014/39654/06-0902.pdf?isAllowed=y&sequence=1>
- [22] Kobayashi, M., Shihabi, M., and Taylor, J., “Mars Cube One Telecommunications Subsystem Design,” NASA, Pasadena, CA, Sept. 2021.
https://descanso.jpl.nasa.gov/DPSummary/DESCANSO18_MarCO.pdf
- [23] Stocklin, F. J., Rackley, M. W., and Sobchak, T. C., “Space Network Users’ Guide (SNUG),” NASA, Greenbelt, MD, Aug. 2012.
<https://web.archive.org/web/20160305123252/http://esc.gsfc.nasa.gov/assets/files/450-SNUG.pdf>
- [24] Chen, C., Shambayati, S., Makovsky, A., Taylor, F. H., Herman, M. I., and Zingales, S. H., “Small Deep Space Transponder (SDST) DS1 Technology Validation Report,” NASA, Pasadena, CA, April 2004.
https://pdssbn.astro.umd.edu/holdings/ds1-c-micas-3-rdr-visccd-borrelly-v1.0/document/doc_Apr04/int_reports/SDST_Integrated_Report.pdf
- [25] DeBoy, C. C., Haskins, C. B., Brown, T. A., Schulze, R. C., Bernacik, M. A., Jensen, J. R., Millard, W., Duven, D., and Hill, S., “The RF Telecommunications System for the New Horizons Mission to Pluto,” *2004 IEEE Aerospace Conference Proceedings*, IEEE, Big Sky, MT, 2004, pp. 1478.
https://www.boulder.swri.edu/~tcase/NH%20RF%20Telecom%20Sys%20ID1369%20FINAL_Deboy.pdf
- [26] Taylor, J., Cheung, K., and Seo, D., “Galileo Telecommunications,” NASA, Pasadena, CA, July 2002.
https://descanso.jpl.nasa.gov/DPSummary/Descanso5--Galileo_new.pdf
- [27] Sellers, J., “MBSE Applications,” *Applied Model-Based Systems Engineering (MBSE)*, 1st ed., Vol. 1, Teaching Science and Technology, Inc., Colorado, 2020, pp. 140-142.
- [28] Valipe, S., “Antenna Test Facility,” NASA.gov, Retrieved 20 November 2021.
<https://www.nasa.gov/centers/johnson/partnerships/eddc/hsvs/antenna-test-facility>
- [29] Wertz, J. R., and Larson, W. J., “Spacecraft Subsystems: Power,” *Space Mission Analysis and Design*, 3rd ed., Vol. 1, Springer, New York, 1999, pp. 407-427.
- [30] Wertz, J. R., and Larson, W. J., “Spacecraft Design and Sizing: Design Budgets,” *Space Mission Analysis and Design*, 3rd ed., Vol. 1, Springer, New York, 1999, pp. 314-318.
- [31] “Solar Radiation in Space,” PVEducation, retrieved 15 March 2022.
<https://www.pveducation.org/pvcdrom/properties-of-sunlight/solar-radiation-in-space>
- [32] Lyons, D. T., “Mars Reconnaissance Orbiter: Aerobraking Reference Trajectory,” AIAA Paper 2002-4821, Aug. 2002.
<https://arc.aiaa.org/doi/10.2514/6.2002-4821>

- [33] “Juno Mission & Trajectory Design,” Spaceflight 101, retrieved 2 Sept. 2022.
<https://spaceflight101.com/juno/juno-mission-trajectory-design/>
- [34] “Mars Reconnaissance Orbiter: Electrical Power,” NASA Mars, retrieved 22 March 2022.
<https://mars.nasa.gov/mro/mission/spacecraft/parts/electricalpower/>
- [35] Savage, D., O’Donnel, F., and Hardin, M., “2001 Mars Odyssey Arrival Press Kit,” NASA, Pasadena, CA, Oct. 2001.
<https://mars.nasa.gov/odyssey/files/odyssey/odysseyarrival1.pdf>
- [36] Krebs, G. D., “Mars Global Surveyor (MGS),” Gunter's Space Page, retrieved 22 March 2022.
https://space.skyrocket.de/doc_sdat/mars_global_surveyor.htm
- [37] “The 2013 MAVEN Mission to Mars,” Mars.NASA.gov, retrieved 10 April 2022.
<https://mars.nasa.gov/files/resources/MAVENPresentation2013.pdf>
- [38] Brown, D., Agle, D., Martinez, M., and Napier, D., “Juno Launch Press Kit,” NASA, Pasadena, CA, Aug. 2011.
https://www.jpl.nasa.gov/news/press_kits/JunoLaunch.pdf
- [39] Dudzinski, L., “Power and Thermal Systems,” NASA Radioisotope Power Systems, retrieved 22 March 2022.
<https://rps.nasa.gov/power-and-thermal-systems/thermal-systems/general-purpose-heat-source/>
- [40] Dagarin, B. P., Taenaka, R. K., and Stofel, E. J., “Galileo Probe Battery System,” *1996 NASA Aerospace Battery Workshop*, NASA ARC, Huntsville, AL, 1996, pp. 133-144.
<https://ntrs.nasa.gov/api/citations/19970013722/downloads/19970013722.pdf?attachment=true>
- [41] Bennett, G. L., Lombardo, J. J., Hemler, R. J., Silverman, G., Whitmore, C. W., Amos, W. R., Johnson, E. W., Schock, A., Zocher, R. W., Keenan, T. K., Hagan, J. C., and Englehart, R. W., “Mission of Daring: The General-Purpose Heat Source Radioisotope Thermoelectric Generator,” AIAA Paper 2006-4096, June 2006.
<https://nuke.fas.org/space/gphs.pdf>
- [42] Davis, P. W., “Cassini Quick Facts,” Nasa Science: Solar System Exploration, retrieved 22 March 2022.
<https://solarsystem.nasa.gov/missions/cassini/mission/quick-facts/>
- [43] Davis, P. W., “Spacecraft Power for Cassini,” NASA Jet Propulsion Laboratory, retrieved 15 March 2022.
https://solarsystem.nasa.gov/system/downloadable_items/1940_power.pdf
- [44] Dudzinski, L., “New Horizons,” NASA Radioisotope Power Systems, retrieved 10 April 2022.
<https://rps.nasa.gov/missions/7/new-horizons/>

- [45] Bechtel, R., “Multi-Mission Radioisotope Thermoelectric Generator (MMRTG),” U.S. Department of Energy, retrieved 6 Sept. 2022.
https://www.nasa.gov/sites/default/files/files/4_Mars_2020_MMRTG.pdf
- [46] Wertz, J. R., and Larson, W. J., “Spacecraft Design and Sizing: Design Budgets,” *Space Mission Analysis and Design*, 3rd ed., Vol. 1, Springer, New York, 1999, pp. 314-318.
- [47] “Power Special Test Equipment (PSTE),” Ametek Programmable Power, Retrieved 20 Nov. 2021.
<https://www.programmablepower.com/products/engineered-systems/power-special-test-equipment-pste>
- [48] Wertz, J. R., and Larson, W. J., “Space Propulsion Systems,” *Space Mission Analysis and Design*, 3rd ed., Vol. 1, Springer, New York, 1999, pp. 685-718.
- [49] “Mars Reconnaissance Orbiter: Propulsion,” NASA Mars, retrieved 20 April 2022.
<https://mars.nasa.gov/mro/mission/spacecraft/parts/propulsion/>
- [50] “Mars Odyssey: Propulsion,” NASA Mars, retrieved 20 April 2022.
<https://mars.nasa.gov/odyssey/mission/spacecraft/parts/propulsion/>
- [51] “Juno Spacecraft Information,” Spaceflight 101, retrieved 20 April 2022.
<https://spaceflight101.com/juno/spacecraft-information/>
- [52] “Galileo Engineering,” Resa, retrieved 20 April 2022.
<https://web.archive.org/web/20080613233904/http://www.resa.net/nasa/engineer.htm>
- [53] Davis, P. W., “Cassini: Engine,” NASA Science: Solar System Exploration, retrieved 20 April 2022.
<https://solarsystem.nasa.gov/missions/cassini/engine/>
- [54] Hebden, K., “After 37 Years, Voyager 1 Fires Up Dormant Thrusters,” Room: Space Journal of Asgardia, retrieved 6 June 2022.
<https://room.eu.com/news/after-37-years-voyager-1-fires-up-dormant-thrusters>
- [55] “New Horizons Spacecraft Overview,” Spaceflight 101, retrieved 20 April 2022.
<https://spaceflight101.com/newhorizons/spacecraft-overview/>
- [56] St. Pierre, J. A., Francis, K. M., Wynn, J. A., Voth, C. T., “Initial GN&C Performance on the Juno Spacecraft,” *Advances in the Astronautical Sciences*, Vol. 144, 2012.
- [57] Baughman, D., “In-Space Propulsion Data Sheets,” Aerojet Rocketdyne, retrieved 7 June 2022.
https://www.rocket.com/sites/default/files/documents/In-Space%20Data%20Sheets_7.19.21.pdf
- [58] “Propulsion: Monopropellant Thrusters,” MOOG Space and Defense Group, retrieved 7 June 2022.
https://www.moog.com/content/dam/moog/literature/Space_Defense/spaceliterature/propulsion/moog-MonopropellantThrusters-Datasheet.pdf

- [59] Hamilton, J., "Marshall Space Flight Center Test Capabilities," 1 Jan. 2005.
<https://core.ac.uk/download/pdf/10514932.pdf>
- [60] Wertz, J. R., and Larson, W. J., "Spacecraft Subsystems: Thermal," *Space Mission Analysis and Design*, 3rd ed., Vol. 1, Springer, New York, 1999, pp. 428-458.
- [61] Fjeld, P., "Lunar Module Coatings," PFJELD, retrieved 14 Sept. 2018.
<https://www.home.earthlink.net/~pfjeld/lmdata/>
- [62] Ma, S., Jiang, M., Tao, P., Song, C., Wu, J., Wang, J., Deng, T., Shand, W., "Temperature Effect and Thermal Impact In Lithium-Ion Batteries: A Review," *Progress in Natural Science: Materials International*, Vol. 28, No. 6, 2018, pp. 653-666.
[https://www.sciencedirect.com/science/article/pii/S1002007118307536#:~:text=Lithium%2Dion%20batteries%20\(LIBs\),%C2%B0C%20~%2060%20%C2%B0C](https://www.sciencedirect.com/science/article/pii/S1002007118307536#:~:text=Lithium%2Dion%20batteries%20(LIBs),%C2%B0C%20~%2060%20%C2%B0C)
- [63] Hamilton, J., "Marshall Space Flight Center Test Capabilities," 1 Jan. 2005.
<https://core.ac.uk/download/pdf/10514932.pdf>
- [64] Wertz, J. R., and Larson, W. J., "Spacecraft Subsystems: Structures and Mechanisms," *Space Mission Analysis and Design*, 3rd ed., Vol. 1, Springer, New York, 1999, pp. 459-497.
- [65] "MIL-HDBK-5J: Department of Defense Handbook: Metallic Materials and Elements for Aerospace Vehicle Structures," Department of Defense, Arlington County, VA, January 2003.
https://engineering.purdue.edu/AAECourses/aae450/2008/spring/5_struct/MIL-HDBK-5J.pdf
- [66] "Atlas V Launch Services User's Guide," United Launch Alliance, Centennial, CO, March 2010.
https://www.ulalaunch.com/docs/default-source/rockets/atlasvusersguide2010a.pdf?sfvrsn=f84bb59e_2
- [67] "Delta II Payload Planners Guide," United Launch Alliance, Littleton, CO, Dec. 2006.
<https://ula.bsshost.me/docs/default-source/rockets/deltaiipayloadplannersguide2007.pdf>
- [68] Wade, M., "Space Shuttle," Astronautix, retrieved 2 Aug. 2022.
<http://www.astronautix.com/s/spaceshuttle.html>
- [69] Wade, M., "Titan 4," Astronautix, retrieved 2 Aug. 2022.
[http://www.astronautix.com/t/titan4.html#:~:text=Payload%3A%206%2C350%20kg%20\(13%2C990%20lb\)%20to%20a%20GTO](http://www.astronautix.com/t/titan4.html#:~:text=Payload%3A%206%2C350%20kg%20(13%2C990%20lb)%20to%20a%20GTO).
- [70] "AISI Type 304 Stainless Steel," MatWeb, retrieved 17 Aug. 2022.
<https://www.matweb.com/search/datasheet.aspx?matguid=bd20a4281ae3430d97cfbebf6904ec50>
- [71] "NASAFacts: Mars Reconnaissance Orbiter," NASA Jet Propulsion Laboratory, Pasadena, CA, September 2006.
https://www.nasa.gov/pdf/119004main_MRO.pdf
- [72] "Mars Odyssey: Spacecraft," NASA Mars, retrieved 22 July 2022.
<https://mars.nasa.gov/odyssey/mission/spacecraft/>

- [73] Wade, M., “Mars Global Surveyor,” Astronautix, retrieved 22 July 2022.
<http://www.astronautix.com/m/marsglobalsurveyor.html>
- [74] Barnett, A., “Galileo Quick Facts,” Nasa Science: Solar System Exploration, retrieved 22 July 2022.
<https://solarsystem.nasa.gov/missions/galileo/overview/>
- [75] Brown, D., Buckley, M., and Martinez, M., “New Horizons Press Kit,” NASA, Pasadena, CA, February 2007.
http://pluto.jhuapl.edu/News-Center/Resources/Press-Kits/011607_JupiterPressKit.pdf
- [76] “Vibration Testing,” NASA, retrieved 20 Nov. 2021.
https://www.nasa.gov/centers/johnson/pdf/639713main_Vibration_Testing_FTI.pdf
- [77] Hunter, J. M., “Chapter 9: Orbital Perturbations,” *Aerospace Engineering 242: Orbital Mechanics & Mission Design*, 2020, pp. 110-111.
- [78] Hunter, J. M., “Chapter 2: Motion Under a Central Force: The Restricted Two-Body Problem,” *Aerospace Engineering 242: Orbital Mechanics & Mission Design*, 2020, pp. 4-13.
- [79] Wertz, J. R., and Larson, W. J., “Launch Systems,” *Space Mission Analysis and Design*, 3rd ed., Vol. 1, Springer, New York, 1999, pp. 719-744.

APPENDIX A – Calculations for Subsystem Sizing

The excel sheet pages provided in appendix A calculate subsystem sizing for the MMRS. They are adapted from an excel document originally created by David J. Cloud.

A.1 – Communication Downlink Parameters (HGA, X-Band, Mars-Orbiting)

Return to Navigator		Communications System - Downlink											
(All information on this sheet is contained in the block from Cell A1 to Cell Q33)													
Frequency	8.40	8.40	GHz	Data rate	5.280E+05	5.280E+05	bps	Probability of Bit Error	1.00E-05	9.60	DB	Required Eb/No	
Wavelength	3.57E-02	m		Altitude	474560000.000	474560000.000	km	Antenna efficiency	55.0%	70.00	m	Antenna diameter	70.00
Spacecraft Transmitter	27512.20	W		Earth angular radius	0.00	0.00	deg	Antenna efficiency	70.00	70.00	m	Peak antenna gain	73.20
Output power	44.40	dB		Elevation angle	15.00	0.00	deg	Half-power beamwidth	0.14	0.14	deg		
Line loss	-3.00	dB		Nadir angle	0.00	75.00	deg	Pointing error	0.00	-0.17	deg	Antenna pointing loss	
Antenna efficiency	55.0%			Earth central angle	47456477.310	km		Antenna pointing loss	260.00	K		System noise temperature	49.05
Antenna diameter	2.50	m		Propagation path length	0.000	0.000	K	G/T					
Peak antenna gain	44.25	dB		Atmospheric attenuation at zenith	-0.000	0.000	dB	Transmit Antenna Mass		50.3	kg		
Half-power beamwidth	1.00	deg		Rain attenuation	0.000	0.000	dB	Mass					
ERP	85.65	dB		Increase in system noise temp	0.00	0.00	K	Mass & Power Estimates					
Pointing error	0.25	deg		Link Budget				Transmitter mass	357.5	1258894.639	kg		
Antenna pointing loss	-0.75	dB		ERP	85.65	dB		Peak transmitter input power	56701.50	177337.6	W		
Duty cycle (per orbit period)	100.0%			Space loss	-284.40	dB		Average transmitter input power	36701.50	177337.6	W		
				Atmospheric attenuation	-0.53	dB							
				Rain attenuation	0.00	dB							
				G/T	49.05	dB							
				Antenna pointing losses	-0.87	dB							
				Eb/No	20.2	dB							
				C/N0	77.44	dB							
				Implementation loss	-2.00	dB							
				Margin	8.61	dB							

A.4 – Solar Array Sizing (Mars)

Return to Navigator		Power Subsystem - Solar Array Sizing		<i>(All information on this sheet is contained in the block from Cell A1 to Cell I26)</i>		
Required spacecraft power - sunlight	960.1	960.1	W	Total required solar power	1573.5	W
Required spacecraft power - eclipse	960.1	960.1	W	Controlled spacecraft power	1573.5	W
				Converted spacecraft power	1573.5	W
Orbit period	111,000	111.0	min	Ideal solar cell performance	153.0	W/m ²
Maximum eclipse time	21.0	21.0	min	BOL power capability	108.1	W/m ²
Mission duration	17,000	17,000	yrs	EOL power capability	56.4	W/m ²
Solar flux	588.6	588.6	W/m ²	Required solar array area	27.89	m ²
Worst-case Sun incidence angle	23.50	23.50	deg			
Transmission efficiency - sunlight		80.0%				
Transmission efficiency - eclipse		60.0%				
				Solar Array Mass & Power Budgets		
Ideal solar cell efficiency	26.0%	26.0%			Mass	Power
Inherent degradation		77.0%		Solar Arrays	(kg)	(W)
Solar cell degradation per year		3.75%		Deployed	62.9	
Lifetime degradation		52.2%		Cylindrical, body-mounted	197.7	
				Omnidirectional, body-mounted	251.8	
Solar array power density		25.0	W/kg	Power Control Unit	31.5	
Spacecraft dry mass		492.0	kg	Regulator/Converters	39.3	314.7
Percent of spacecraft dry mass for wiring		4.0%		Wiring	19.7	78.7
Percent of spacecraft power for wiring		5.0%				

A.5 – Solar Array Sizing (Jupiter)

Return to Navigator		Power Subsystem - Solar Array Sizing				
<i>(All information on this sheet is contained in the block from Cell A1 to Cell I26)</i>						
Required spacecraft power - sunlight	960.1	960.1	W	Total required solar power	1200.1	W
Required spacecraft power - eclipse	960.1	960.1	W	Controlled spacecraft power	1200.1	W
Orbit period	77040.000	77040.0	min	Converted spacecraft power	1200.1	W
Maximum eclipse time	0.0	0.0	min	Ideal solar cell performance	13.1	W/m ²
Mission duration	17.000	17.000	yrs	BOL power capability	9.3	W/m ²
Solar flux	50.5	50.5	W/m ²	EOL power capability	4.8	W/m ²
Worst-case Sun incidence angle	23.50	23.50	deg	Required solar array area	247.89	m ²
Transmission efficiency - sunlight		80.0%				
Transmission efficiency - eclipse		60.0%				
Ideal solar cell efficiency	26.0%	26.0%		Solar Array Mass & Power Budgets		
Inherent degradation	77.0%	77.0%			Mass	Power
Solar cell degradation per year	3.75%	3.75%		Solar Arrays	(kg)	(W)
Lifetime degradation	52.2%	52.2%		Deployed	48.0	
Solar array power density		25.0	W/kg	Cylindrical, body-mounted	150.8	
Spacecraft dry mass		492.0	kg	Omnidirectional, body-mounted	192.0	
Percent of spacecraft dry mass for wiring		4.0%		Power Control Unit	24.0	240.0
Percent of spacecraft power for wiring		5.0%		Regulator/Converters	30.0	
				Wiring	19.7	60.0

A.6 – Theoretical MMRS Battery Sizing

Return to Navigator		Power Subsystem - Secondary Battery Sizing	
<i>(All information on this sheet is contained in the block from Cell A1 to Cell H15)</i>			
Orbit period	111.0	min	
Maximum eclipse time	21.0	min	
Mission duration	17,000	years	
Required power during eclipse	960.1	W	
Transmission efficiency	90.0%		
Number of charge-discharge cycles	80553		
Depth of discharge	29.9%		
Energy density	50.0	W-hr/Kg	
Bus voltage	28.0	V	
			1247.9
		Battery capacity	W-hr
		Battery capacity	44.6
			A-hr
		Mass of batteries	25.0
			kg

A.7 – Propulsion System Sizing

Return to Navigator		Propulsion System Sizing		<i>(All information on this sheet is contained in the block from Cell A1 to Cell J33)</i>	
Chemical Propulsion System					
Specific impulse	327.0	327.0	sec	Minimum feasible specific impulse	0.4
Spacecraft dry mass (excluding propulsion system)	3625.0	3625.0	kg	Initial stage mass	3634.1
Delta-V requirement	6.8	6.8	m/s	Final stage mass	3626.4
Inert mass fraction		15.0%		Propellant mass	7.7
				Inert mass	1.4
Initial thrust-to-weight ratio		1.50		Thrust	53412.1
				Mass flow rate	16.7
					kg/s
Electric Propulsion System					
Specific impulse	327.0	327.0	sec	Ratio of payload mass to initial mass	
Exhaust velocity		3204.0	m/s	Jet power	
Burn duration			sec	Peak source power	
Burn duration			days	Average source power	
Spacecraft dry mass (excluding propulsion system)		3625.0	kg	Initial stage mass	
Delta-V requirement		6.8	m/s	Final stage mass	
Power system - specific power		50.0	W/kg	Propellant mass	
Power system - specific mass		0.0200	kg/W	Inert mass	
Thrust efficiency		47.5%		Mass flow rate	
Duty cycle (per orbit period)		100.0%		Thrust	
					kg/s
					N

A.8 – Propulsion System Storage & Feed

Return to Navigator		Propulsion System – Storage and Feed				
<i>(All information on this sheet is contained in the block from Cell A1 to Cell H17)</i>						
Thrust	1020.0	1020.0	N	Propellant flow rate	0.32	kg/s
Specific impulse	1123.9	327.0	sec	Fuel flow rate	0.07	kg/s
Propellant mass	1123.9	1123.9	kg	Oxidizer flow rate	0.25	kg/s
Oxidizer to fuel ratio	3.50	3.50		Fuel mass	249.8	kg
Fuel density	875.000	875.000	kg/m ³	Fuel tank volume	0.29	m ³
Oxidizer density	1442.460	1442.460	kg/m ³	Radius of spherical fuel tank	0.413	m
Ullage fraction	3.00%	3.00%		Oxidizer mass	874.1	kg
				Oxidizer tank volume	0.62	m ³
				Radius of spherical oxidizer tank	0.530	m
				Bulk density	1316.36	kg/m ³
				Bulk volume	0.88	m ³

A.9 – Thermal Control System Sizing

Return to Navigator		Thermal Control Subsystem Analysis						
<i>(All information on this sheet is contained in the block from Cell A1 to Cell I29)</i>								
Orbit altitude	370,000	370,000	km	Solar flux			1418.0	W/m ²
Earth angular radius		70.94	deg	Albedo			34.0%	
Albedo reflection factor		0.998		Maximum Earth IR emission			258.0	W/m ²
Available surface area	20,000	20,000	m ²	Minimum Earth IR emission			216.0	W/m ²
Diameter of equivalent sphere		2.52	m	Solar energy absorbed			4254.0	W
Absorptivity of spacecraft surface		60.00%		Albedo energy absorbed			1289.4	W
Emissivity of spacecraft surface		80.00%		Maximum Earth IR energy absorbed			921.9	W
Maximum power dissipation on spacecraft			W	Minimum Earth IR energy absorbed			771.9	W
Minimum power dissipation on spacecraft			W	Maximum equilibrium temperature				deg, C
Upper temperature limit for spacecraft	113.0	113.0	deg, C	Minimum equilibrium temperature				deg, C
Lower temperature limit for spacecraft	-20.0	-20.0	deg, C					
<i>Possible changes to reduce maximum equilibrium temperature to specified upper limit:</i>								
Additional surface area			m ²	New absorptivity of spacecraft surface				
				New emissivity of spacecraft surface				
<i>Heater requirements during eclipse:</i>								
Radiator area to accommodate s/c power dissipation			m ²	Maximum eclipse time			36.2	min
Minimum temperature for given radiator area			deg, C	Duty cycle (per orbit period)			39.4%	
Required heater power (during eclipse)			W	Average heater power				W

A.10 – Thermal Control: Solar Array Analysis

Return to Navigator		Thermal Control – Solar Array Analysis							
<i>(All information on this sheet is contained in the block from Cell A1 to Cell I20)</i>									
Altitude		370.000	km	Solar flux		1418.0	W/m ²		
Earth angular radius		70.94	deg	Worst-case Sun incidence angle		23.50	deg		
Albedo reflection factor		0.998		Albedo		34.0%			
Mission duration	10.000	10.000	yrs	Maximum Earth IR emission		258.0	W/m ²		
				Minimum Earth IR emission		216.0	W/m ²		
Surface area of solar array	20.00	20.00	m ²	Projected surface area		18.34	m ²		
Ideal solar cell efficiency		14.8%							
Inherent degradation		77.0%		Solar energy absorbed		20936.3	W		
Solar cell degradation per year		3.75%		Albedo energy absorbed		4729.7	W		
Lifetime degradation		68.2%		Maximum Earth IR energy absorbed		3381.9	W		
				Minimum Earth IR energy absorbed		2831.3	W		
Absorptivity - top of solar array		80.5%		EOL power output from solar array		2022.4	W		
Absorptivity - bottom of solar array		60.0%		Maximum equilibrium temperature		74.99	deg. C		
Emissivity - top of solar array		82.5%		Minimum equilibrium temperature		-75.02	deg. C		
Emissivity - bottom of solar array		80.0%							

A.11 – Spacecraft Bus: Preliminary Sizing

Return to Navigator		Preliminary Spacecraft Sizing									
(All information on this sheet is contained in the block from Cell A1 to Cell AB27)											
				Mass (kg)	Average Power (W)			Size			
								Minimum	Expected	Maximum	
Payload Mass	130.0	130.0	kg	130.0	1000.0	Spacecraft					
Payload Percentage	27.0%	27.0%	%	263.6	533.9	Volume	8.08	16.16	80.80	m ³	
Margin Percentage (Mass)	25.0%	25.0%	%	29.2	110.4	Body area	3.10	8.61	16.87	m ²	
						Linear dim	1.76	2.93	4.11	m	
Payload Power	1000.0	1000.0	W	101.0	179.7	Moment of inertia	--	2225.14	--	kg-m ²	
Payload Percentage	58.4%	58.4%	%	13.5	31.3						
Margin Percentage (Power)	25.0%	25.0%	%	79.2	0.0						
Orbit Delta V Budget	3190.0	3190.0	m/s	12.4	31.3						
Att Control Percentage	5.0%	5.0%	%	98.4	135.0						
Margin Percentage (Propellant)	25.0%	25.0%	%	12.3	383.5						
Residual Percentage	2.0%	2.0%	%								
Propellant Specific Impulse	327.0	327.0	sec	492.0		Solar array (if deployed)					
						Area	9.35	20.04	28.05	m ²	
						Mass	40.80	76.70	136.06	kg	
						Area offset	3.72	5.98	8.03	m ²	
						Moments of inertia					
						Perpendicular to array face	506.78	2873.62	9158.54	kg-m ²	
						Perpendicular to array axis	580.88	2809.59	8993.46	kg-m ²	
						About array axis	15.89	64.03	160.08	kg-m ²	

A.12 – Structure & Mechanics: Monocoque Structure

Return to Navigator		Structural Analysis: Monocoque Structure										
<i>(All information on this sheet is contained in the block from Cell A1 to Cell O27)</i>												
Cylinder length		2.93	m	Rigidity (Stiffness)								
Cylinder radius		1.32	m	Natural frequency (axial)			27.3	v/s	Set to value			
Spacecraft mass		1615.9	kg	Natural frequency (lateral)			19.5	v/s	Set to value			
Young's modulus		7.100E+10	N/m ²	Axial deflection			0.411	cm				
Material density		2.800E+03	kg/m ³	Lateral deflection			0.504	cm				
Ultimate tensile stress		5.240E+08	N/m ²	Stability								
Yield tensile stress		4.480E+08	N/m ²	Ultimate load			4.172E+05	N				
Factor of safety (ultimate)		1.25		Geometric parameter (phi)			7.352					
Factor of safety (yield)		1.10		Reduction factor (gamma)			0.100					
Axial acceleration load factor	10.0	10.0	g's	Buckling stress			3.066E+05	N/m ²				
Lateral acceleration load factor	5.0	5.0	g's	Critical buckling load			2.440E+02	N			Set to zero	
				Margin of safety			-1.00					
				Applied loads								
Cylinder thickness		9.569E-03	cm	Axial load			1.583E+05	N				
Cross-sectional area		7.961E+00	cm ²	Bending moment			1.161E+05	N-m				
Area moment of inertia		6.979E+04	cm ⁴	Equivalent axial load			3.337E+05	N				
				Ultimate load			4.172E+05	N				
				Yield load			3.671E+05	N				
Skin		6.5	kg	Margin of safety (ultimate)			0.00		Set to zero			
Fasteners & fittings		0.7	kg	Margin of safety (yield)			-0.03		Set to zero			
Total		7.2	kg									

A.13 – Structure & Mechanisms: Semi-Monocoque Structure

Return to Navigator		Structural Analysis: Semi-Monocoque Structure					
<i>(All information on this sheet is contained in the block from Cell A1 to Cell S31)</i>							
Cylinder length	2.93	m		Rigidity (Stiffness)			
Cylinder radius	1.32	m		Natural frequency (axial)		27.3	r/s
Spacecraft mass	1615.9	kg		Natural frequency (lateral)		19.5	r/s
Young's modulus	7.100E+10	N/m ²		Stability			
Poisson's ratio	0.33			Ultimate load		4.172E+05	N
Material density	2.800E+03	kg/m ³		Panel width (b)		2.080	m
Ultimate tensile stress	5.240E+08	N/m ²		Cylinder variable (z)		64460.989	
Yield tensile stress	4.480E+08	N/m ²		Buckling coefficient (k)		18883.7	
Factor of safety (ultimate)	1.25			Buckling stress		6.548E+05	N/m ²
Factor of safety (yield)	1.10			Critical buckling load		5.213E+02	N
				Margin of safety		-1.00	
Axial acceleration load factor	10.0	g's		Applied loads			
Lateral acceleration load factor	5.0	g's		Axial load		1.583E+05	N
				Bending moment		1.161E+05	N-m
				Equivalent axial load		3.337E+05	N
				Ultimate load		4.172E+05	N
Skin thickness	4.784E-03	cm		Yield load		3.671E+05	N
Radius to thickness ratio	27675.4			Margin of safety (ultimate)		0.00	
Cross-sectional area (skin)	3.981E+00	cm ²		Margin of safety (yield)		-0.03	
Area moment of inertia (skin)	3.489E+04	cm ⁴					
				Mass Budget			
Number of stringers	4			Skin		3.3	kg
Cross-sectional area (each stringer)	1.00	cm ²		Stringers		3.3	kg
Area moment of inertia (all stringers)	3.489E+04	cm ⁴		Ring frames & fasteners		1.6	kg
Total cross-sectional area	7.96			Total		8.2	kg

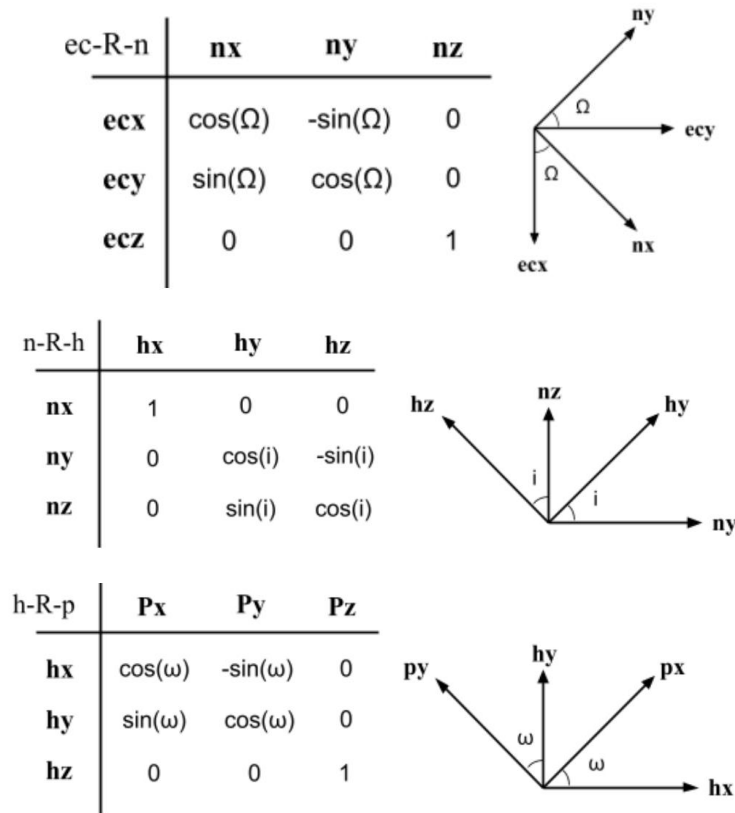
A.14 – Launch Vehicle Information: Atlas V 400

Return to Navigator		Launch Vehicle Information			
<i>(All information on this sheet is contained in the block from Cell A1 to Cell A2125)</i>					
Select Desired Launch Vehicle:		Atlas V 400 [United States]			
Spacecraft loaded mass	1615.9	kg			
Performance					
<i>Mass to orbit</i>					
LEO (typical inclination)	12500.0	kg			
LEO (polar)	10750.0	kg			
GTO	5000.0	kg			
GEO	N/C	kg			
Reliability experience					
<i>Reliability</i>					
Total flights				N/A	
Successes				0	
Partial failures				0	
Total failures				0	
Down time - last failure				N/A	months
Down time - average				N/A	months
Launches since last failure				N/A	months
Available inclinations					
Minimum	28.5	deg			
Maximum	120.0	deg			
Environment					
<i>Injection accuracies</i>					
Apogee location	117.0	km		4.6	m
Perigee location	2.4	km		5.0	m
Inclination	0.20	km		5.3	m
				6.0	g's
				2.0	g's
				15.0	Hz
				8.0	Hz
Flight rate	N/A	per year		83.0	\$M
				Estimated Launch Price	

APPENDIX B – Orbital Mechanics & Mission Design

B.1 – Derivation of Position & Velocity Vectors

Using the reference frame illustrated in figure 7.2, the following rotation tables can be developed. Note that, instead of Earth being the central body, the sun is considered the central body. These tables together show the rotation from the sun-centered (ECI) frame to the perifocal frame in terms of Ω , ω , i , and θ . One rotation is made at a time, with an intermediate frame between rotations. Spacecraft particle Q is then resolved into the sun-centered (ECI) basis vectors.



Ultimately, the rotation of the sun-centered (ECI) frame to the perifocal (P) frame can be represented by matrix multiplication of the above rotation tables as follows.

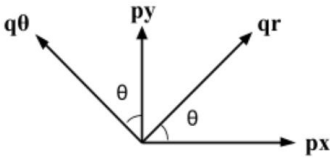
$${}^{EC}R^P = {}^{EC}R^N \times {}^N R^H \times {}^H R^P$$

Performing the multiplication of these three matrices results in the following matrix, which represents the rotation from the ECI frame to the perifocal frame.

$$\begin{vmatrix} \cos(\omega)\cos(\Omega) - \sin(\omega)\sin(\Omega)\cos(i) & -\sin(\omega)\cos(\Omega) - \cos(\omega)\sin(\Omega)\cos(i) & \sin(i)\sin(\Omega) \\ \cos(\omega)\sin(\Omega) + \sin(\omega)\cos(i)\cos(\Omega) & -\sin(\omega)\sin(\Omega) + \cos(\omega)\cos(i)\cos(\Omega) & -\sin(i)\cos(\Omega) \\ \sin(\omega)\sin(i) & \cos(\omega)\sin(i) & \cos(i) \end{vmatrix}$$

To additionally go from the perifocal frame to the Q frame (centered on the spacecraft), the following rotation table can be used.

p-R-q	qr	qθ	qz
Px	cos(θ)	-sin(θ)	0
Py	sin(θ)	cos(θ)	0
Pz	0	0	1



B.2 – Code: Position & Velocity Vectors from Keplerian Elements (Mars About Sun)

The following code was developed in MATLAB that converts between the input of the six Keplerian elements and outputs the associated initial position and velocity vector of Mars about the sun.

```

%% Position Vectors (MARS about sun)
clear all
close all
clc
% Sun
G = 6.67e-20;
M = 1.989e30;
GM = G*M; % kg^2/sec^2

ra = 249.261e6; % Mars furthest approach (km)
rp = 206.650e6; % Mars closest approach (km)

% Keplerian Elements (Note: Can use GMAT to calculate some keplerian based on ra
and rp inputs)
e = (ra-rp)/(ra+rp); % Eccentricity (ellipse)
theta = 0; % True Anomaly (rad) (θ at periapsis)
i = 1.85061; % Inclination of orbit plane (deg)
cap_omega = 49.57854; % Right Ascension of the Ascending Node (deg)
low_omega = 336.04084; % Argument of Periapsis (deg)

a = 0.5*(rp+ra) % Semi-Major Axis length (km) (Keplerian Element)
h = sqrt(GM*a)*sqrt(1-e^2) % Specific Angular Aomentum (km/sec)

% a) -- Position in P frame-- (THETA IN DEG)

```

```

r_vector = ((h^2)/GM)/(1+e*cosd(theta));
pos_Px = r_vector*(cosd(theta));
pos_Py = r_vector*(sind(theta));
r_in_p = [pos_Px pos_Py]

% b) -- Position in ECI frame-- (omegas, i in deg)
pos_ECx = pos_Px*(cosd(low_omega)*cosd(cap_omega) -
sind(low_omega)*sind(cap_omega)*cosd(i))...
+ pos_Py*(-sind(low_omega)*cosd(cap_omega) -
cosd(low_omega)*sind(cap_omega)*cosd(i));
pos_ECy = pos_Px*(cosd(low_omega)*sind(cap_omega) +
sind(low_omega)*cosd(i)*cosd(cap_omega))...
+ pos_Py*(-sind(low_omega)*sind(cap_omega) +
cosd(low_omega)*cos(i)*cos(cap_omega));
pos_ECz = pos_Px*(sind(low_omega)*sind(i))...
+ pos_Py*(cosd(low_omega)*sind(i));
r_in_ECI = [pos_ECx pos_ECy pos_ECz]

% c) -- Velocity in P frame-- (omegas, i in deg)
vel_Px = (GM/h)*(-sind(theta)); %(THETA IN DEG)
vel_Py = (GM/h)*(e+cosd(theta)); %(THETA IN DEG)
v_in_P = [vel_Px vel_Py]

% d) -- Velocity in ECI frame-- (omegas, i in deg)
vel_ECx = vel_Px*(cosd(low_omega)*cosd(cap_omega) -
sind(low_omega)*sind(cap_omega)*cosd(i))...
+ vel_Py*(-sind(low_omega)*cosd(cap_omega) -
cosd(low_omega)*sind(cap_omega)*cosd(i));
vel_ECy = vel_Px*(cosd(low_omega)*sind(cap_omega) +
sind(low_omega)*cosd(i)*cosd(cap_omega))...
+ vel_Py*(-sind(low_omega)*sind(cap_omega) +
cosd(low_omega)*cosd(i)*cosd(cap_omega));
vel_ECz = vel_Px*(sind(low_omega)*sind(i))...
+ vel_Py*(cosd(low_omega)*sind(i));
v_in_ECI = [vel_ECx vel_ECy vel_ECz]

```

B.3 – Code: Position & Velocity Vectors from Keplerian Elements (Earth About Sun)

The following code was developed in MATLAB that converts between the input of the six Keplerian elements and outputs the associated initial position and velocity vector of Earth about the sun.

```

%% Position Vectors (Earth about sun)
clear all
close all
clc
% Sun
G = 6.67e-20;
M = 1.989e30;
GM = G*M; % kg^2/sec^2

```

```

% Keplerian Elements    (Note: Can use GMAT to calculate some keplerian based on ra
and rp inputs)
ra = 152.1e6;          % Earth furthest approach (km)
rp = 147.095e6;       % Earth closest approach (km)

e = (ra-rp)/(ra+rp);  % Eccentricity (ellipse)
theta = 0;            % True Anomaly (rad) (0 at periapsis)
i = 0.00005 ;        % Inclination of orbit plane (deg)
cap_omega = -11.26064; % Right Ascension of the Ascending Node (deg)
low_omega = 102.94719; % Argument of Periapsis (deg)

a = 0.5*(rp+ra)          % Semi-Major Axis length (km) (Keplerian Element)
h = sqrt(GM*a)*sqrt(1-e^2) % Specific Angular Aomentum (km/sec)

% a) -- Position in P frame-- (THETA IN DEG)
r_vector = ((h^2)/GM)/(1+e*cosd(theta));
pos_Px = r_vector*(cosd(theta));
pos_Py = r_vector*(sind(theta));
r_in_p = [pos_Px pos_Py]

% b) -- Position in ECI frame-- (omegas, i in deg)
pos_ECx = pos_Px*(cosd(low_omega)*cosd(cap_omega) -
sind(low_omega)*sind(cap_omega)*cosd(i))...
+ pos_Py*(-sind(low_omega)*cosd(cap_omega) -
cosd(low_omega)*sind(cap_omega)*cosd(i));
pos_ECy = pos_Px*(cosd(low_omega)*sind(cap_omega) +
sind(low_omega)*cosd(i)*cosd(cap_omega))...
+ pos_Py*(-sind(low_omega)*sind(cap_omega) +
cosd(low_omega)*cos(i)*cosd(cap_omega));
pos_ECz = pos_Px*(sind(low_omega)*sind(i))...
+ pos_Py*(cosd(low_omega)*sind(i));
r_in_ECI = [pos_ECx pos_ECy pos_ECz]

% c) -- Velocity in P frame-- (omegas, i in deg)
vel_Px = (GM/h)*(-sind(theta)); % (THETA IN DEG)
vel_Py = (GM/h)*(e+cosd(theta)); % (THETA IN DEG)
v_in_P = [vel_Px vel_Py]

% d) -- Velocity in ECI frame-- (omegas, i in deg)
vel_ECx = vel_Px*(cosd(low_omega)*cosd(cap_omega) -
sind(low_omega)*sind(cap_omega)*cosd(i))...
+ vel_Py*(-sind(low_omega)*cosd(cap_omega) -
cosd(low_omega)*sind(cap_omega)*cosd(i));
vel_ECy = vel_Px*(cosd(low_omega)*sind(cap_omega) +
sind(low_omega)*cosd(i)*cosd(cap_omega))...
+ vel_Py*(-sind(low_omega)*sind(cap_omega) +
cosd(low_omega)*cosd(i)*cosd(cap_omega));
vel_ECz = vel_Px*(sind(low_omega)*sind(i))...
+ vel_Py*(cosd(low_omega)*sind(i));
v_in_ECI = [vel_ECx vel_ECy vel_ECz]

```

B.4 – Code: Position & Velocity Vectors from Keplerian Elements (Transfer About Sun)

The following code was developed in MATLAB that converts between the input of the six Keplerian elements and outputs the associated initial position and velocity vector of spacecraft Q in an elliptical transfer orbit from Earth to Mars about the sun.

```
%% Position Vectors (Transfer Orbit - Earth/Mars)
clear all
close all
clc
% Sun
G = 6.67e-20;
M = 1.989e30;
GM = G*M;    % kg^2/sec^2

ra = 249.261e6;    % Furthest approach (Mars) (km)
rp = 147.095e6;    % Closest approach (Earth) (km)

% Keplerian Elements    (Note: Can use GMAT to calculate some keplerian based on ra
and rp inputs)
e = (ra-rp)/(ra+rp);    % Eccentricity (ellipse)
theta = 0;              % True Anomaly (rad) (0 at periapsis)
i = 0.00005;           % Inclination of orbit plane (deg)
cap_omega = -11.26064; % Right Ascension of the Ascending Node (deg)
low_omega = 102.94719; % Argument of Periapsis (deg)

a = 0.5*(rp+ra)          % Semi-Major Axis length (km) (Keplerian Element)
h = sqrt(GM*a)*sqrt(1-e^2) % Specific Angular Aomentum (km/sec)

% a) -- Position in P frame--    (THETA IN DEG)
r_vector = ((h^2)/GM)/(1+e*cosd(theta));
pos_Px = r_vector*cosd(theta);
pos_Py = r_vector*sind(theta);
r_in_p = [pos_Px pos_Py]

% b) -- Position in ECI frame--    (omegas, i in deg)
pos_ECx = pos_Px*(cosd(low_omega)*cosd(cap_omega) -
sind(low_omega)*sind(cap_omega)*cosd(i))...
+ pos_Py*(-sind(low_omega)*cosd(cap_omega) -
cosd(low_omega)*sind(cap_omega)*cosd(i));
pos_ECy = pos_Px*(cosd(low_omega)*sind(cap_omega) +
sind(low_omega)*cosd(i)*cosd(cap_omega))...
+ pos_Py*(-sind(low_omega)*sind(cap_omega) +
cosd(low_omega)*cos(i)*cos(cap_omega));
pos_ECz = pos_Px*(sind(low_omega)*sind(i))...
+ pos_Py*(cosd(low_omega)*sind(i));
r_in_ECI = [pos_ECx pos_ECy pos_ECz]

% c) -- Velocity in P frame--    (omegas, i in deg)
vel_Px = (GM/h)*(-sind(theta));    %(THETA IN DEG)
vel_Py = (GM/h)*(e+cosd(theta));    %(THETA IN DEG)
```

```

v_in_P = [vel_Px vel_Py]

% d) -- Velocity in ECI frame-- (omegas, i in deg)
vel_ECx = vel_Px*(cosd(low_omega)*cosd(cap_omega) -
sind(low_omega)*sind(cap_omega)*cosd(i))...
    + vel_Py*(-sind(low_omega)*cosd(cap_omega) -
cosd(low_omega)*sind(cap_omega)*cosd(i));
vel_ECy = vel_Px*(cosd(low_omega)*sind(cap_omega) +
sind(low_omega)*cosd(i)*cosd(cap_omega))...
    + vel_Py*(-sind(low_omega)*sind(cap_omega) +
cosd(low_omega)*cosd(i)*cosd(cap_omega));
vel_ECz = vel_Px*(sind(low_omega)*sind(i))...
    + vel_Py*(cosd(low_omega)*sind(i));
v_in_ECI = [vel_ECx vel_ECy vel_ECz]

```

B.5 – Code: Hohmann Transfer Wait Time

The following code was developed in MATLAB that calculates the wait time before the Hohmann transfer can be initiated such that the spacecraft Q will intercept Mars at the same location at the same time.

```

%% (Hohmann wait time) (Leverage 7.10.11)
clear all
close all
clc

% Constants
G = 6.67e-20;
Msun = 1.989e30;      % Mass sun (kg)
GMsun = G*Msun;

r1 = 147.095e6;      % INT Orbit radius (km) (Perigee)
r2 = 249.261e6;      % TGT Orbit (Apogee)
a = 0.5*(r1+r2);

theta1 = 180;      % True Anomaly (deg) - KEEP AT 180
theta2 = 270;      % True Anomaly (deg) - VARIABLE

% Target (Mars)
tau_tgt = 2*pi*sqrt((r2^3)/(GMsun));      % Period TGT orbit (sec)
omega_tgt = (2*pi/tau_tgt)*3600;      % Angular velocity TGT orbit (rad/HR)

% Interceptor (Earth)
tau_int = 2*pi*sqrt((r1^3)/(GMsun));      % Period INT orbit (sec)
omega_int = (2*pi/tau_int)*3600;      % Angular velocity INT orbit (rad/HR)

% Transfer (Ellipse ffrom Earth to Mars)
tau_tr = 2*pi*sqrt((a^3)/(GMsun))*(1/3600)*0.5      % Period of transfer orbit (1/2
ellipse) (hr)
% Angle through which TGT moves during course of maneuver
angle = tau_tr*omega_tgt*57.2958      % (1 rad = 57.2958 deg)

```

```

% --Wait time (theta1 = 180)--
wait = ((theta1-(theta1-angle))/(omega_int-omega_tgt))*(1/60)*(1/24) % (days)

% Angle each craft travels during wait time
int_travel_angle = omega_int*wait*57.2958 % (deg)
tgt_travel_angle = omega_tgt*wait*57.2958 % (deg)

%--Wait time (theta2 = variable)--
wait2 = ((theta2-(theta1-angle))/(omega_int-omega_tgt))*(1/60)*(1/24); % (days)

if wait2 < 0
    wait2 = ((theta2-(theta1-angle)+360)/(omega_int-omega_tgt))*(1/60)*(1/24);
else
    wait2 = wait2
end

% Angle each craft travels during wait time
int_travel_angle2 = omega_int*wait2*57.2958*(24); % (deg) *24 FACTOR
tgt_travel_angle2 = omega_tgt*wait2*57.2958*(24); % (deg) *24 FACTOR

```

B.6 – Code: Hohmann Transfer Delta-V

The following code was developed in MATLAB that calculates the delta-v required for spacecraft Q to make a Hohmann transfer from Earth to Mars.

```

%% (Hohmann delta v) (Leverage DP 4/18)
clear all
close all
clc

% Constants
G = 6.67e-20;
%Mearth = 5.972e24; % Mass Earth (kg) Planet 1
%Mmars = 6.4169e23; % Mass Mars (kg) Planet 2
Msun = 1.989e30; % Mass sun (kg)

rearth = 6378; % Radius Earth (km) Planet 1
%rmars = 3389; % Radius Mars (km) Planet 2
%rsun = 695800; % Radius Sun (km)

r1 = 147.095e6; % Distance Earth to sun (km) (perigee)
r2 = 249.261e6; % Distance Mars to sun (km) (Apogee)

%-First delva v-
r_circ_1 = r1; % Earth orbit radius (Altitude = 0)
V_circ_1 = sqrt((G*Msun)/r_circ_1)

r_p2 = r_circ_1;
r_a2 = r2; % Mars orbit radius (Altitude = 0)
a2 = 0.5*(r_p2+r_a2);
V_p2 = sqrt(G*Msun)*sqrt((2/r_p2)-(1/a2));

```



```

delta_v1 = V_p2-V_circ_1

%-Second delva v-
r_circ_2 = r2;    % Mars orbit radius (Altitude = 0)
V_circ_2 = sqrt((G*Msun)/r_circ_2)

r_a2 = r2;    % Mars orbit radius (Altitude = 0)
V_a2 = sqrt(G*Msun)*sqrt((2/r_a2)-(1/a2));

delta_v2 = V_circ_2-V_a2

%-Total delta v-
delta_v = delta_v1 + delta_v2

% ---Time for orbit transfer---
tau_sec = 2*pi*sqrt((a2^3)/(G*Msun))*0.5    % Total transfer time (sec)
tau_days = 2*pi*sqrt((a2^3)/(G*Msun))*0.5*(1/60)*(1/60)*(1/24)    % Total transfer
time (days)

```

B.7 – Code: Keplerian Elements from Position & Velocity Vectors

The following code was developed in MATLAB that calculates the six Keplerian elements required to define an orbit from inputs of the initial position and velocity vector of the orbit. Orbit period is also calculated.

```

% Find Keplerian elements from r and v (+ resolution of quadrant ambiguity)
% (Like Problem 5.9.4/5.9.5)
clear all
close all
clc

%---Givens---
GM = 398332;    % kg^2/sec^2

% Position Vector
pos_ECx = -6859.3;
pos_ECy = 3212.4;
pos_ECz = -994.8;
r_in_ECI = [pos_ECx pos_ECy pos_ECz]

% Velocity Vector
vel_ECx = -1.7998;
vel_ECy = -7.1040;
vel_ECz = -1.2961;
v_in_ECI = [vel_ECx vel_ECy vel_ECz]

%---Keplerian Elements----
% a) Specific angular momentum, h
r_vector = [pos_ECx pos_ECy pos_ECz];
v_vector = [vel_ECx vel_ECy vel_ECz];
h_vector = cross(r_vector,v_vector)    % Cross product of r x v    (h vector = r x
v)

```

```

h = sqrt(dot(h_vector,h_vector))      % Dot product of h dot h      (h = sqrt(h dot
h))

% b) Eccentricity, e
v_cross_h = cross(v_vector,h_vector);
r = sqrt(dot(r_vector,r_vector));
e_vector = (v_cross_h/GM) - (r_vector/r)
e = sqrt(dot(e_vector,e_vector))

% c) Inclination angle, i (deg)
ECz = [0 0 1];
i = acosd(dot(ECz,h_vector)/h)
%i = acosd(dot(1,54577.1)/h) %i = acosd(dot(ECz,ECz component of h)/h)

% d) True anomaly, theta (deg)
theta = acosd((dot(r_vector,e_vector))/(r*e));

% Quadrant Ambiguity Test
if dot(r_vector,v_vector) < 0
    theta = 360 - theta
else
    theta = theta
end

% e) Right ascension of the ascending node, cap_omega (deg)
ECz = [0 0 1];
ECy = [0 1 0];
ECx = [1 0 0];
n_vector = cross(ECz,h_vector)
n = sqrt(dot(n_vector,n_vector));
cap_omega = acosd(dot(ECx,n_vector)/n);

% Quadrant Ambiguity Test
if dot(n_vector,ECy) < 0
    cap_omega = 360 - cap_omega
else
    cap_omega = cap_omega
end

% f) Argument of perigee, low_omega (deg)
low_omega = acosd(dot(e_vector,n_vector)/(e*n));

% Quadrant Ambiguity Test
if dot(e_vector,ECz) < 0
    low_omega = 360 - low_omega
else
    low_omega = low_omega
end

% g) Semi-major axis length, a (m)
a = ((h^2)/GM)*(1/(1-e^2))

% Orbital period
T = 2*pi*sqrt(a^3/GM)    % Orbial period

```

B.8 – Code: Animation of Earth, Mars, & Hohmann Orbits

The following code was developed in MATLAB. This code leverages the code provided in appendices B.2 to B.7. The position and velocity vectors calculated using those codes are used as inputs. The results are then plotted and animated in 3D. This code was developed in collaboration with Jordan Pollard, and is included with expressed permission.

```
% Jordan Pollard & Tyler Saunders
clear all;
close all;
clc;
%-----
% constants
hours=5800;
G=6.6742e-20; % gravatational values
M_Sun=1.989e30; % mass of Sun
% R_Sun=695800; % radius of Sun in Km
% R_Earth=6378; % radius of earth in Km
% R_Mars=3397; % radius of mars in Km
R_Sun=7958000; % radius of Sun in Km (not to scale)
R_Earth=5378000; % radius of earth in Km (not to scale)
R_Mars=4397000; % radius of mars in Km (not to scale)
r0E= [-0.0433e8 1.4703e8 0.0000];
v0E=[-30.2688 -0.8912 0.0000];
r0M= [1.8630e8 0.8938e8 -0.0271e8];
v0M=[-11.4466 23.8820 0.7819];
r0T=[-0.0433e8 1.4703e8 0.0000]; % intial position in km Earth orbit
% r0T=[149967000 -293159 0]; % intial position in km Earth orbit
v0T=[-33.6661 -0.9913 0.0000]; % initial Velocity in km/s Earth orbit
r03=[-1.1334e8 2.3919e8 0]; % intial position in km Mars Orbit
v03=[-23.6322 -9.6601 0]; % initial Velocity in km/s Mars Orbit
%Hyperbolic Trajectory:

t0=0; % intial time
tf=95000000; % intial time transfer
t0M=0; % intial time
tfM=98400000;
t0T=0; % intial time
tfT=20000000;
t03=20000000; % intial time transfer
tf3=300002800; % time of flight/final time transfer
theta=0:0.01:2*pi;
y0=[r0E v0E]';
y0M=[r0M v0M]';
y0T=[r0T v0T]';
y03=[r03 v03]';
%-----
% ODE45 construction
options = odeset('RelTol',1e-10,'AbsTol',1e-10);
[tE,fE]=ode45(@ratesSun,[t0 tf],y0,options);
[tM,fM]=ode45(@MarsorbitSun,[t0M tfM],y0M,options);
[tT,fT]=ode45(@EarthMarsTransfer,[t0T tfT],y0T,options);
% [t3,f3]=ode45(@rates2,[t03 tf3],y03,options);
```

```

%-----
%Plot of 3D Orbit
xout=fE(:,1);
yout=fE(:,2);
zout=fE(:,3);
xoutM=fM(:,1);
youtM=fM(:,2);
zoutM=fM(:,3);
xoutT=fT(:,1);
youtT=fT(:,2);
zoutT=fT(:,3);
[XM,YM,ZM] = sphere;
XM=XM*R_Mars;
YM=YM*R_Mars;
ZM=ZM*R_Mars;
[XE,YE,ZE] = sphere;
XE=XE*R_Earth;
YE=YE*R_Earth;
ZE=ZE*R_Earth;
[X,Y,Z] = sphere;
X=X*R_Sun;
Y=Y*R_Sun;
Z=Z*R_Sun;
fig=figure();
set(fig,'color','white')
plot3(xout, yout, zout,'b-',xoutM, youtM, zoutM,'r-',xoutT, youtT, zoutT,'g-',
'linewidth',4)
% plot3(xoutM, youtM, zoutM,'r-','linewidth',4)
% plot3(xoutT, youtT, zoutT,'g-','linewidth',4)
grid on
hold on
axis equal
surf(X,Y,Z,'FaceColor','y','FaceAlpha',.5)
surf(XM-64963100,YM-231581000,ZM-3253790,'FaceColor','r','FaceAlpha',.5)
surf(XE+1842520,YE+147084000,ZE,'FaceColor','b','FaceAlpha',.5)
title('Mission Profile: Sun Center Transfer');
xlabel('x km');
ylabel('y km');
zlabel('z km');
legend('Earth Orbit','Mars Orbit','Transfer Orbit');
%-----
%Animation
figure;
hold all;
[Sun_x,Sun_y,Sun_z] = sphere;
surf(Sun_x*R_Sun,Sun_y*R_Sun,Sun_z*R_Sun,'FaceColor','y','FaceAlpha',.5);
myLines(1) = plot3(NaN, NaN, NaN,'LineWidth',1);
myLines(2) = plot3(NaN, NaN, NaN, '-b','LineWidth',1);
myLines(3) = plot3(NaN, NaN, NaN,'LineWidth',1);
myLines(4) = plot3(NaN, NaN, NaN, '-r','LineWidth',1);
myLines(5) = plot3(NaN, NaN, NaN,'LineWidth',1);
myLines(6) = plot3(NaN, NaN, NaN, '-g','LineWidth',1);
n_time_faster = 1500;
time_pause = 30/n_time_faster;
np = 10;

```

```

title('Mission Profile: Sun Center Transfer');
xlabel('x km');
ylabel('y km');
zlabel('z km');
grid on;
axis equal;
view(45, 10);
rotate3d on;
tam=length(tE);
tamM = length(fM);

% Earth orbit animaition
for k = 1:np:tam
    pause(time_pause);
    set(myLines(1), 'XData', fE(1:k-1,1), 'YData', fE(1:k-1,2), 'ZData', fE(1:k-
1,3));
    set(myLines(2), 'Marker','o','color','b','XData', fE(k,1), 'YData', fE(k,2),
'ZData', fE(k,3));
    drawnow;
end
% Mars orbit animation
for kM = 1:np:tamM
    pause(time_pause);
    set(myLines(3), 'XData', fM(1:kM,1), 'YData', fM(1:kM,2), 'ZData', fM(1:kM,3));
    set(myLines(4), 'Marker','o','color','r','XData', fM(kM,1), 'YData', fM(kM,2),
'ZData', fM(kM,3));
    drawnow;
end
myLines(1) = plot3(NaN, NaN, NaN,'LineWidth',1);
tamT = length(fT);
% Perform the plotting for transfer
for kT = 1:np:tamT
    pause(time_pause);
    set(myLines(5), 'XData', fT(1:kT,1), 'YData', fT(1:kT,2), 'ZData', fT(1:kT,3));
    set(myLines(6), 'Marker','^','color','g','XData', fT(kT,1), 'YData', fT(kT,2),
'ZData', fT(kT,3));
    drawnow;
end
% myLines(5) = plot3(NaN, NaN, NaN,'LineWidth',1);
% myLines(6) = plot3(NaN, NaN, NaN, '-b','LineWidth',1);
% tam3 = length(f3);
%% Perform the plotting for transfer
% for k3 = 1:np:tam3
%     pause(time_pause);
%     set(myLines(5), 'XData', f3(1:k3,1)-64963100, 'YData', f3(1:k3,2)-231581000,
'ZData', f3(1:k3,3)-3253790);
%     set(myLines(6), 'Marker','o','XData', f3(k3,1)-64963100, 'YData', f3(k3,2)-
231581000, 'ZData', f3(k3,3)-3253790);
%     drawnow;
% end
%-----
% state space function construction
function dydt = ratesSun(tE,fE)
G=6.6742e-20;           % gravatational values
M_Sun=1.989e30;       % mass of Earth

```

```

mu=G*(M_Sun);
x=fE(1);
y=fE(2);
z=fE(3);
vx=fE(4);
vy=fE(5);
vz=fE(6);
r=norm([x y z]);
ax=-mu*x/r^3;
ay=-mu*y/r^3;
az=-mu*z/r^3;
dydt=[vx vy vz ax ay az ]';
end

```

```

function dfdt = EarthMarsTransfer(tT,fT)
G=6.6742e-20; % gravatiational values
T_Sun=1.989e30; % Tass of The Sun
mu=G*(T_Sun);
xT=fT(1);
yT=fT(2);
zT=fT(3);
vxT=fT(4);
vyT=fT(5);
vzT=fT(6);
rT=sqrt(xT^2+yT^2+zT^2);
axT=-mu*xT/rT^3;
ayT=-mu*yT/rT^3;
azT=-mu*zT/rT^3;
dfdt=[vxT vyT vzT axT ayT azT ]';
end

```

```

function dfdt = MarsorbitSun(tM,fM)
G=6.6742e-20; % gravatiational values
M_Sun=1.989e30; % mass of The Sun
mu=G*(M_Sun);
xM=fM(1);
yM=fM(2);
zM=fM(3);
vxM=fM(4);
vyM=fM(5);
vzM=fM(6);
rM=sqrt(xM^2+yM^2+zM^2);
axM=-mu*xM/rM^3;
ayM=-mu*yM/rM^3;
azM=-mu*zM/rM^3;
dfdt=[vxM vyM vzM axM ayM azM ]';
end

```

```

function dfdt = orbitchange(t2,f2)
G=6.6742e-20; % gravatiational values
M_Earth=5.974e24; % mass of Earth
mu=G*(M_Earth);

```

```

% G=6.6742e-20;           % gravatiational values
% M_Mars=0.64169e24;     % mass of mars
% mu=G*(M_Mars);
x2=f2(1);
y2=f2(2);
z2=f2(3);
vx2=f2(4);
vy2=f2(5);
vz2=f2(6);
r2=sqrt(x2^2+y2^2+z2^2);
ax2=-mu*x2/r2^3;
ay2=-mu*y2/r2^3;
az2=-mu*z2/r2^3;
dfdt=[vx2 vy2 vz2 ax2 ay2 az2 ]';
end

```

```

function dfdt = rates2(t3,f3)
G=6.6742e-20;           % gravatiational values
% M_Earth=5.974e24;     % mass of Earth
% mu=G*(M_Earth);
M_Mars=0.64169e24;     % mass of mars
mu=G*(M_Mars);
x3=f3(1);
y3=f3(2);
z3=f3(3);
vx3=f3(4);
vy3=f3(5);
vz3=f3(6);
r3=sqrt(x3^2+y3^2+z3^2);
ax3=-mu*x3/r3^3;
ay3=-mu*y3/r3^3;
az3=-mu*z3/r3^3;
dfdt=[vx3 vy3 vz3 ax3 ay3 az3 ]';
end

```

APPENDIX C – Risk Assessment

C.1 – Rubrics for Ascertaining Risk Level

The rubrics below are used to gauge risk. The values 1 through 5 denote the likelihood of the risk factor occurring. The letters A through E denote the consequence if the risk factor were to occur. The color codes (red, yellow, or green), denote the impact the risk factor would have on the system. Risks are first identified by number and letter. The color of the corresponding square then denotes whether the risk is acceptable, moderate, or unacceptable.

5					
4					
3					
2					
1					
	A	B	C	D	E

Level	Likelihood
5	Near Certainty
4	Highly Likely
3	Likely
2	Low Likelihood
1	Not Likely

	Unacceptable
	Moderate
	Acceptable

Level	Consequence
E	Catastrophic
D	Major
C	Moderate
B	Minor
A	Insignificant